Quantifying Emissions of Greenhouse Gases from South Asia Through a Targeted Measurement Campaign

by

Anita Lakshmi Ganesan

B.S., Cornell University (2005)

Submitted to the Department of Earth, Atmospheric and Planetary Sciences
in partial fulfillment of the requirements for the degree of

Doctor of Philosophy in Climate Physics and Chemistry

at the

MASSACHUSETTS INSTITUTE OF TECHNOLOGY

June 2013

Author .....
Department of Earth, Atmospheric and Planetary Sciences
March 29, 2013

Certified by .....
Ronald G. Prinn
TEPCO Professor of Atmospheric Science
Thesis Supervisor

Accepted by .....
Robert van der Hilst
Schlumberger Professor of Earth and Planetary Sciences
Head, Department of Earth, Atmospheric and Planetary Sciences

Quantifying Emissions of Greenhouse Gases from South Asia Through a Targeted Measurement Campaign

by

Anita Lakshmi Ganesan

Submitted to the Department of Earth, Atmospheric and Planetary Sciences
on March 29, 2013, in partial fulfillment of the
requirements for the degree of
Doctor of Philosophy in Climate Physics and Chemistry

Abstract

Methane (CH_4), nitrous oxide (N_2O) and sulfur hexafluoride (SF_6) are powerful greenhouse gases with global budgets that are well-known but regional distributions that are not adequately constrained for the purposes of mitigation and policy initiatives. Quantifying emissions using inverse approaches at the national scale requires measurements that specifically target the region of interest. Primarily due to the lack of atmospheric measurements from the region, emissions estimates of these greenhouse gases from India have largely been missing.

New *in situ* measurements of atmospheric mole fractions from a Himalayan station in Darjeeling, India (27.03°N, 88.26°E, 2200 meters above sea level) have been collected from December 2011 for CH_4 and March 2012 for N_2O and SF_6 to February 2013 using high-precision instrumentation that is linked to the Advanced Global Atmospheric Gases Experiment (AGAGE). These measurements comprise the first high-frequency dataset of these gases collected in India and are used for measurement-based assessment of emissions. Several features are identified. In SF_6, the signal associated with Northern Hemispheric background is typically present. CH_4 and N_2O mole fractions are almost always enhanced over the background, suggesting strong regional sources. Additionally, a diurnal signal resulting from thermally driven winds is seasonally present.

A particle dispersion model is used to track 'air histories' of measurements, quantifying the sensitivity of concentrations at Darjeeling to surface emissions. The effect of topography on the derived air histories is investigated to test the robustness of the model in simulating transport in this complex environment. The newly acquired data set is used to investigate the ability of the model to reproduce signals that stem from the mesoscale diurnal winds. The sensitivities of meteorological resolution and particle release height are investigated to better quantify some of the uncertainties associated with this chemical transport model.

A Quasi-Newton inverse method is used to estimate emissions at monthly resolution. CH_4, N_2O and SF_6 emissions from India are found to be $44.3^{54.2}_{38.5}$ Tg yr^{-1}, 825^{1045}_{707} GgN yr^{-1} and 221^{241}_{205} kton yr^{-1}, respectively. Significant uncertainty reduc-

tion is seen on emissions from India during the summer when the monsoon results in high sensitivity over the subcontinent.

Thesis Supervisor: Ronald G. Prinn
Title: TEPCO Professor of Atmospheric Science

Acknowledgments

There are many people who have supported this work and have each contributed in their own way to the success of the project. First, is my thesis advisor, Ron Prinn, who has provided me with many opportunities throughout my graduate career and also the guidance to achieve everything that has been accomplished. I would also like to thank my thesis committee - Shuhei Ono for the ongoing discussions about my work in India, Simon O'Doherty and Alistair Manning, who on numerous occasions have helped advise this project and who have also made the UK feel like a second home.

This project could not have happened without my collaborators from the Bose Institute. First and foremost is Dr. Abhijit Chatterjee, who has really seen this project through to the end. His interest in the goals of this research and his management of all of the details required to operate a remote instrument has contributed to the success of the measurement campaign. I have a special appreciation for the work done by Mrs. Yashodhara Yadav, my technician in Darjeeling who has been operating and maintaining the instrument while I have been away. She is the most dedicated person that I could have ever imagined to have working on my instrument and has dealt with all of the problems that arise at remote field sites. She has worked day and night to ensure the smooth running of the instrument and I very much appreciate her hard work. I also acknowledge Dr. Sanjay Ghosh, Mr. D.K. Roy and Prof. Sibaji Raha who have also gone out of their way to help with the complicated logistics of this project.

I have a special thanks to the Weiss Lab at the Scripps Institution of Oceanography - Chris Harth, Peter Salameh, Jens Muhle, Steph Mumma, Adam Cox, Tim Arnold and Ray Weiss. This project would not have been the same without their continual support. I cannot thank them enough for their dedication to my work, for calibrating standards and for hosting me in their lab for six months. Many other colleagues in AGAGE and NOAA have also provided me with advice throughout the past few years and I thank them for their guidance.

The support at MIT has been incredible. My fellow atmospheric chemists, Diane Ivy and Laura Meredith have each contributed in so many ways. My work has benefited strongly from their support but I have benefited personally from their friendship. Malte Jansen, Dan Chavas, Roberta Sciascia, Mike Byrne, Marty Singh, Cim Wortham, Andrew Barton, Fanny Monteiro and many others have been great friends that have made the past six years very enjoyable. My fellow 'Prinn group' members have been tremendously supportive. A special thanks to Bhaskar Gunturu and Arnico Panday for advice when I was still in the planning stages of the project. Finally, I must acknowledge Melissa Fox and Robens Jospeh, who have helped me navigate the numerous logistical and financial complexities of this project.

My parents and brother have been the unseen presence that has made everything possible and have been there and back with me helping behind the scenes. Above all, is my gratitude to Matt. In one person, he has been everything - my best friend and role model - and has supported this project from all ways possible.

This work was funded by the following sources: At MIT, the Center for Global Change Science Director's Fund, the Joint Program on the Science and Policy of Global Change, the Martin Family Society of Fellows for Sustainability, and the MIT Energy Initiative and additional funding from the NASA grant supporting the Advanced Global Atmospheric Gases Experiment.

Contents

List of Figures

List of Tables

Chapter 1

Introduction

Long-lived greenhouse gases (LLGHG) are a subject of great concern, due to their strong infrared properties and their ability to persist in the atmosphere on timescales ranging from decades to tens of thousands of years. Three of these LLGHGs, methane (CH_4), nitrous oxide (N_2O) and sulfur hexafluoride (SF_6), are incredibly potent compounds that continue to grow in the atmosphere despite regulation under the Kyoto Protocol.

1.1 Global and Regional Emissions

Between 1978 and 1986, predecessors of the Advanced Global Atmospheric Gases Experiment (AGAGE) began measuring CH_4 and N_2O using the gas chromatograph - multidetector instrument (GC-MD) comprised of a flame ionization detector (FID) and electron capture detector (ECD) [Prinn et al., 2000]. Measurement of SF_6 began in 2003 when it was added to the suite of compounds measured by the 'Medusa' gas chromatograph mass spectrometer (GC-MS) system [Miller et al., 2008]. These compounds were first measured at five monitoring stations: (1) Mace Head (Adrigole prior to 1983), Ireland (MHD) (2) Trinidad Head , California (Cape Meares, Oregon prior to 1989), USA (THD) (3) Ragged Point, Barbados (RPB) (4) Cape Matatula, American Samoa (SMO) (5) Cape Grim, Tasmania, Australia (CGO). Each of these five primary stations were situated to sample oceanic air for a portion of the year for

the purpose of measuring semi-hemispheric 'background' mole fractions and to sample polluted air for a portion of the year for regional emissions estimation. Since the implementation of these stations, other stations have joined AGAGE (Ny-Alesund, Norway; Jungfraujoch, Switzerland; Shangdianzi, China; Gosan, Korea) or affiliated with the network (Monte Cimone, Italy and Hateruma, Japan). At each of these stations, CH_4, N_2O and SF_6 are measured *in situ* and at high-frequency (∼hourly). Calibration of these gases are on the Tohoku University, SIO-98 and SIO-2005 scales, respectively [Prinn et al., 2000].

Figures 1-1 shows CH_4 and N_2O mole fractions measured by AGAGE from 1997 to present and SF_6 mole fractions from 2004 to present. In 2011, the globally weighted mean mole fraction for the three species from AGAGE data was 1803.1 ±4.1 nmol mol^{-1}, 324 ±0.1 nmol mol^{-1} and 7.26 ±0.02 pmol mol^{-1}, respectively (personal communication, M. Rigby, http://agage.eas.gatech.edu [2013]). In all species, the observed latitudinal gradient suggests that emissions sources are larger in the Northern Hemisphere. For CH_4, there is both a strong seasonal cycle and inter-hemispheric gradient of approximately 20 nmol mol^{-1} and 150 nmol mol^{-1}, respectively. In 2007, a sudden increase in the global growth rate of CH_4 was detected, following nearly a decade of little change and the cause of this acceleration is still being investigated [Rigby et al., 2008, Dlugokencky et al., 2009]. In N_2O, the seasonal cycle and inter-hemispheric gradient are approximately 0.4 nmol mol^{-1} and 1 nmol mol^{-1}, respectively, signals which are small compared to its average mole fraction. The main sink reaction for N_2O is destruction by photolysis in the stratosphere. The smaller latitudinal gradient suggests a flatter emissions gradient and/or weaker tropical sink relative to CH_4. SF_6 has only a small seasonal cycle related to variability in transport and an inter-hemispheric gradient of approximately 0.4 pmol mol^{-1}. The primary mechanism for destruction of SF_6 is through photolysis in the mesosphere.

Global emissions of the above species are generally well-constrained, as global growth rates derived from measurements (such as the AGAGE measurements discussed above) and knowledge of sink processes are well-understood (though not completely). Global CH_4 emissions are approximately 582 Tg CH_4 yr^{-1} and the largest

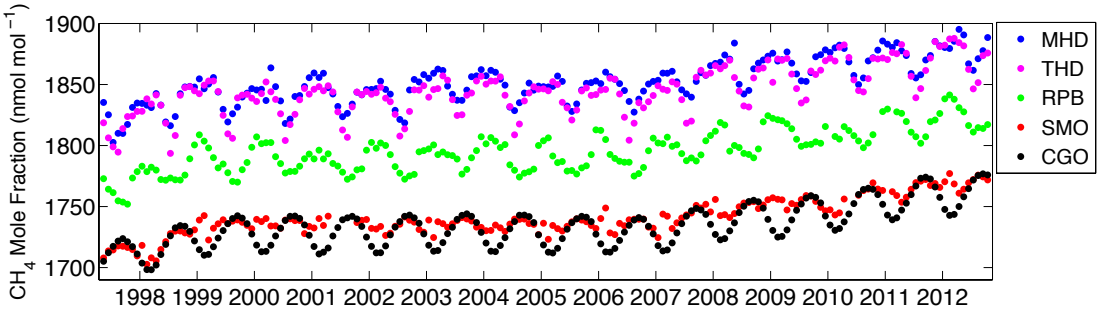

(a) CH_4

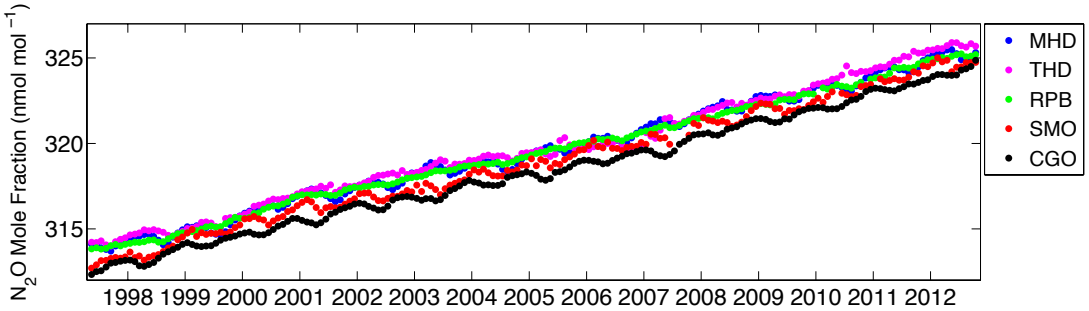

(b) N_2O

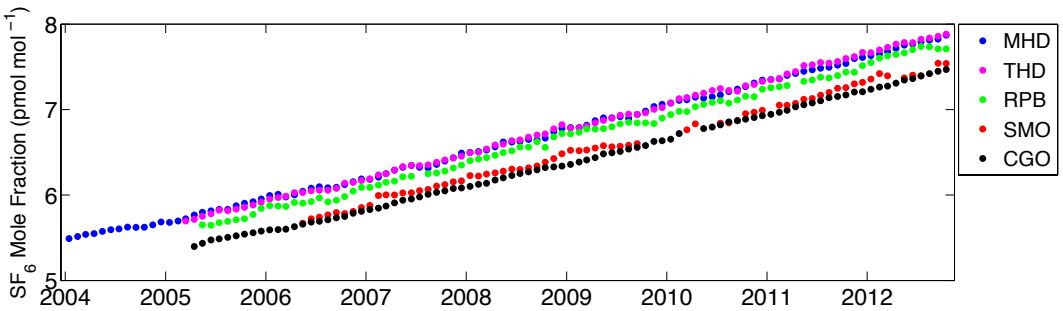

(c) SF_6

Figure 1-1: Monthly mean mole fractions measured by AGAGE at the five primary stations: Mace Head, Ireland (blue), Trinidad Head, California (purple), Ragged Point, Barbados (green), Cape Matatula, American Samoa (red), Cape Grim, Tasmania (black) for (a) CH_4 (b) N_2O and (c) SF_6 [Rigby et al., 2008, Huang et al., 2008, Rigby et al., 2010, http://agage.eas.gatech.edu, 2013]

uncertainties in this value stem from uncertainties in the sink reactions corresponding to ±103, ±15 and ±8 Tg CH_4 yr^{-1} for OH, soil and stratospheric sinks [Denman et al., 2007]. Total N_2O emissions are 17.3 (15.8-18.4) TgN yr^{-1} for top-down estimates, which are assimilated from atmospheric measurements and 17.7 (8.5-27.7) TgN yr^{-1} for bottom-up estimates, which are compiled using proxies (e.g., population density) and emissions factors [Denman et al., 2007]. Though the two show general agreement, a large range in emissions estimates exists and in particular in the bottom-up estimates, reflecting the various methodologies and ancillary data used to compile these inventories [Denman et al., 2007]. Global 2008 top-down SF_6 emissions show good agreement among two studies resulting in estimates of 7.2±0.4 and 7.4±0.6 Gg yr^{-1} [Rigby et al., 2010, Levin et al., 2010]. Table 1.1 summarizes recent publications of top-down emissions estimates for the three gases.

Table 1.1: Selected recent publications with top-down global and regional emissions estimates. Emissions were estimated for the years indicated.

Species	Publications	Global emission rate
CH_4	Chen and Prinn [2005]	500-600 Tg CH_4 yr^{-1} (1996-2001)
	Bergamaschi et al. [2009]	506.7-542.8 Tg CH_4 yr^{-1} (2004)
	Bousquet et al. [2006]	532 ±3 Tg CH_4 yr^{-1} (2008)
N_2O	Huang et al. [2008]	$15.4^{+1.7}_{-1.3}$ TgN yr^{-1}(2001-2005)
	Hirsch et al. [2006]	17.2 ±1.4 TgN yr^{-1} (1998-2001)
SF_6	Rigby et al. [2010]	7.4±0.6 Gg SF_6 yr^{-1} (2008)
	Levin et al. [2010]	7.2±0.4 Gg SF_6 yr^{-1} (2008)

Quantification of regional emissions are much less constrained than the global burden and requires measurements with high sensitivity to air masses containing regional pollution. To date, no concerted measurement campaign has been carried out in India to target the above species at high-frequency. From 1993-2002 and from 2009-present, flasks have been collected in duplicate twice per month at a station in

Cabo de Rama, India (Cape Rama), and analyzed for CH_4 and N_2O mole fraction at the CSIRO[1] in Australia [Bhattacharya et al., 2009]. Previous and ongoing satellite measurements include measurements by SCIAMACHY[2], AIRS[3] and GOSAT[4] [Bergamaschi et al., 2009, Xiong et al., 2009, Parker et al., 2011] . In Xiong et al. [2009], satellite retrievals of CH_4 using AIRS showed a plume-like enhancement of CH_4 over South Asia during the monsoon, suggesting increased emissions and deep convection during this period. Samples collected by CARIBIC[5] flights using commercial aircraft flights operating between Germany and India have also shown a distinct monsoon plume [Schuck et al., 2010]. These plumes contain CH_4, N_2O and SF_6 enhancements due to increased vertical transport from deep convection. Vertical enhancements in N_2O have been measured in HIPPO[6] observations when the origin of air masses was from South Asia, the Western Pacific or Indonesia and suggest an unaccounted-for tropical source [Wofsy, 2011].

Several studies have attempted to quantify regional emissions using global Eulerian models but the typical approach has been to aggregate India and large portions of Asia into a single emitting region [e.g., Chen and Prinn, 2005, 2006, Huang et al., 2008, Rigby et al., 2010]. This aggregation is done for two reasons: (1) for computational efficiency since sensitivities are computed for fewer regions and (2) because uncertainty reduction without a nearby measurement site would be small. Newer approaches using high resolution particle dispersion models have not yet been applied to India, where high-frequency surface data has not existed [Manning et al., 2003, 2011, Stohl et al., 2009, Rigby et al., 2011b]

Of the many global emissions estimates for these gases, only a few have utilized measurements from South Asia. The importance of including Cape Rama measurements from India in regional emissions estimates has been demonstrated in Huang et al. [2008] and Patra et al. [2009]. In Patra et al. [2009], CH_4 emissions from In-

[1]Commonwealth Scientific and Industrial Research Organization
[2]SCanning Imaging Absorption SpectroMeter for Atmospheric CHartographY
[3]Atmospheric Infrared Sounder
[4]Greenhouse gases Observing SATellite
[5]Civil Aircraft for the Regular Investigation of the atmosphere Based on an Instrument Container
[6]HIAPER Pole-to-Pole Observations

dia were deduced (however, not using an inverse framework) using AGAGE, NOAA[7] and CSIRO surface stations, including the Cape Rama dataset. Emissions from India were found to be 41 Tg CH_4 yr^{-1}, which is significantly lower than emissions reported in most global-scale inventories. In Bergamaschi et al. [2009], CH_4 emissions over Asia (including, India, China and Southeast Asia) were estimated using SCIAMACHY (using a CO_2 proxy) and NOAA surface data at ∼130 Tg yr^{-1}. The inversion showed the large spatial and temporal variability in CH_4 source strength within India. However, satellite data over India are often erroneous due to frequent cloud cover, high aerosol optical depth and because retrievals over India based on CO_2 proxies have large uncertainties due to the sparsity of CO_2 measurements in the region. In Huang et al. [2008], inversions for N_2O emissions performed with Cape Rama data showed significant error reduction over the case when Indian measurements were not included. Specifically, inversions performed without the Cape Rama data showed the South Asian source to be 74% larger and the African sources to be 21% smaller than the estimates obtained using the Indian data, indicating that large spatial covariances exist without the use of unique Indian measurements. The results of this study further show South Asian emissions (region encompassing all of the Middle East, Pakistan, Afghanistan, portions of China) to be $0.95^{+0.17}_{-0.20}$ TgN yr^{-1} from 2002-2005. Top-down SF_6 emissions for non-UNFCCC[8] countries, which include India, China, Southeast Asia and parts of the Middle East were estimated to be 4.1 ±0.3 Gg yr^{-1} in 2008, and the majority of these emissions are expected to come from China. An analysis of covariance shows an average correlation of 30% between Asian non-UNFCCC and North American emissions and is the largest correlation derived from the inversion [Rigby et al., 2010]. This implies that the measurements do not contain enough information to constrain the regions independently.

The Indian Network for Climate Change Assessment (INCAA) 2007 report, sponsored by the Government of India, published bottom-up sectoral inventories of CH_4 and N_2O emissions, following the Intergovernmental Panel on Climate Change's 1996

[7]National Oceanic and Atmospheric Administration
[8]United Nations Framework Convention on Climate Change

methodology. According to this inventory, India's emissions in 2007 were 20.5 Tg CH_4 and 240 Gg N_2O (or 150 GgN) [Indian Network for Climate Change Assessment, 2007]. These emissions appear to be smaller than top-down estimates predicted by Patra et al. [2009] and Huang et al. [2008] (estimate includes South Asian countries other than India but it is assumed that the majority of these emissions come from India). Figure 1-2 shows the distribution of emissions by sector from the INCAA report for the two gases. In both cases, the majority of emissions are from the agricultural sector, comprising over 75% of CH_4 emissions and 60% of N_2O emissions. Emissions estimates for SF_6 were not compiled through INCAA.

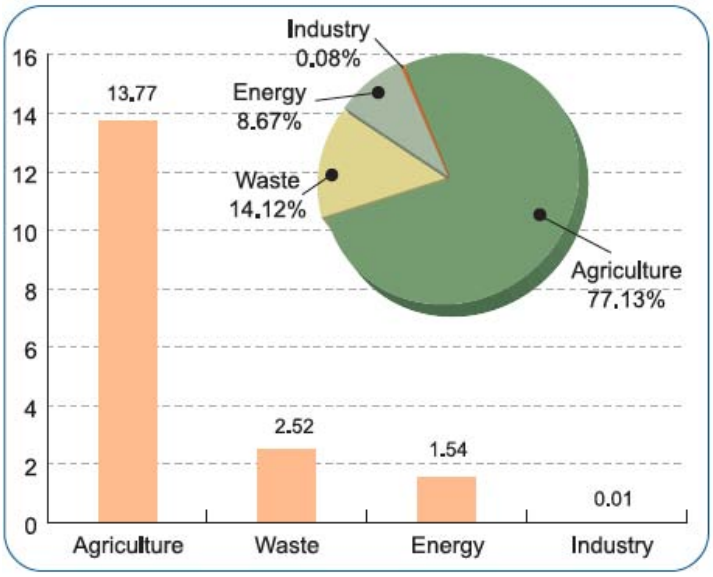

(a)

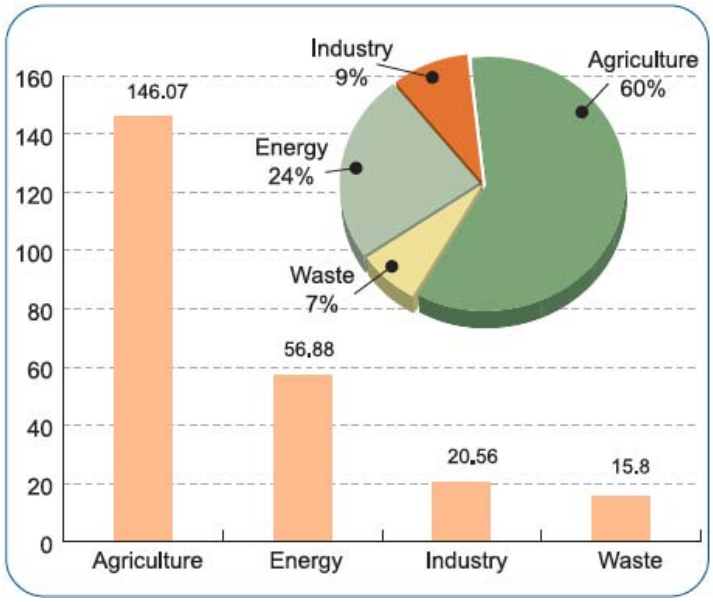

(b)

Figure 1-2: 2007 sectoral emissions from India and percentage breakdown of (a) CH_4 in Tg and (b) N_2O in Gg. Figures from Indian Network for Climate Change Assessment [2007].

1.2 Emissions Sources

Emissions sources are well-known for the three gases but large uncertainties exist in source disaggregation in emissions estimates. Globally, a large fraction of CH_4 emis-

sions are naturally occurring but anthropogenic sources dominate with 60% of the CH_4 budget [Denman et al., 2007]. It is further thought that natural emissions of CH_4 maybe be accelerating with increased warming. Natural sources of CH_4 include boreal and tropical wetlands, volcanoes, natural fires and termites. Inverse methods have implicated tropical wetlands as the primary driver of the 2007 growth anomaly but this finding does not appear to be consistent with CH_4 emissions simulated from some wetland models [Bousquet et al., 2011, Spahni et al., 2011]. Anthropogenic sources are rice paddies, ruminants, natural gas, biomass burning, sewage and others [Denman et al., 2007]. In India, almost 50% of CH_4 emissions are through enteric fermentation and approximately 20% through rice cultivation. Natural sources are a smaller component of total emissions [Indian Network for Climate Change Assessment, 2007].

The principal source of N_2O globally is naturally occurring from tropical soil and oceanic emissions primarily through nitrification and denitrification and accounts for approximately 60% of the budget. The remainder of emissions is anthropogenically driven through the usage of fertilizers in agricultural soils, from biomass burning, sewage, transportation and other smaller sources. In India, almost 60% of N_2O emissions are from agricultural soil emissions [Indian Network for Climate Change Assessment, 2007].

Studies of SF_6 from firn air measurements have shown only a small pre-industrial concentration of 6 x 10^{-3} pmol mol^{-1}, suggesting that SF_6 is almost entirely anthropogenically emitted [Deeds et al., 2008]. Primarily, emissions are from the electrical industry as it is used as a dielectric in high-voltage switchgear and is released through leakage and during the maintenance and refill process [Niemeyer and Chu, 1992]. Other minor sources are emission during magnesium and aluminum production and during semiconductor manufacture [Maiss and Brenninkmeijer, 1998]. SF_6 is often used as a tracer in geophysical applications owing to its stability and easy detection.

1.3 Chemical Properties

CH_4 has the the second largest direct radiative forcing contribution at 0.48 $\pm$0.05 Wm^{-2}, only behind carbon dioxide (CO_2) [Forster et al., 2007]. The main sink for CH_4 is reaction with the hydroxyl radical (OH), resulting in an atmospheric lifetime of approximately 9 years. However, indirect radiative effects caused by the feedback between CH_4 lifetime and OH concentration result in an increased lifetime of 12 years. These additional indirect effects include the coupled reaction pathways with tropospheric ozone, the production of stratospheric water vapor and its chemical oxidation to CO_2. In total, the direct and first three indirect effects result in a radiative forcing of 0.86 Wm^{-2} and a 100-year global warming potential (GWP) of 25 [Shindell et al., 2005, Forster et al., 2007]

N_2O is an important greenhouse gas and ozone-depleting substance with a radiative forcing contribution of 0.16 Wm^{-2} in 2005 [Forster et al., 2007]. Based on current mole fractions, its radiative forcing has exceeded that of chlorofluorocarbon-12 (CFC-12), now making it the third largest contributor. In addition, N_2O plays an important role in the chemistry of the ozone layer and is the primary source of stratospheric NO_x. Ravishankara et al. [2009] found N_2O to be the most important ozone-depleting substance in the 21st century. Though its ozone-depletion potential (ODP) is low (0.017), the large atmospheric burden and long lifetime make N_2O the largest ODP-weighted emitter. N_2O is inert in the troposphere; in the stratosphere, photolysis and reaction with $O(^1D)$ are the primary sink mechanisms, which result in an atmospheric residence time of 114 years (131 years in Prather et al. [2012]) [Forster et al., 2007].

SF_6 is the most potent greenhouse gas regulated under the Kyoto Protocol. It is notable for its strong greenhouse properties with a GWP of 22,800 and lifetime of 3,200 years, making it essentially inert on human timescales. Its long lifetime owes to the fact that destruction of SF_6 only occurs in the mesosphere [Forster et al., 2007].

Atmospheric lifetime, global warming potential and radiative forcing of the three gases are summarized in Table 1.2.

Table 1.2: Atmospheric lifetimes, global warming potentials and radiative forcing contributions of three LLGHGs (Forster et al. [2007], Shindell et al. [2005])

Species	Lifetime (years)	100-yr GWP	2005 Radiative Forcing (Wm^{-2})
CH_4	12	25	0.48
N_2O	114	298	0.16
SF_6	3200	22800	0.0029

1.4 Research Goals

The large range and uncertainties in emissions estimates from South Asia primarily result from a lack of atmospheric measurements in the region. While the AGAGE stations in China, South Korea and Japan are able to provide information on East Asian emissions, a measurement station sampling Indian air is required for dedicated emissions estimation from South Asia. Furthermore, a station sampling in high-frequency (∼hourly) has the benefits of providing significant error reduction in emissions estimation, discerning intra- and inter-annual variability and identifying pollution events amidst 'background' signal. The major objectives of this thesis are to:

- Develop instrumentation for high-precision, automated monitoring of three important greenhouse gases, CH_4, N_2O and SF_6. This instrument is closely linked to the AGAGE network through shared standards, and through similar equipment and data protocols. Data quality is closely monitored by computing the daily repeatability of standards measured each day, through monitoring of non-linearities, and through monitoring of drift in the calibration standard, amongst other metrics. Details are found in Chapter 2.

- Develop a new Indian field site adequate for carrying out this study. The field site chosen for this study is located in Darjeeling, West Bengal, India and is

housed by the Bose Institute's High Altitude Research Center. While basic site infrastructure was already in place, additional modifications were made for implementation of the instrument developed in this thesis. Site characterization is found in Chapter 1 and details of site modifications are found in Chapter 2.

- Collect high-frequency measurements of CH_4, N_2O and SF_6 from Darjeeling, India for a period of at least one year, thereby measuring signals over a full annual cycle. With this dataset, diurnal and seasonal features are identified, including discussion of the type and magnitude of variability that is measured over a year. Details are found in Chapter 4.

- Use a Lagrangian Particle Dispersion Model to create air history maps for Darjeeling, India and characterize the ability of the chemical transport model to accurately capture flow in the Himalayas. Model-simulated and observed wind fields are compared. Additionally, the effect of particle release height and model resolution are used to diagnose the robustness of the chemical transport model and to determine the sensitivities of the model to these important parameters. Details are found in Chapters 3 and 5.

- Develop inverse modeling framework for emissions estimation and deduce emissions estimates with resulting uncertainties. Using air history maps created by the Lagrangian Particle Dispersion Model, a Quasi-Newton method is used to estimate monthly emissions fields and boundary conditions, optimized from an *a priori* emissions field. Details are found in Chapter 5.

1.5 Site Selection

The field site selected for this study is located in the Himalayan foothills at Darjeeling, West Bengal, India and is housed at the Bose Institute High Altitude Research Center (27°02'N, 88°15'E, 2194 meters above sea level, Figure 1-3, Chatterjee et al. [2010]). The location of Darjeeling was primarily selected for its high sensitivity to Indian/South Asian air masses year-round along with high sensitivity to air masses

passing over agricultural zones during the Southwest Monsoon when CH_4 and N_2O emissions are expected to peak. The primary rice-growing season occurs during this period as much of India's rice cultivation is rain-fed. Figure 3-2 shows 'surface influence' for each season, a metric that is indicative of the regions from which emissions would be sampled at Darjeeling. These maps show Darjeeling's high sensitivity to surface air from the Indo-Gangetic plains of India, an area with the highest human and cattle population density and where rice cultivation is significant. The second criteria was altitude. In the absence of constructing a tall tower, sites at high altitude sample air from a greater distance and have a larger extent of 'surface influence'. The third criteria was for the site to be located in a region of low emissions, so that measured signals are not dominated by local processes. As shown in Figures 5-5 and 5-6, CH_4, N_2O and SF_6 emissions are low relative to the nearby Indo-Gangetic plains, which are approximately 50km from Darjeeling. The final criteria was for adequate site infrastructure. The Bose Institute offered the best local support and demonstrated interest in contributing to the project. Bose Institute's High Altitude Research Center in Darjeeling is comprised of several buildings, on-site guest rooms, existing power and internet access, availability of a generator and local technical support. The local support is one of the most crucial elements of a field project and was a considerable factor when choosing this site. A technician (Mrs. Yashodhara Yadav) was trained to operate the instrument and deal with routine procedures such as changing gas cylinders, monitoring instrument function and shutting down the instrument safely during severe power outages. Furthermore, the technician was able to learn non-routine procedures as well, such as measuring battery voltages in the uninterruptible power supply, replacing faulty parts and dealing with computer issues. This technician support has proved invaluable to the project.

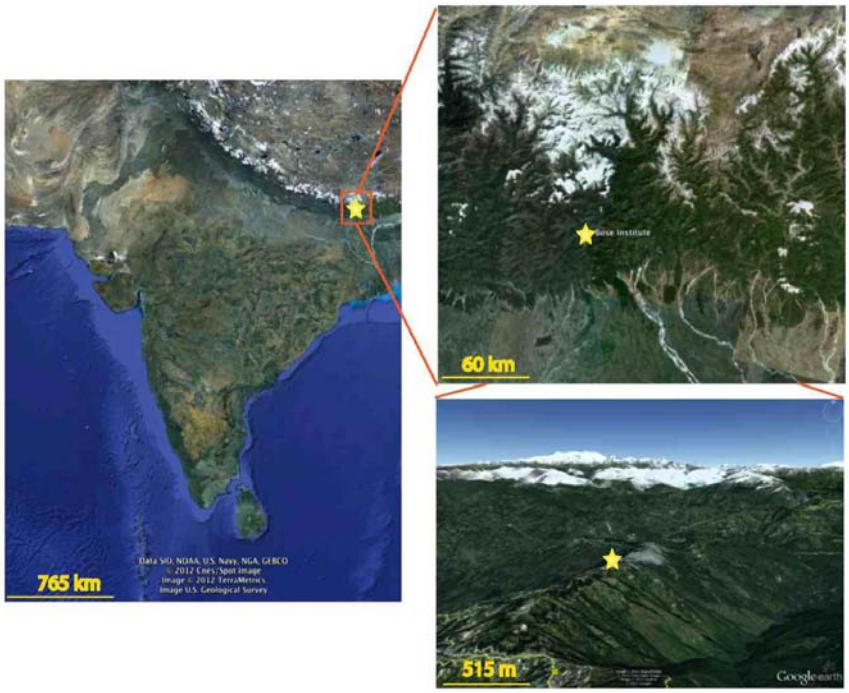

Figure 1-3: Location of field site in Darjeeling, West Bengal, India (27°02'N, 88°15'E, 2194m), showing its location in the Himalayan foothills of Northeast India. Images are from Google Earth.

1.6 Site Characterization

Darjeeling is a small Indian town with a population of ∼100,000 developed on the Northwest facing slope of a Northeast-Southwest ridge (Figures 1-3, 1-4). The main town center in Darjeeling is located at ∼2000 masl, approximately 200m below the station and 250m below the ridgetop. It is located ∼50km north of the Indo-Gangetic Plains. The area surrounding Darjeeling is typical of the terrain of the Eastern Himalayas and is heavily forested. The region on the slope below Darjeeling contains several tea plantations, where synthetic nitrogen fertilizers are used seasonally and could contribute to a local source of N_2O. Wood biomass burning is prevalent throughout the mountain region and mainly during the winter season, which may contribute to local sources of CH_4 and N_2O. Additionally, there may be small natural gas sources in the town, another potential local influence on CH_4. Vehicular emissions also exist, mainly from tourist vehicles which operate predominantly on diesel fuel, though

the contribution to CH_4 and N_2O is thought to be small. Local sources of SF_6 are expected to be small. The nearest transformer is located in Ghoom, approximately 10km away from Darjeeling, though leakage could occur from this transformer.

The measurement station is located in a relatively unpopulated portion of Darjeeling and is in a wooded area (Figure 1-4a). There is one road that leads to the Bose Institute and continues further upslope to a Japanese Temple where the road ends. As a result, there is very little vehicular traffic on this road.

(a)

(b)

Figure 1-4: (a) Location of the instrument at the Bose Institute in Darjeeling, as seen from the road below. The site is located in a wooded area above the town. (b) Town of Darjeeling, located 200m below the Bose Institute.

1.6.1 Synoptic and Mesoscale Meteorology

The synoptic meteorology of South Asia varies considerably with season and is illustrated by the climatology of the 850 and 200 mb wind fields (Figure 1-5) [Kalnay et al., 1996]. The winter months (Dec - Feb) are characterized by relatively stagnant, dry surface air and upper level westerlies. Temperatures fall below freezing in the Himalayan region where snow can be prevalent, while temperatures in other parts of India are mild due to the barrier the Himalayas form against cold, Arctic air. The pre-monsoon or summer period (March - May) is the hottest time of the year in the plains of India when thunderstorms are widespread and frequent. Humidity begins to rise during this time and continues into the monsoon season (June-Aug), which is

characterized by strong southwesterly flow (known as the Southwest Monsoon). The onset of this period begins in June when the temperature gradient between the subcontinent and surrounding ocean is the largest. As a large low-pressure system forms over the land, air moves in from the warm tropical ocean, bringing with it copious amounts of moisture. Air passing over the heating land mass reaches the Himalayas, where it is effectively blocked and rises to form upper level easterlies, closing this Walker-type cell. Figure 1-6 shows the climatology of vertical motion during the Southwest Monsoon and illustrates this strong upward motion in the Himalayas. A positive feedback results from latent heat released from the condensation of rising moist air, which in turn cools the land mass further and results in stronger winds. An implication of this sustained monsoon period is that the summer months are the primary rainy season for most of India except for southeastern India. Furthermore, during the summer, the Intertropical Convergence Zone (ITCZ) shifts northward and results in the transport of Southern Hemispheric air to India. The following autumn or post-monsoon months (Sept-Nov) are known as the Northeast Monsoon, which is the retreating flow of the summer monsoon. In a reverse fashion, the land mass cools faster than the surrounding ocean, resulting in a negative temperature gradient between land and the ocean causing air to flow from the Himalayas to the ocean. For most of India, this is characterized by dry, subsiding air with weaker winds than the summer monsoon. For Southeast India, this air first passes over the Bay of Bengal and results in copious rain for this part of the country.

The mesoscale meteorology of the eastern Himalayas plays a large role in the signals measured in the greenhouse gas mole fractions at Darjeeling. One of the more dominant regional flows are the slope winds that occur in mountainous terrain. The slope wind system in a typical mountain setting is governed by upslope/downslope, up-valley/down-valley and plains-to-mountain winds that result from horizontal pressure gradients caused by the heating or cooling of sloping surfaces [Whiteman, 2000]. The typical slope wind system is governed by four periods: morning transition, daytime (coupled), evening transition and nighttime (decoupled) and is illustrated in Figure 1-7.

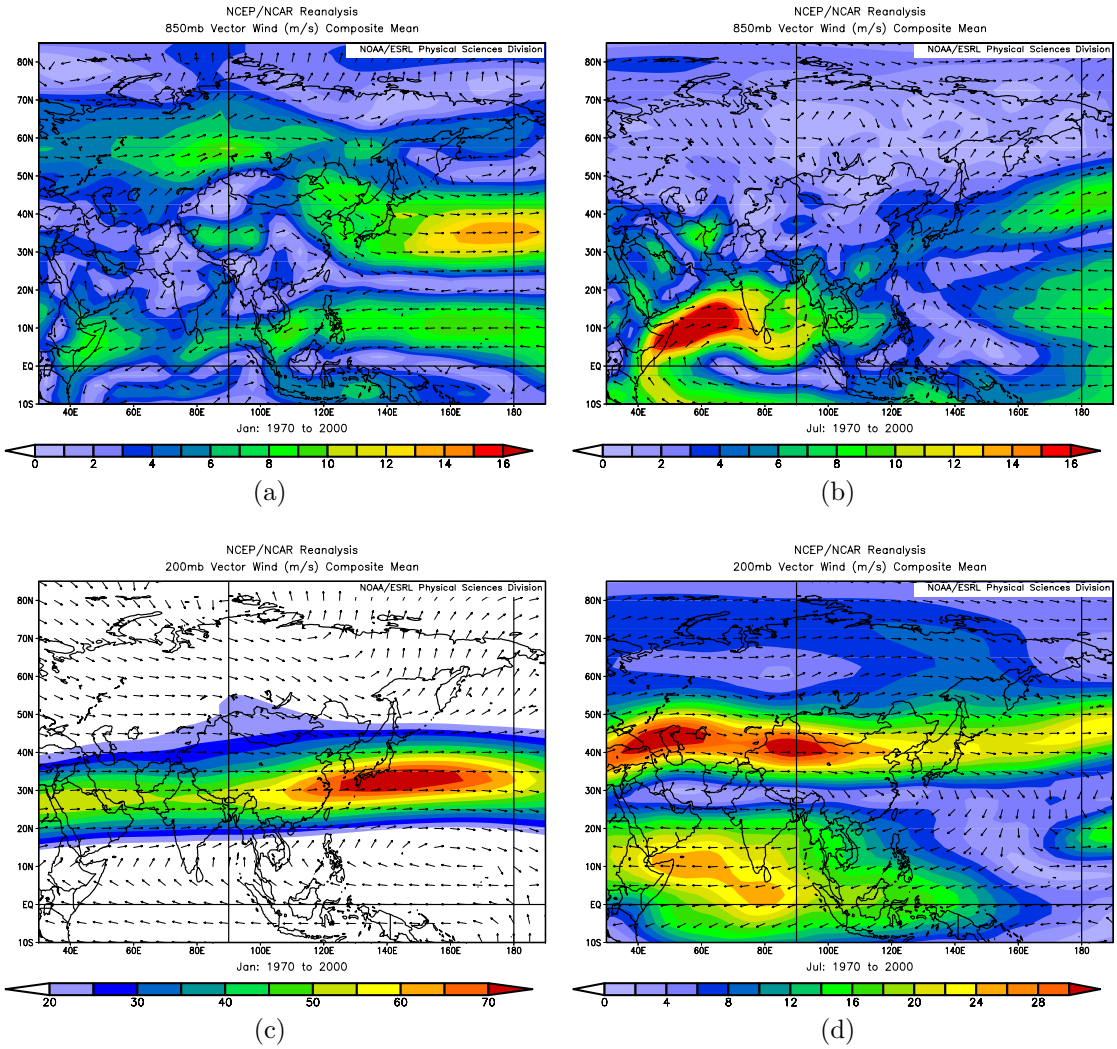

Figure 1-5: Climatology of wind speeds and direction from 1970-2000 for the (a) 850 mb level in January (b) 850mb level in July (c) 200mb level in January (d) 200mb in level July. Colorbar indicates wind speed (m/s) and vectors show wind direction. Figures provided by the NOAA/ESRL Physical Sciences Division, Boulder Colorado from http://www.esrl.noaa.gov/psd/ [Kalnay et al., 1996].

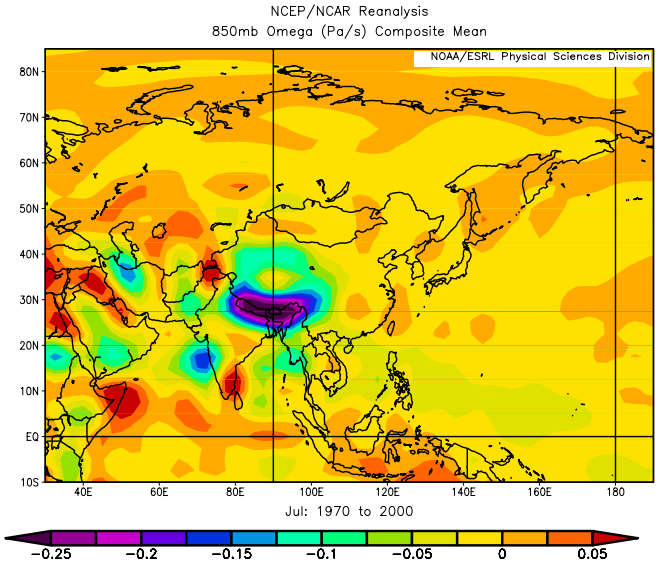

Figure 1-6: Climatology of vertical wind speed from 1970-2000, showing strong vertical motion (Pa/s) over the Himalayas during the July monsoon. Figure provided by the NOAA/ESRL Physical Sciences Division, Boulder Colorado from http://www.esrl.noaa.gov/psd/ [Kalnay et al., 1996].

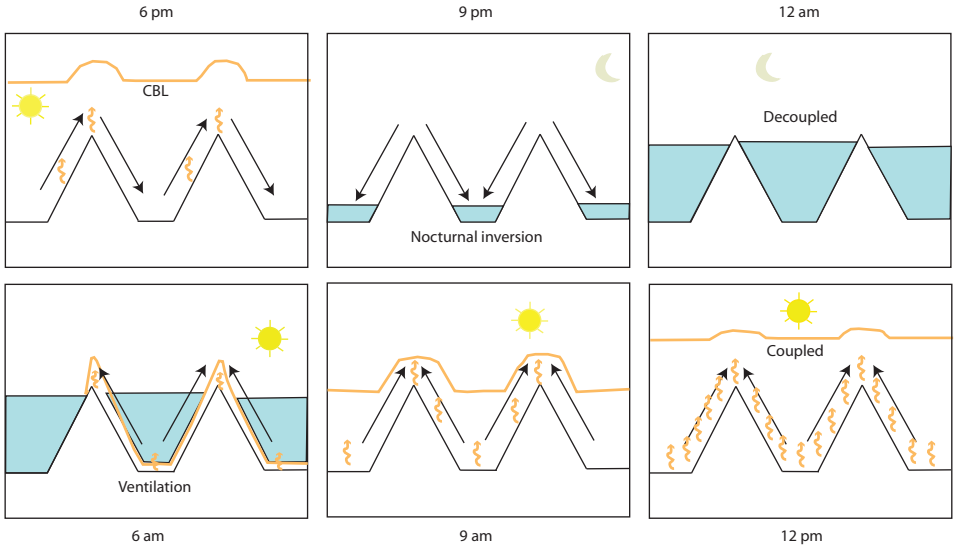

Figure 1-7: Schematic of the diurnal flows occurring in a typical mountain system, showing position of the convective boundary layer and nocturnal inversion layer. Schematic is adapted from Whiteman [2000].

The discussion begins during the day with maximum daytime temperatures occurring around 2-3 pm. The boundary layer height is at its daily maximum and air is considered coupled with the air above the mountain. Maximum upslope and up-valley wind speeds occur at this time in an unstable boundary layer and pollutant transport is the largest. Wind speeds are generally uniform within the mixed layer but as the layer grows, become influenced by winds aloft. The evening transition period begins around sunset, which typically occurs in Darjeeling between 5-6 pm. As the mountain surface cools, sensible heat is transferred from the air to the surface, resulting in a reversal of flow to down-slope and mountain-to-plains. As the valley air becomes stable, along-valley winds shift from up-valley to down-valley. The boundary layer height decreases until night, when it is at its daily minimum. As the boundary layer height decreases and air becomes stably stratified, a nighttime inversion is formed below the mountaintop and winds become weak. The nighttime air is decoupled from air aloft. For a station above this inversion layer (or for gases that have no sources within the valley), minimum pollutant concentrations are measured at night. This is of course the opposite scenario for a station measuring urban pollutants in a valley, where the stable nighttime air would lead to maximum concentrations at night. The morning transition period occurs just before sunrise as the surface of the mountain begins to warm. Sensible heat flux is transferred from the surface to the air just above the surface. Due to the horizontal pressure gradient that results from the slope of the mountain, air just above the surface rises and adjacent air moves in, resulting in upslope flows. The nighttime inversion begins to break up through convective currents in the heating air and the boundary layer begins to grow. While the mechanism of slope flows are well-known, many factors can affect these thermally-driven winds. Cloud cover, moisture and snowfall can modulate the amount of radiation received at the surface. Strong winds above the mountain can dominate over the slope winds when the mountain system is coupled with air aloft. West-facing slopes (such as Darjeeling) have delayed sunrise, which affects the onset of upslope flows.

Meteorological Observations from Darjeeling

Figure 1-8 shows median daily profiles of air temperature and barometric pressure measured at Darjeeling for January and July using meteorological sensors discussed in Appendix A. Air temperature typically maximizes around 2 pm and minimizes around 3 am. During the summer, median air temperature is around 17°C during the day and 15.5°C at night, while winter temperatures are at 5°C during the day and 2°C at night. In both seasons, only a relatively small difference in daytime and nighttime air temperatures is observed, suggesting that air temperature is modulated by cloud cover and humidity.

In contrast to the diurnal structure of air temperature, barometric pressure varies semi-diurnally, which is consistent with the profile expected in the tropics. The semi-diurnal nature results from a thermal forcing that stems from water vapor and ozone absorption in the upper atmosphere and which only occurs for half the day (zero for remainder of the day). The forcing is thus not purely diurnal and can be decomposed into diurnal and semidiurnal (and higher frequency) modes. In both the extra-tropics and tropics, the diurnal mode is not observed but for different reasons. In the extra-tropics, most of the diurnal forcing is in trapped modes that cannot vertically propagate to the surface. In the tropics, the propagating diurnal mode has a short vertical wavelength, which is prone to interference. In both cases, the semi-diurnal mode propagates to the surface, however, synoptic scale variability in the extra-tropics dominates the signal and the small semi-diurnal effect is not observed. At Darjeeling, a semi-diurnal cycle in barometric pressure is clearly observed and occurs year-round. The first maximum occurs around 10am and a second maximum occurs at 10pm.

Wind speed and wind direction were continuously monitored and are important metrics used to diagnose features in the trace gas measurements. The most prominent feature is the diurnal shift in wind direction during the winter and the lack of diurnal winds during the summer. Furthermore, wind speeds peak during the pre-monsoon of March/April when widespread storms occur in Northeast India and are weak during

the monsoon when vertical motion in the Himalayas is strong. Wind roses containing wind speed and wind direction for different times of day and season are discussed further in Section 3.4.

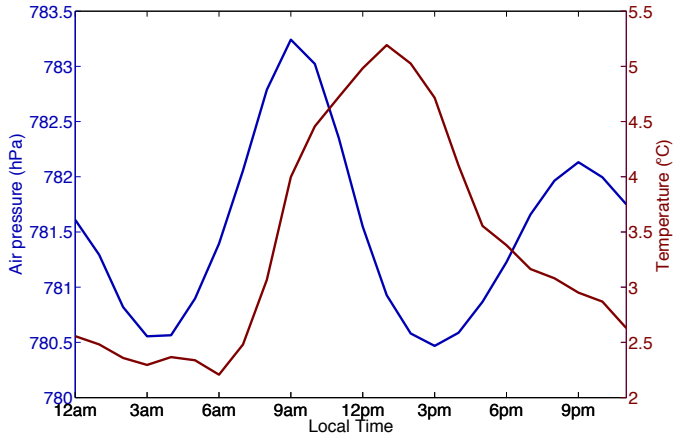

(a)

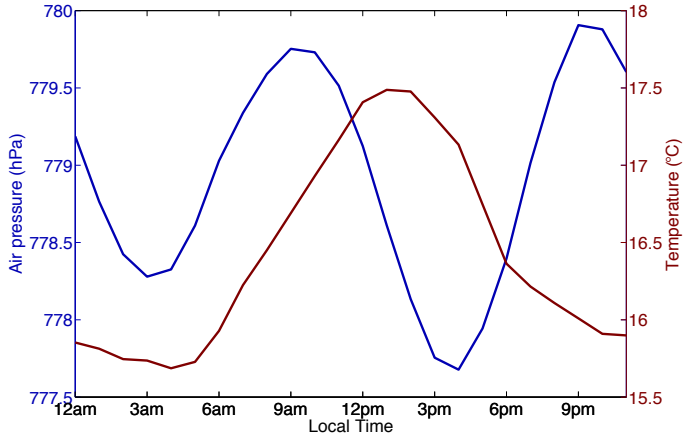

(b)

Figure 1-8: Observed median air pressure (hPa, blue) and air temperature (°C, red) for (a) January 2012 and (b) July 2012 showing a diurnal structure in air temperature and semi-diurnal structure in barometric pressure.

Chapter 2

Instrument for High-Frequency Measurement of CH_4, N_2O and SF_6 Mole Fractions

This chapter presents the instrument and field site setup for measurement of CH_4, N_2O and SF_6 mole fractions in Darjeeling, India. In Section 2.1, instrument design and operation are discussed. Section 2.2 assesses the performance and robustness of the instrument with particular attention to repeatability, non-linearities and memory artifacts. Finally, implementation of the instrument and the field site setup are discussed in Section 2.3.

2.1 Instrument Design

A fully automated, custom-built sampling system was developed and integrated with a gas chromatograph (GC) equipped with a flame ionization detector (FID) and micro electron capture detector (μECD, hereby referred to as ECD) to measure CH_4 (FID), N_2O and SF_6 (ECD). Development of the instrument was based on similar designs developed by Hall et al. [2007, 2011], Dlugokencky et al. [2005], Moore et al. [2003], and Prinn et al. [2000] but improved design features will be discussed. Manufacturers for all major parts can be found in Appendix A.

To begin, the air sample is pumped into the instrument using a custom-built pump module as shown in Figure 2-1. The inlet consists of an inverted titanium cup with monel metal mesh covering and a 1/2" bulkhead union. The inlet line is 1/2" OD Synflex Type 1300/Dekabon tubing drawn from the inlet cup to the pump module. An oscillating aquarium-style pump continually flushes the line at 12 L/min to prevent buildup of condensation and to reduce the residence time between the sampling point and the instrument. The residence time of the line is approximately 30 seconds. The flushing pump contains components that could contaminate the air sample so the line is split upstream through a 7 micron filter and to a diaphragm pump that is switched on only during sampling. Air and any water that may have condensed in the line passes through this pump and into a water trap. This trap has a dip tube configuration, where water droplets fall to the bottom and air fills an outer tube that is connected to the instrument. Finally, water and the bulk of air passes through a back pressure regulator where the majority of the flow is vented at 2 L/min. Only a small amount of sample is introduced into the GC system at 100 mL/min. Two flow meters and a pressure gauge are used to monitor pump function and to set the appropriate flow rates.

The 'sample module' is an aluminum enclosure split into two chambers, with one chamber that is thermostatted to 35°C and one that is held at room temperature (Figure 2-2). The heated chamber houses five valves with micro-electric actuators, sample loops, micrometering valves, a Nafion dryer, and inlet ports to the instrument. It is thermostatted to minimize variations in the amount of sample measured in the air sample and standard. Heating and thermostatting of this chamber is accomplished by using one of the GC's heated zones, which supplies a modulated voltage to coiled resistance wire. A small computer fan circulates air within the enclosure to make sure the space is evenly heated and the heated chamber is fully insulated with neoprene. The rear, unheated, chamber contains all valve electronics .

The carrier gas for the FID is N_2 at a purity of 99.999% and for the ECD is a 10% CH_4 in Argon mixture (P-10) at a purity of 99.995% (relative to the mixture). H_2 at 99.999% purity is supplied to the FID along with zero air from a pure air generator

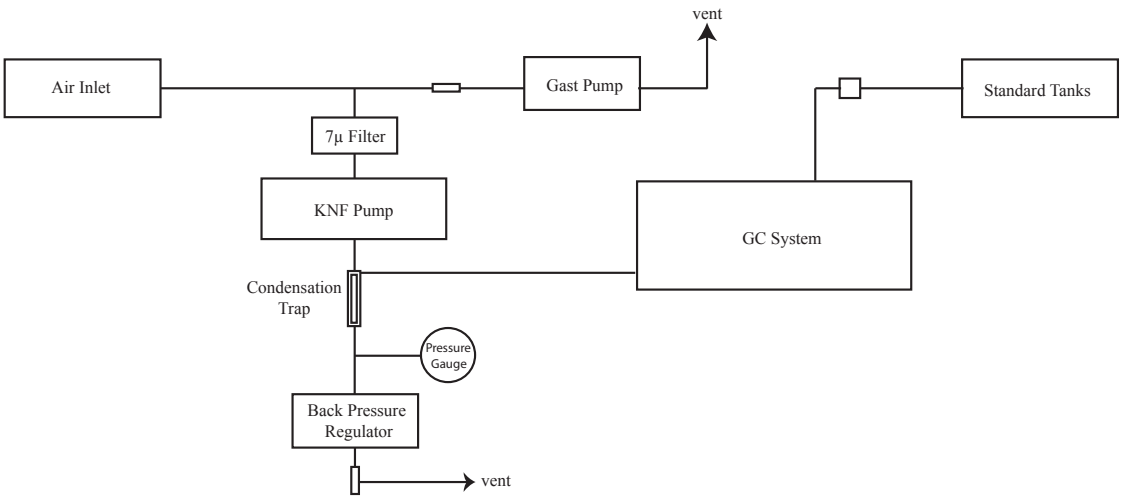

Figure 2-1: Flow diagram of the air and standard intake system, including the configuration of the pump module. The Gast pump continuously flushes the line, while the non-contaminating KNF pump draws air into the instrument for analysis for 45s every 20 minutes.

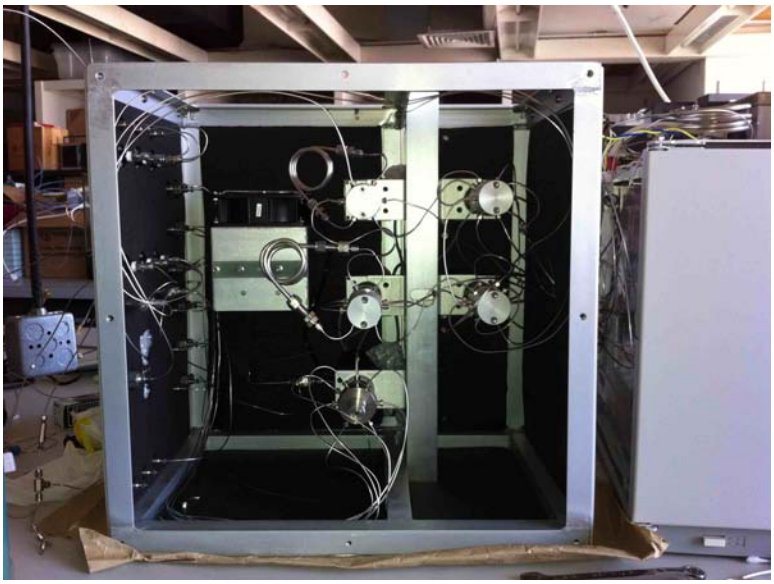

Figure 2-2: The sample module containing valves, sample loops, Nafion dryer and inlet ports is held at 35°C to correct for any variations in sample amount between the air sample and standard.

equipped with a CH_4 reactor. Carrier gases for both channels and H_2 are supplied to the instrument through 1/8" copper tubing and zero air is supplied to the FID through 1/4" 316 stainless steel tubing. Moisture traps are fitted on both the N_2 and P-10 gases. Additionally, a heated gas purifier is used on the P-10 gas to remove trace amounts of O_2. The purity of the gases with inclusion of these traps was determined to be of sufficient quality as it did not adversely impact instrument sensitivity or repeatability of the measured species.

Flow control for all carrier and fuel gases is achieved by the use of the electronic pressure control (EPC) units built into the GC, which sets the head pressure to the columns. Flow control for the sample and standard are achieved using non-lubricated Viton seal micrometering valves. The five micro-electric actuated valves contain purge housings to prevent introduction of ambient air during valve switching and utilize a flow of N_2 (that also flushes the FID columns but by design, does not encounter sample) at 20 mL/min.

A detailed schematic of the GC system is found in Figure 2-3. Unless indicated, 1/16" 316 stainless steel tubing is used for all connections. A 6-port stream selection valve (SSV) with 12-port actuator selects between air sample and standard, alternating between the two to produce a calibrated measurement, and directs to stream to a Nafion dryer, which uses a countercurrent gas of zero air supplied by the pure air generator. Sample loops for the FID and ECD channels of 1.5 mL and 9 mL respectively, are continuously flushed and filled with the sample for 45 seconds at 100 mL/min. At this time the SSV is closed and the sample is allowed to equilibrate with ambient pressure for 30 seconds. A coiled length of tubing separates the two systems (FID and ECD) so that there is no possible backward mixing of CH_4 from the P-10 carrier gas into the FID system. Additionally a coiled length of tubing is placed at the end of the sample stream so there is no diffusion of ambient air back into the sample loops.

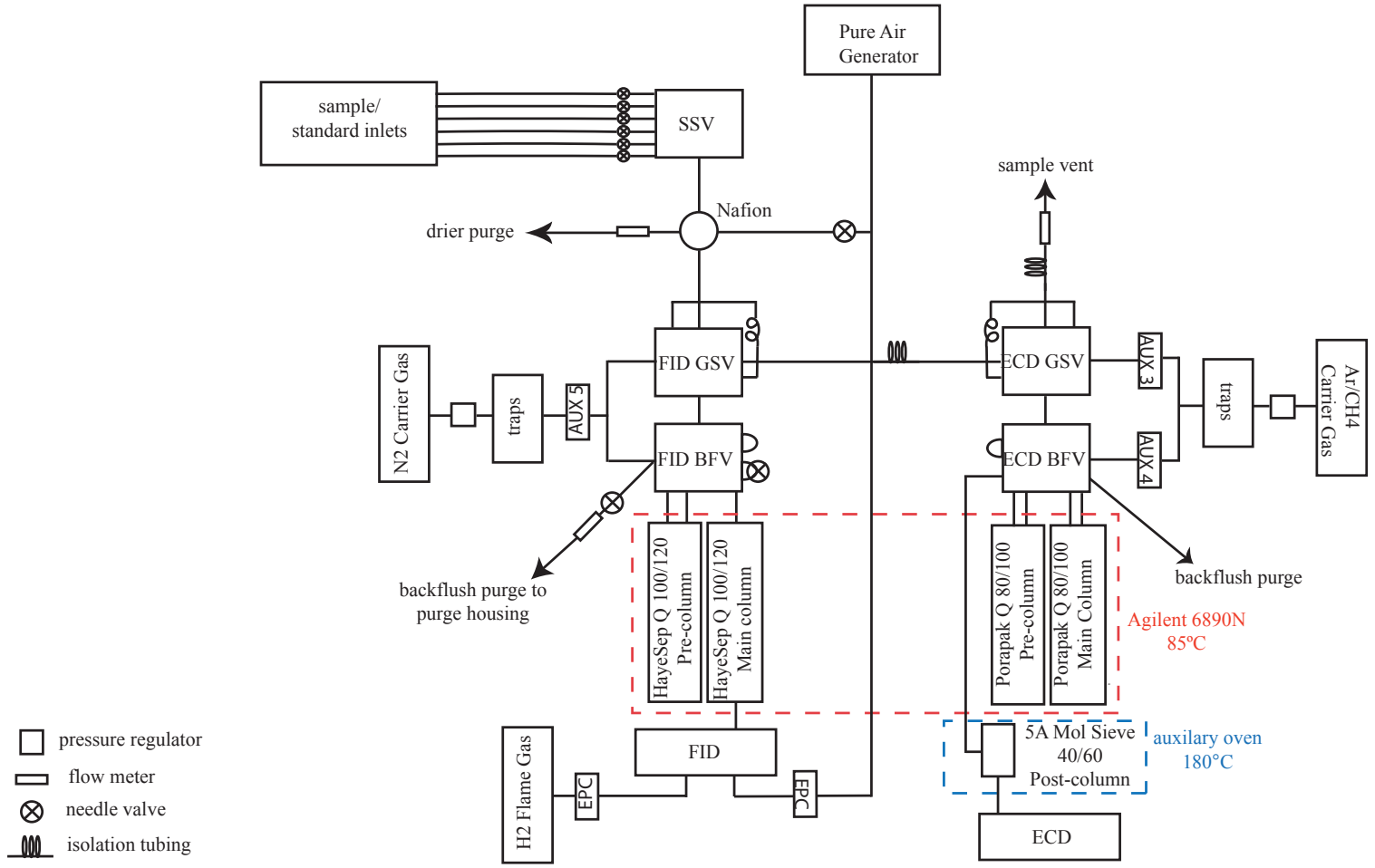

Figure 2-3: Flow diagram containting components and connections of the GC-FID/ECD system. Air or standard is selected using a stream selector valve (SSV) which fills each sample loop. Each system contains a gas sampling valve (GSV) and a back flush valve (BFV) to control the chromatographic separation. The red box shows which columns are contained within the GC, held isothermally at 85°C and the blue box represents a custom-built column oven held at 180°C.

Though analysis with the FID and ECD are done simultaneously, each channel will be discussed separately. Tables 2.1, 2.2 and 2.3 summarize the relevant parameters for the chromatographic setup. Flow rates and column temperatures were varied to determine the optimal response to minimize repeatability errors and will be discussed further. After the FID sample loop has equilibrated, the sample is injected through a 10-port 2-position gas sampling valve (GSV) onto a HayeSep Q 100/120 pre-column (3', 1/8" OD) and main-column (6', 1/8" OD). (Note: A 8-port valve would be sufficient for this operation.) After CH_4 has eluted off the pre-column, the GSV is switched to the backflush position where the pre-column is backflushed and CH_4 continues through the main-column to the FID. The column flow rate is 40 mL/min and backflush flow rate is 20 mL/min. The flame is supplied by H_2 at 60 mL/min and zero air at 275 mL/min. The column temperature is held isothermally at 85°C and the FID at 190°C. Air from the pure air generator is delivered through a 6L ballast volume that allows for mixing of the air prior to entering the FID and thus minimizes any fluctuations in oxygen levels in order to keep the flame steady.

For the ECD channel, the sample is injected after equilibration through a 10-port 2-position GSV onto a Porapak Q 80/100 pre-column (1', 3/16" OD) and main-column (2', 3/16"OD), where N_2O and SF_6 are separated from air. After oxygen passes through these columns, it is 'heart-cut' out to the vent, upon which the, GSV is switched and the pre-column is backflushed while N_2O and SF_6 continue through the main-column and onto a third Molecular Sieve 5Å 40/60 post-column. On the post-column, the order of elution of N_2O and SF_6 is reversed so that SF_6 is detected before the much larger N_2O peak, to improve the SF_6 response. N_2O co-elutes with CO_2 on this post-column. This third post-column is contained in a custom-built oven that is controlled and modulated by the GC using one of the GC's heated zones. The pre- and main- columns are maintained at 85°C to maintain consistency with the FID system, the post-column is held at 180°C and the ECD detector temperature is 340°C. Column flow is 35 mL/min during the heart-cut, increased to 40 mL/min through the post-column and is 30 mL/min during backflush. ECD valve configurations are shown in Figure 2-4. P-10 exhaust is vented outside the lab to prevent any accidental

contamination of CH_4.

Column and flow parameters were optimized to maximize repeatability for the three gases. The combinations of oven temperature and flow rates are used to balance resolution and peak broadening. Narrow peaks with sufficient separation typically have the smallest repeatability errors. Peak broadening, which decreases the signal-to-noise of the peak response, increases when components move slowly through the column. On the other hand, resolution improves when components move slowly through the column. Higher oven temperatures and flow rates result in narrower peaks but decreased peak separation. Furthermore, the separation of N_2O and SF_6 occurs in opposite directions on the Porapak and Molecular Sieve columns because the order of elution is reversed on the Molecular Sieve column. Cooler pre- and main column temperatures (and/or slower flow rate) increase separation of N_2O and SF_6 on the Porpak columns and further separation is then required on the Molecular Sieve to compensate. Other factors to consider include possible oxidation of CO to CO_2 on the Porapak columns at high oven temperatures (though this is addressed in section 2.2.2) , oxidation of the columns at high temperature and conservation of carrier gas. These considerations were all made in optimizing flow rates and oven temperatures, while accommodating the requirement for the FID and ECD oven temperatures to be the same. Parameters were varied until the optimized values (in terms of the above considerations as well as maximizing repeatability) were reached.

Several components are able to be controlled remotely via incorporation of relays. The diaphragm pump, gas purifiers and the pure air generator are switched on and off via relays that are controlled through auxiliary 'valves' 5-7 of the GC using an external events cable. Valves 5 and 6 (pump, purifiers respectively) are 24VDC, 30 mA sources that are used to drive the relays. Valve 7 is simply a contact closure and thus, an additional 24VDC, 100 mA power supply is used to trigger the relay when the circuit is closed via the contact closure. The pump is switched on during sampling for approximately one minute every twenty minutes via a solid state relay. The purifier and pure air generator use mechanical relays where the default ('on') position of the device corresponds to the 'off' position of the valve. These are only

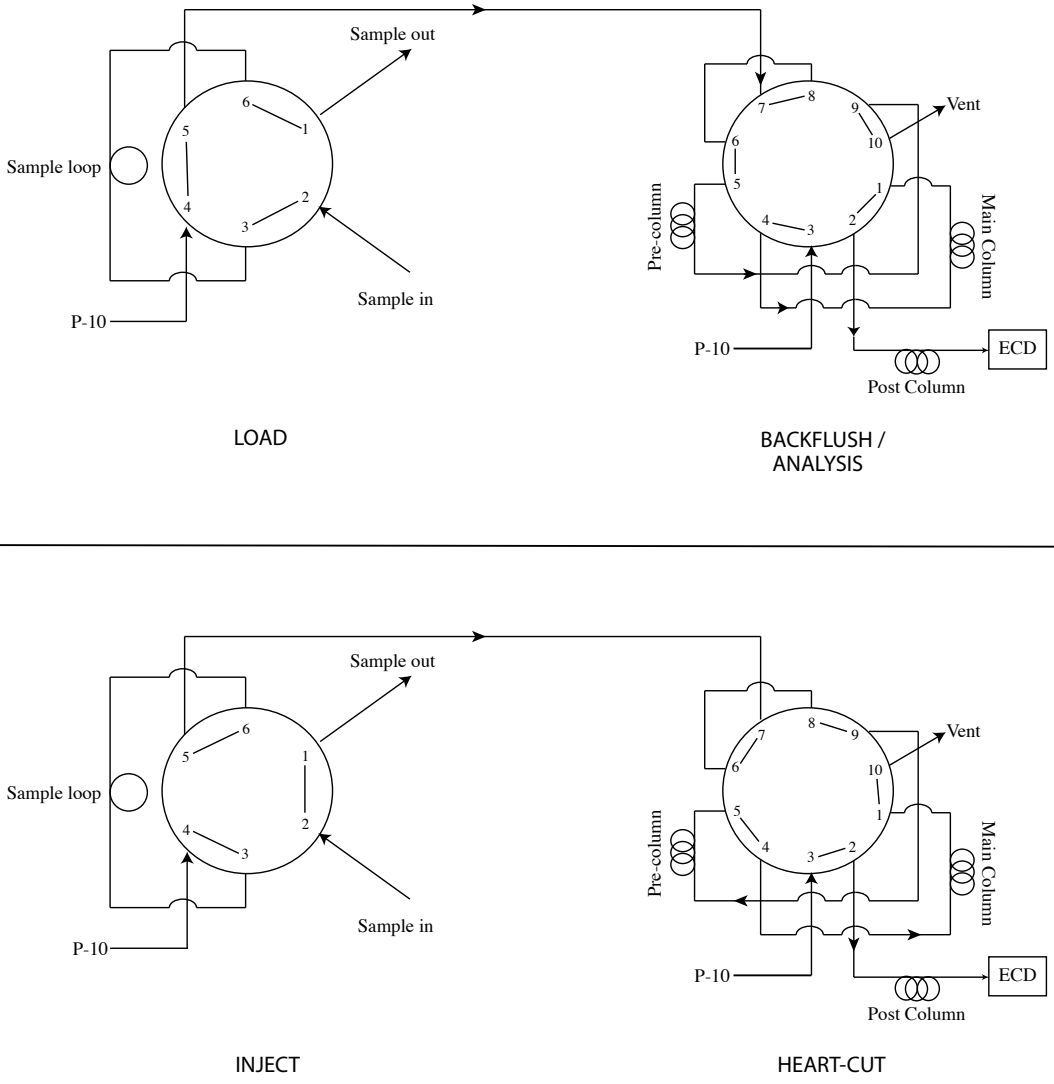

Figure 2-4: ECD valve configurations in the load/inject and backflush/heart-cut positions. During 'load' the sample loop is filled. The gas sampling valve then switches to 'inject', while the backflush valve is in 'heart-cut' to vent out O_2. After all O_2 has been removed, the backflush valve switches to 'backflush/analysis', where N_2O and SF_6 proceed to the main/post columns and the pre-column is back flushed.

Table 2.1: Summary of FID and ECD detector, sample loop and column parameters. Development of the methodology can be found in Hall et al. [2007, 2011], Dlugokencky et al. [2005] and Prinn et al. [2000]

	FID	ECD
Det. Temp.	190°C	340°C
Sample Vol.	1.5 mL	9 mL
Pre-column	HayeSep Q 100/120	Porapak Q 80/100
Length/ID/Temp	91cm/2.0mm/85°C	1.00m/3.7mm/85°C
Main-column	HayeSep Q 100/120	Porapak Q 80/100
Length/ID/Temp	1.82m/2.0mm/85°C	2.00m/3.7mm/85°C
Post-column	none	5Å Molecular Sieve 40/60
Length/ID/Temp		91cm/ 2.2mm/180°C

Table 2.2: Flow rates for FID and ECD components during each segment of the analysis.

Detector	Component	Flow rate (mL/min)
FID	Columns	40
	Backflush	40
	H_2 fuel gas	60
	Air fuel gas	275
ECD	Heart-cut	35
	Post-column	40
	Backflush	30

triggered so that devices are switched off during rare shut-down times.

Instrument operation and control is achieved through GCwerks® (version 3, Peter Salameh, http://gcwerks.com), a software designed for remote operation of GC instruments and for easy data integration and manipulation. GCwerks® is currently used at all AGAGE sites. The software has the ability to communicate with and control all components of the instrument and the uninterruptible power supply (UPS). Through GCwerks®, the 'run' sequence containing instrument parameters is auto-

Table 2.3: EPC head pressures to achieve desired flow rates. A 'red dot' restrictor is used on each EPC channel.

Detector	EPC	Valve configuration	EPC setpoint (psig)
FID	EPC5	Main	60
		Backflush	60
ECD	EPC3	Heart-cut	40
	EPC4	Heart-cut	45
	EPC3	Backflush/analysis	45
	EPC4	Backflush/analysis	60

matically implemented and set to alternate between an air sample and a standard to produce calibrated measurements. Furthermore, the software automatically corrects for the non-linearity in the ECD, and calculates the calibrated mole fractions and daily repeatabilities based on bracketed standard runs for a variety of metrics (e.g. peak height, peak area, peak width, retention time). This is discussed further in Section 2.2.

All components of the instrument (GC, pure air generator, pumps, valves, computer, gas purifier) are connected to the main power (and to generator power) through the UPS. Except for the pure air generator, which runs specifically on 220V, 50Hz power, all other components run on native United States 120V but are operating at 50 Hz. Components were purchased for 120V for two reasons: (1) the GC was previously purchased in 2006 for another project and (2) because parts would be easily testable in the lab at MIT. The pure air generator was purchased for 220V power as it requires dedicated operation at 50Hz due to the specific timing sequence of the methane reactor and compressors. As such, the UPS additionally acts as a step-down transformer for all components except for the pure air generator. When main (or generator) power is out for more than one and a half hours, GCwerks® is configured to run the normal sequence on battery power before triggering a shutdown sequence that will cool all GC heated zones, set valves to a safe position (i.e. ensure that the se-

lector is not bleeding standard gas), turn off the FID flame and cool down the heated gas purifier. The instrument is then in a safe position to be turned off (i.e. when batteries are depleted or the UPS is shut off). The time of normal operation on battery power can cover most outages but in the event that the instrument shuts down, there is sufficient battery time to cool the instrument down safely. Section 2.3 discusses mechanisms put in place to ensure the continuous operation of the instrument during power anomalies.

Data storage and backup is automated and done with three redundancies. The instrument computer continuously stores all chromatograms, stripcharts (temporal information about the run), and calibrated measurement values. The data is automatically copied to two additional locations at specified times every twelve hours. The data is copied onto an external hard drive that is connected directly to the computer and was used as a backup for times that the internet is down. The information is also copied to a machine at MIT and this machine is automatically backed up to a MIT server.

2.2 Characterization of Instrument

Figure 2-5 shows typical chromatograms for CH_4, N_2O and SF_6. In the FID chromatogram, oxygen elutes at 69 s followed by a larger CH_4 peak at 95 s. On the ECD system, there is no air peak as the oxygen is vented out prior to switching flow onto the post-column. The small disturbance in the baseline at $\sim$185 s is caused by a slight fluctuation in pressure during the valve-switch. This is followed by SF_6 at 329 s and N_2O at 423 s. The timing of the valve-switch was determined by varying this parameter and measuring whether there was an effect on the SF_6 and N_2O peak responses. When it was determined that increasing or decreasing this time by ten seconds had no effect on the peak response, it was deemed as a stable value, that is, no oxygen was being allowed to enter the detector and SF_6 and N_2O were not being cut off.

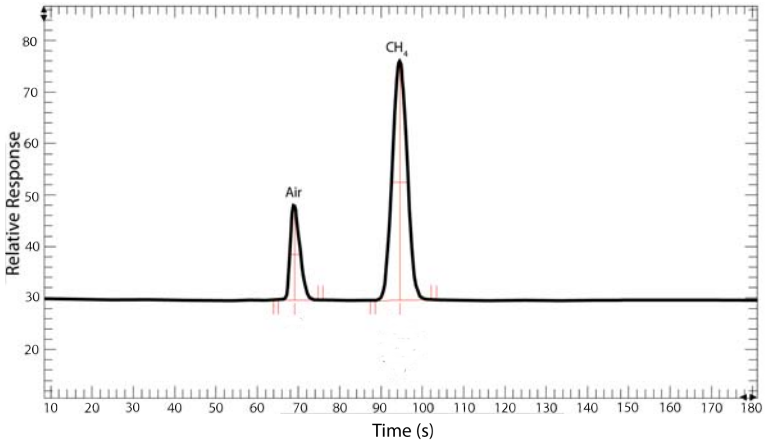

(a)

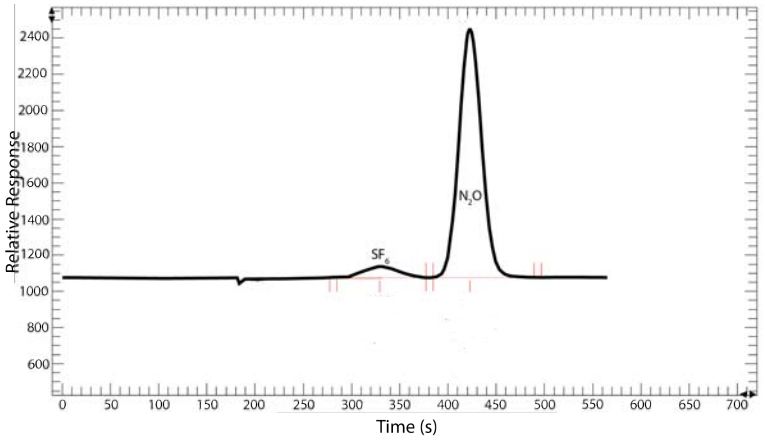

(b)

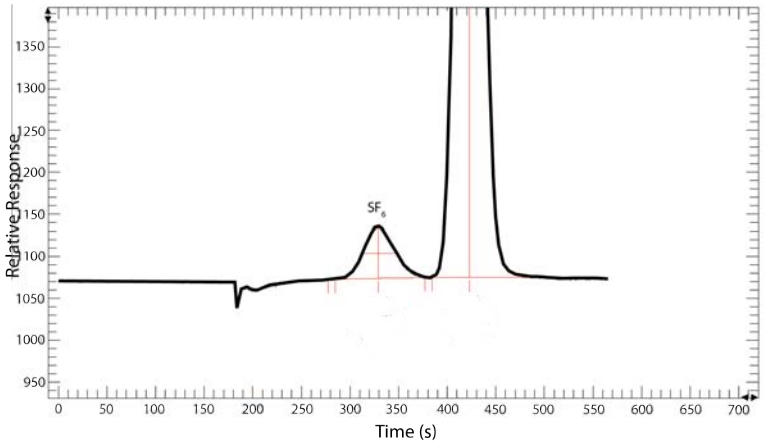

(c)

Figure 2-5: Typical chromatograms with units in relative response on the y-axis and time in seconds on the x-axis. (a) CH_4 elutes as a narrow peak at 95 s after a small air peak. (b) N_2O elutes at 422 s after oxygen is vented out and SF_6 elutes from the molecular sieve column. (c) SF_6 elutes at 329 s, prior to the much larger N_2O peak.

2.2.1 Repeatability

Repeatability is a key metric for establishing uncertainty on measurements, as well as for understanding the smallest resolvable signals in the mole fractions. The repeatability for the three gases is continuously monitored by GCwerks® which computes a 1σ 'daily' value on the standards measured each day. Typical 1σ values achieved using similar instrumentation at AGAGE sites (note: SF_6 is measured in AGAGE using the 'Medusa' GC-MS system which pre concentrates 2L of air and in this work, is measured using an ECD with a 9 mL loop injection) are 0.05-0.15%, 0.03-0.15% and 0.2-0.6% for CH_4, N_2O and SF_6, respectively. On this system, average 1σ values are 0.073% (CH_4 by height), 0.054% (N_2O by area), and 0.399%,(SF_6 by height) which lie within the range typically achieved for these gases (Figure 2-6). The average CH_4 repeatability was affected by two short periods (corresponding to daily values over 0.1 nmol mol^{-1}) when the H_2 pressure in the cylinder was below 200 psig. It is thought that small leaks caused by imperfections in the cylinder threads could have affected the CH_4 repeatability during these times. When the H_2 cylinders were replaced, daily values returned to normal. N_2O repeatability that is calculated by height is almost twice as large as that calculated by area and is due to the fact that a height fit correction has not been implemented on the N_2O peak, which has noise at the top of the peak (whereas noise is minimal in CH_4 and SF_6). Small deviations in where the top of the peak is found results in poor height repeatability. For CH_4 and SF_6, height and area repeatability are similar but calculations based on peak height will be used in the remainder of this study.

2.2.2 Memory and Non-Linearities

Memory effects were also investigated. Samples of ambient air were run in between samples of zero air to determine whether CH_4, N_2O or SF_6 would be measured in the subsequent zero air runs. For CH_4 and SF_6 there is no measurable memory effect. A non-linear 'memory' effect exists for N_2O and results from the doping of N_2O by carbon dioxide (CO_2) but this effect is eliminated after ten consecutive, automated

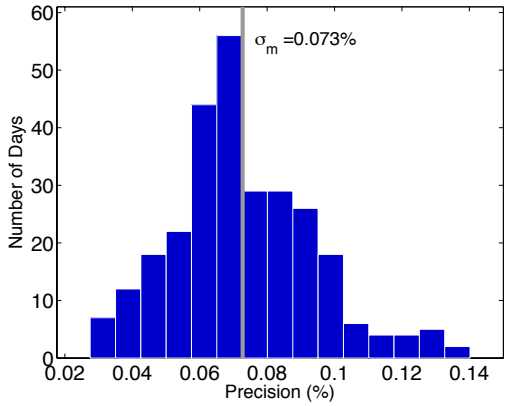

(a)

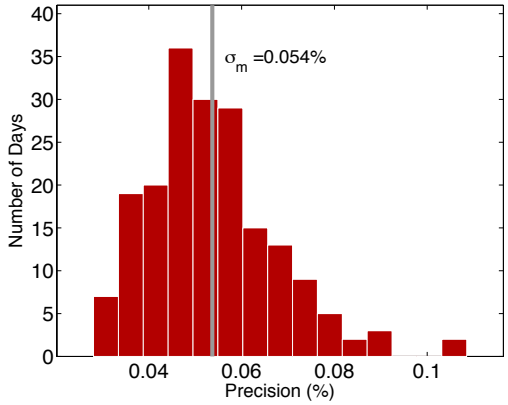

(b)

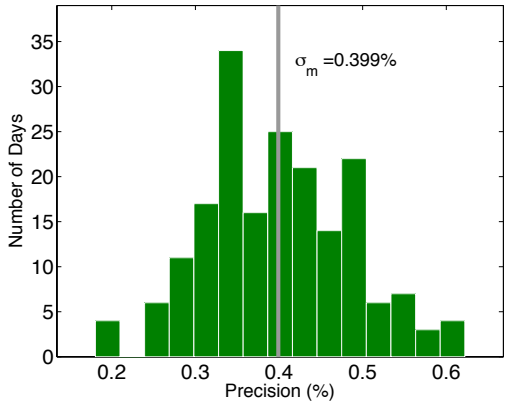

(c)

Figure 2-6: Histogram of instrument repeatability using the 1σ values computed daily for (a) CH_4 by peak height (b) N_2O by peak area and (c) SF_6 by peak height. Mean values for the entire time period is shown as a gray line.

injections of air (or standard filled with air) every ten minutes. This effect results from the fact that N_2O intrinsically has low sensitivity on an ECD due to a series of rapid reactions that both produce an electron and recapture an electron, leading to no net change in current (Equation 2.1) [Moore et al., 2003].

$$\begin{aligned} N_2O + e^- &\rightarrow O^- + N_2 \\ N_2O + O^- &\rightarrow NO^- + NO \\ N_2 + NO^- &\rightarrow NO + N_2 + e^- \end{aligned} \tag{2.1}$$

For this reason, the carrier gas contains 10% CH_4 which serves to interrupt the regeneration of the electron and thus leads to a decrease in current . However, CO_2 is also a dopant for N_2O and similarly interrupts the rapid recycling of the electron (Equation 2.2).

$$\begin{aligned} CH_4 + O^- &\rightarrow CH_3 + OH^- \\ CO_2 + O^- + N_2 &\rightarrow CO_3^- + N_2 \end{aligned} \tag{2.2}$$

In the current chromatographic setup, CO_2 co-elutes with N_2O (this must be done in order to measure SF_6 before N_2O) and an issue arises because variations in atmospheric CO_2 abundance could result in an artificial change in N_2O response. Furthermore, the molecular sieve column, which serves to reverse the order of N_2O and SF_6 elution, highly retains CO_2. At the temperature that the column is held (180°C), CO_2 from a sample slowly bleeds off the column for about two hours. This property is exploited because ten automated injections accumulates enough CO_2 in the system to prevent small changes from run to run to affect N_2O response. The time to 'equilibration' was tested by sampling from a tank of air for a given number of runs and then injecting either a sample of zero air (no CO_2) or a 1000 μmol/mol (high concentration) CO_2 sample and re-sampling the tank of air. The number of runs was varied until no change (i.e. within instrumental repeatability) was noticed before and after the variable CO_2 sample was injected. Any time the instrument is switched off or sampling has been interrupted, the first four hours (as a high overestimate) of data is thrown out.

Nonlinearities in the detectors were measured by exploiting the assumption that the FID is essentially linear over the range of concentrations of CH_4 that are being measured in the atmosphere. Beginning with this assumption, the non-linearity of

the ECD was determined from seven samples containing CH_4, N_2O, SF_6 in zero air and were made for the range of mole fractions measured at polluted AGAGE sites. The initial mixture was purchased from Linde LLC and the initial stock was made at 1200 μmol mol^{-1} CH_4, 175 μmol mol^{-1} N_2O and 5 nmol mol^{-1} SF_6 (balance zero air), concentrations that are roughly 670 times atmospheric concentration. At this concentration, the blend tolerance is $\pm$2% for CH_4 and N_2O and $\pm$5% for SF_6. A set of six samples were made from this initial stock that ranged from 1.8-5.8 μmol mol^{-1} CH_4, 277-1080 nmol mol^{-1} N_2O and 7.5-38 pmol mol^{-1} SF_6 (a seventh sample was made for SF_6 to increase the range as the contrast in values measured in 'pollution events' at other AGAGE sites versus background air is much larger for SF_6 than for CH_4 or N_2O). The dilution ratio for each sample was determined from the CH_4 response for each sample and by assuming that the FID is linear.

Four of the set of the linearity samples were prepared in new 3L stainless steel cylindrical cylinders with electropolished interiors and dual-inlets from Lab Commerce, Inc. Two samples were prepared in older 2.9L round-bottom stainless steel flanks with single inlet from Biospherics Research Corporation. In preparation, the cylinder and flasks were first filled with ultra high purity N_2 and evacuated to below 100 mtorr a total of three times using an Edwards High Vacuum Pump. This N_2 was first sampled directly from the cylinder on the FID and ECD for any trace amounts of CH_4, N_2O or SF_6 and there was no detectable amount of these gases. Next, all of the sample flasks and cylinder were filled with this N_2, allowed to sit for several days and then re-measured for CH_4, N_2O and SF_6 content. One of the older round-bottom flasks was found to have elevated N_2O and this flask was replaced. All other flasks and the cylinder showed no detectable amount of CH_4, N_2O or SF_6 and it was concluded that there was no outgassing of these compounds from the flask itself. The third step was to test the ultra zero air that would be used for dilution for any trace amounts of these compounds. After evacuation of the N_2, the cylinder and flasks were filled with the zero air and again measured for CH_4, N_2O and SF_6. There was no detectable amount of CH_4, N_2O or SF_6 in the zero air and it was concluded that traps would not be necessary for purification. The initial stock was first diluted into

secondary and tertiary mixtures, which wet prepared in a 34L stainless steel cylinder (Essex Cryogenics). The cylinder was evacuated, filled with stock and allowed to equilibrate to atmospheric pressure. The cylinder was then filled with ∼200 psig of zero air and allowed to mix to form the secondary sample. After mixing, the cylinder was re-equilibrated to atmospheric pressure (venting out most of the secondary) and refilled with ∼200 psig of zero air. This tertiary sample was used for subsequent dilutions. Samples were diluted from the tertiary (except for sample X which was made in a separate series to extend the range for SF_6) by filling the flask with ∼5 psig of the parent, allowing the flask to equilibrate to atmospheric pressure (so that approximately same amount of parent is used in each dilution), followed by addition of varying amounts of zero air. This procedure was followed, rather than creating a dynamic dilution series, because a mass flow controller was not available for use. Use of the mass flow controller would have allowed dilution to be measured without use of the FID to diagnose dilution ratio, but is not expected to yield different results. CO_2 was not present in any samples and small non-linearities could be introduced in ambient samples as the detector could be closer to saturation.

Non-linearity analyses are plotted as the unitless 'normalized sensitivity' versus 'normalized peak response' in Figure 2-7. Peak response, by either height or area depending on the substance, is analogous to the mole fraction of the sample. Sensitivity is the 'response per mole' given the known concentrations of the samples. Both of these are normalized to a common standard (sample D with roughly atmospheric concentrations) so that any drift that occurs over the time that the measurements are being made is corrected for by the standard. Therefore, an instrument that is linear would have normalized sensitivities of unity over all concentrations, as the 'response per mole' would remain constant. In this case, CH_4 is prescribed to be linear and so values of unity at all concentrations is assumed.

Nonlinearities could change over time and should periodically reevaluated. Nonlinearities could be affected by changes in carrier gas (though this effect would be small), changes in columns or changes in the detectors. Nonlinearities based on the small range in mole fractions measured at Darjeeling are considered to be small. For

Table 2.4: Samples made for linearity analysis. The tertiary was used to create samples A-E. Sample X was created in a separate series to extend the range. Dilution ratios were determined by measuring CH_4 response and assuming linearity in the FID.

Sample	Cylinder	Species	Mole fraction (nmol mol^{-1})
Tertiary	34L stainless	CH_4 N_2O SF_6	5056.4 738.1 20.9x10^{-3}
A	3L cylindrical, dual-inlet	CH_4 N_2O SF_6	3232.5 471.8 13.4x10^{-3}
B	3L cylindrical, dual-inlet	CH_4 N_2O SF_6	2556.0 373.1 10.6x10^{-3}
C	3L cylindrical, dual-inlet	CH_4 N_2O SF_6	2257.4 329.5 9.3x10^{-3}
D	3L cylindrical, dual-inlet	CH_4 N_2O SF_6	1911.2 279.0 7.9x10^{-3}
E	2.9L round	CH_4 N_2O SF_6	1721.4 251.2 7.1x10^{-3}
X	2.9L round	CH_4 N_2O SF_6	9183.9 1339.3 38.3x10^{-3}

N_2O, the range of concentrations measured in Darjeeling in 2012 is 325-331 nmol mol^{-1} for N_2O and 7.4-8.2 pmol mol^{-1} for SF_6 (Chapter 4).

2.2.3 Calibration

Measurements are calibrated using a dry compressed air standard filled in an electropolished aluminum cylinder (30 L water capacity, 1700 psig fill pressure) at the Scripps Institution of Oceanography (SIO) in July 2012. The cylinder was first passivated with air for approximately a week and then evacuated and re-filled. The standard was calibrated to values of 1835.01± 1.16 nmol/mol, 324.60 ± 0.09 nmol/mol, and 7.55 ± 0.04 pmol/mol for CH_4, N_2O and SF_6, respectively, using the AGAGE Multi-Detector system (for CH_4 and N_2O) and the AGAGE Medusa system (for SF_6). CH_4, N_2O and SF_6 are calibrated on the Tohoku University, SIO-98 and SIO-2005 scales, respectively. Intercalibration between different scales (e.g., SIO, Tohoku, NOAA) are routinely performed and result in an offset between measurements calibrated on different scales [Prinn et al., 2000, Cunnold et al., 2002, Huang et al., 2008, Rigby et al., 2010].

Ambient air measurements can be calibrated either by peak height or peak area, depending on instrument performance. Equation 2.3 shows the calibration procedure, where r_{air} and r_{std} are the response for air and standard, respectively. Each air measurement is bracketed by standards, that is, the response of the standard is interpolated in time using the standard response on either side of the air measurement (indicated by the overbar).

$$\chi_{sample} = \frac{r_{air}}{\overline{r_{std}}} \chi_{standard} \tag{2.3}$$

Due to the high fill pressure and large volume of the cylinder, enough air is available in the standard to run the instrument for three years. Studies have shown that dry standards filled in electropolished aluminum cylinders have been used widely and no significant drift has been reported for each of the three gases over the timeframe

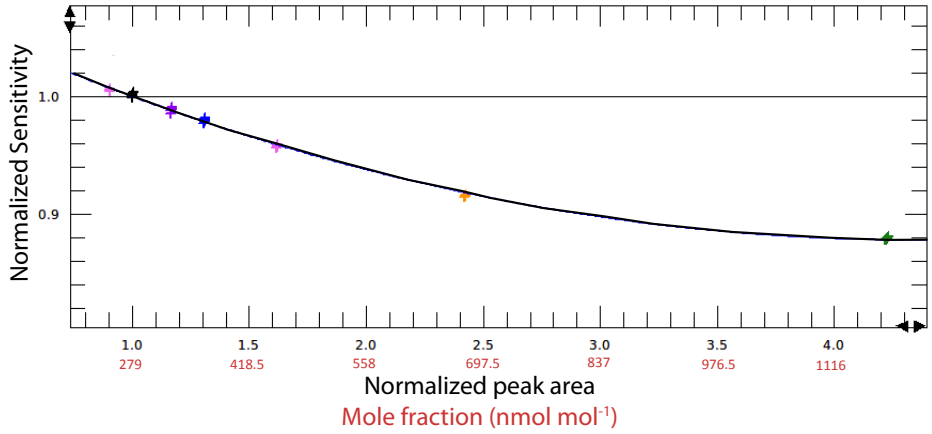

(a)

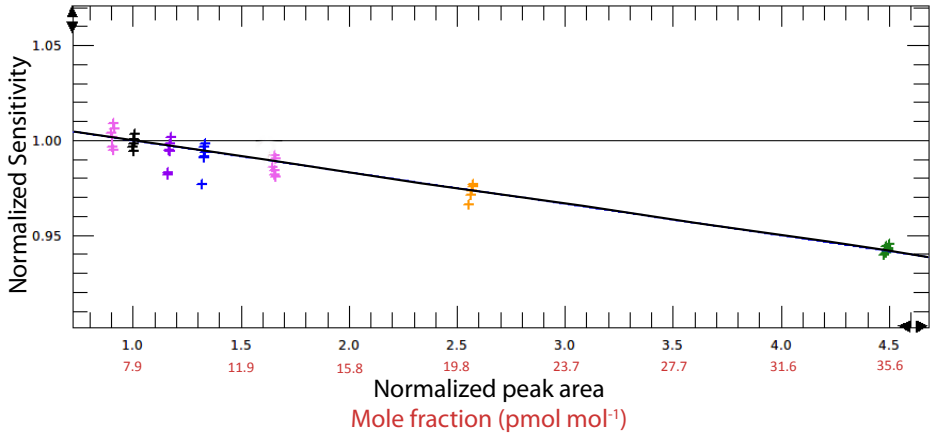

(b)

Figure 2-7: Non-linearity analysis, showing normalized sensitivity on the y-axis and normalized peak response (height or area) of the instrument on the x-axis. (a) N_2O (b) SF_6

of this study [Dlugokencky et al., 2005, Hall et al., 2007, 2011]. To verify standard drift, the ratios of the standard and two other cylinders should be computed yearly to compute 'drift values,' A, B and C in Equation 2.4. This test was scheduled for January 2013 but due to a cancelled site visit, has been postponed to summer 2013. In the absence of this analysis, there is no suitable alternate metric to evaluate standard drift. Raw responses in the standard cannot be used as there is considerable instrumental drift, which varies differently for different species. A comparison of drift in the raw standard responses will give erroneous results.

$$\begin{aligned} \frac{\chi_{standard} + A}{\chi_{cylinder,1} + B} &= R_1 \\ \frac{\chi_{standard} + A}{\chi_{cylinder,2} + C} &= R_2 \\ \frac{\chi_{cylinder,1} + B}{\chi_{cylinder,2} + C} &= R_3 \end{aligned} \tag{2.4}$$

2.3 Implementation at Site

The largest source of instrument instability is due to the fluctuating power. It is not uncommon to see several short duration (i.e., less than 1 hour) power outages per day. Furthermore, the voltage can drop below 180V during peak consumption hours (6-9 am, 7-10 pm). The isolation transformer, UPS and generator make it generally possible to operate without interruption and is further discussed.

At the time of installation of the FID (November 2011), the line to the GC included a manual isolation transformer with voltage stabilizer to stabilize the line voltage at 220V and an auto-mode 30 kVA generator. However, this setup made it necessary for manual switching between the mains and generator, which due to human error, has led to inadvertent shut-down of the instrument. Additionally, during periods of increased load, the transformer was not able to cope with the demand and failed to stabilize the voltage, again leading to a shut-down of the instrument. The main modifications

made to the pre-existing site is that a new auto-mode 30 kVA, three-phase isolation transformer with built-in servo voltage stabilizer was installed on the line (May 2012) to this instrument. The addition of a second isolation transformer reduced the total load on each and allowed for dedicated lines to the instruments that are separated from general-use power lines. As with the original isolation transformer, the purpose of this device is to both electrically isolate the devices from the source, thus preventing damage from surges, as well as to stabilize the voltage during brown-outs. The new auto-mode feature removed the influence of human error that had previously resulted in shut-downs by including automated switching between the mains and the generator lines. After installation of this isolation transformer, data losses were much less frequent.

The inlet line was installed approximately 5m high on a 10m tower that is constructed on the roof of a four-story building (Figure 2-8a,b,c). At this height, it is possible to have local influence from the building on air flow but constructing a taller tower was not feasible. The inlet cup was inverted and attached via hose clamps to a 1-inch vertical aluminum rod which was affixed to a 3m rod extending horizontally from the tower. A 1/4" guy wire was extended across the two buildings and clamped down using wire rope clamps. The Synflex tubing was affixed with hose clamps and zip ties approximately every meter to a tie-down point on the tower, along the guy wire and on rebars mounted along the sides of the buildings. There is no point where excessive stress is placed on the Synflex. The inlet line is connected directly to the pump module and totals ~65 feet in length. The instrument is located on the first floor of an adjacent building equipped with an air conditioner and de-humdifier (Figure 2-8d). The dehumidifier is used continuously between March-October and the air conditioner is only used for hot days during the summer, when air temperatures exceed 27°C. Most of the year, air temperatures are significantly below this threshold and the air conditioner is not needed. A small fan is used instead to ventilate air in the lab. The inlet line that is within the lab space has been insulated with pipe insulation to minimize the formation of condensation in the line when the air conditioner is being used.

(a)

(b)

(c)

(d)

Figure 2-8: (a) Sampling tower, mounted on the roof of a 4-story building. (b) Installation of the inlet line on the tower (c) Sampling tower with mounted inlet line and position of guy wire connecting to adjacent building. (d) Laboratory housing the equipment.

Chapter 3

Chemical Transport Modeling

3.1 Lagrangian Particle Dispersion Model

3.1.1 Model Formulation

The UK Met Office's Numerical Atmospheric dispersion Modeling Environment version 3 (NAME) is a Lagrangian Particle Dispersion Model (LPDM) used to simulate atmospheric transport [Jones et al., 2004, Ryall and Maryon, 1998]. In this application, NAME calculates transport by following a large number of particles 'backwards' in time from the measurement site. The particles move in large part with the wind, which is provided by three-dimensional meteorological fields supplied from a Numerical Weather Prediction (NWP) model but also from additional turbulent motion that is simulated by a random-walk formulation. Chemistry, wet and dry deposition and radioactive decay can be included but for the purposes of the long-lived gases being studied here, particles are assumed to be inert.

Particles are advected each timestep via Equation 3.1, where $\boldsymbol{x_t}$ and $\boldsymbol{u}(\boldsymbol{x_t})$ are the particle position and velocity at time t. $\boldsymbol{u'}(\boldsymbol{x_t})$ and $\boldsymbol{u'_l}(\boldsymbol{x_t})$ are the components of particle motion due to turbulence and low-frequency meander. The low-frequency meandering term acts on scales between those resolved by the meteorological fields and those paramaterized by turbulent motion.

$$\boldsymbol{x_{t+\Delta t}} = \boldsymbol{x_t} + [\boldsymbol{u}(\boldsymbol{x_t}) + \boldsymbol{u'}(\boldsymbol{x_t}) + \boldsymbol{u'_l}(\boldsymbol{x_t})]\Delta t \tag{3.1}$$

Both turbulence and meander are calculated as random-walk motions with profiles that were determined as fits to observational data [Morrison and Webster, 2005]. The random-walk formulation is shown in Equations 3.2 and 3.3, where σ_u^2 and σ_w^2 and τ_u and τ_w are horizontal and vertical velocity variances and Lagrangian timescales, respectively and r_t is a random value with zero mean and unit variance. σ_u and σ_w are both computed based on turbulence profiles for stable and unstable (e.g. convective) conditions and converge to free tropospheric values of 0.25 m/s and 0.1 m/s, respectively. For both stable and unstable conditions, homogenous ($\frac{\partial \sigma_w}{\partial z} = 0$) and inhomogeneous profiles are available, the latter being more computationally expensive. The first right-hand terms of Equations 3.2 and 3.3 correspond to 'memory' of the previous step and the second term to a random perturbation. In all of the runs used in this study, the memory term is neglected for computational efficiency. The third term of Equation 3.3 corresponds to a 'drift velocity,' which prevents particles from accumulating when σ_w is low. This term is required in the vertical since σ_w can change dramatically with height, while changes are small in the horizontal. In the model runs used here, a homogeneous approximation is assumed and this term is therefore zero. An entrainment scheme deals with a turbulence discontinuity at the top of the boundary layer in the homogeneous scheme.

$$\boldsymbol{u'_{t+\Delta t}} = \boldsymbol{u'_t}\left(1 - \frac{\Delta t}{\tau_u}\right) + \left(\frac{2\sigma_u^2 \Delta t}{\tau_u}\right)^{1/2} r_t \tag{3.2}$$

$$\boldsymbol{w'_{t+\Delta t}} = \boldsymbol{w'_t}\left(1 - \frac{\Delta t}{\tau_w}\right) + \left(\frac{2\sigma_w^2 \Delta t}{\tau_w}\right)^{1/2} r_t + \frac{\Delta t}{\sigma_w}\frac{\partial \sigma_w}{\partial z}(\sigma_w^2 + w_t'^2) \tag{3.3}$$

A simple convection scheme is utilized. In convective clouds deeper than 500m, a fraction of particles (based on cloud fraction) are randomly redistributed from the cloud base to cloud top.

Though particles are treated as inert species, CH_4 oxidation by OH is the most

significant loss process for the species modeled and this loss is considered to be small on the 30-day timescale of the air history. As discussed in Manning et al. [2011], the typical depletion in CH_4 during this time would be on the order of a couple of percent, but this error is expected to be much smaller than other uncertainties. The convection scheme could be a leading source of error, particularly for the deep convection that occurs during the Indian monsoon. Errors in the boundary layer formulation could also lead to significant errors in the derived air history maps. This uncertainty is expected to be more significant at night when boundary layer height is low. Finally, errors resulting from topography in the Himalayas could contribute to uncertainties in the large-scale transport and will be discussed further.

3.1.2 Model Setup

The computational domain used for the model runs over Darjeeling is from 5-50°N, 50-120°E, covering India, China, Southeast Asia, part of the Middle East and up to 19 km vertically. This domain was chosen to be consistent with the methodology used in the inverse modeling and will be discussed further in Chapter 5.

Particles are released from the Darjeeling station (27°02'N, 88°15'E) at a release height between 450-550 magl and are released randomly throughout this 100 m column in order to minimize errors that occur at any given height. The choice of this release height is discussed in Section 3.3. Particles are released continuously at a rate of 20000 particles hr^{-1} at a mass of 1 g s^{-1} for each three hour period. The choice of particle release rate is important to ensure a good statistical distribution of particle trajectories and depends on the model and output resolutions.

3.1.3 Model Meteorology

NWP meteorological fields from the Met Office's Unified Model (UM) were used to drive NAME. Most model simulations utilized the UM South Asian Model (SAM), which is available from 2010 onwards for the South Asian domain at 0.11° horizontal resolution and for 70 vertical levels at three-hourly temporal resolution. A compar-

ison with lower resolution meteorology using the UM global model at 0.352°x0.234° horizontal resolution, for 70 vertical levels and three-hourly resolution was made to investigate the role of meteorological resolution in modeling flow in the Himalayas and will be discussed in Section 3.2. The model time step in all simulations using SAM was five minutes.

For computational efficiency, SAM fields are nested within the global meteorological fields. Nesting is done 'temporally,' with SAM fields used for the first seven days backwards in time, followed by utilization of the global model fields at lower resolution. It is assumed that within seven days (as an overestimate), particles will have left the Himalayas and the lower resolution drivers would be sufficient to model flow through the plains, as meteorological fields from the global model are considered to be sufficient to model the overall synoptic flow. Furthermore, if particles leave the computational domain of SAM prior to the seven day period, they enter the flow regime of the global model. Small discontinuities could exist at the boundaries between the different meteorologies.

Figure 3-1 shows the difference in topography in the two models and it is clear that the higher resolution model captures more topographical features in the Himalayas that are otherwise smoothed in the global model. While the true surface height of the observation point is 2194 masl, the model surface height in the SAM and global model topography files are 1340 and 1129 masl, respectively.

Boundary layer height is computed within the NWP model and is used to drive the turbulence profiles discussed above. NAME was set to have a minimum and maximum boundary layer height of 100 m and 4 km, respectively. Uncertainties associated with boundary layer formulation in the NWP model are not investigated in this study, but could have a significant impact on the derived air histories.

3.1.4 Air Histories

NAME outputs 'air histories' or the influence of surface emissions on the measured concentrations at the station and directly provides the sensitivity of a measurement in Darjeeling to emissions from the domain. Output resolution is at the same resolution

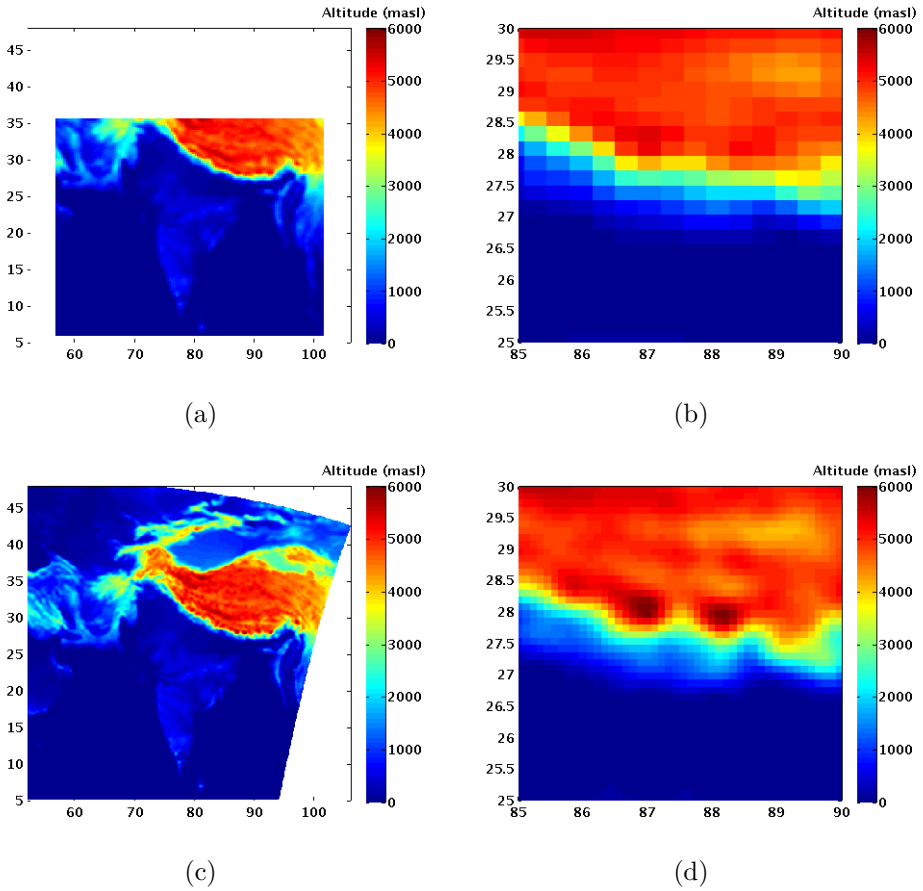

Figure 3-1: Topography for South Asia (left hand side) and Darjeeling region (right hand side) used by NAME and the Unified Model at (a,b) global model resolution at 0.352°x0.234° and (c,d) SAM resolution at 0.11°x0.11°. Colorbar shows altitude in masl.

as the global model meteorological fields and is at 0.352°x0.234° horizontal spacing. In the vertical, a 0-100 magl level is used. The horizontal resolution was chosen rather than the resolution of the SAM fields for two reasons: (1) because after the seven day period, this is the maximum resolution modeled and (2) for computation efficiency since the model time step was decreased by a factor of three (over runs using just global meteorology) to accommodate the high resolution of SAM. The temporal resolution of the output is three hourly, again, to be consistent with the meteorological resolution. Particles mass and the corresponding amount of time that particles spend in the lower 100 meters above ground of the model are tracked throughout a 30-day period and result in an integrated value over this period. The time period was chosen

to ensure that the majority of particles have left the domain within this time to result in a complete 'picture'. If particles do not leave the domain, then the influence of surface emissions from the domain could be underestimated. The output is the time-integrated surface influence (g s m^{-3}) for each grid cell resulting from a release of particles at 1 g s^{-1} from the site. The surface influence is divided by the total mass emitted during each three hour period and multiplied by area of each grid cell to form the matrix, **D**, which represents how 1 g m^{-2} s^{-1} of continuous emissions from the site would result in the measured concentration at the receptor. Multiplying **D** by an emissions field (**E**) would result in the 'contribution' by each grid cell to concentration at the receptor (**C**) (Equation 3.4). To convert from concentration (g m^{-3}) to mole fraction (mol mol^{-1}), concentrations are scaled by temperature (K) and pressure (Pa) at the receptor for each measurement time (using meteorological fields generated by the model), by the molar mass of the gas (g mol^{-1}) and the gas constant (J mol^{-1} K^{-1}) (Equation 3.5).

$$\mathbf{DE} = \mathbf{C} \tag{3.4}$$

$$\chi_i = c_i \frac{\mathrm{R}T_i}{p_i \mathrm{M}} \qquad \text{for i=1...m} \tag{3.5}$$

NAME has been used extensively for similar applications and at various sites, including Mace Head, Ireland, and the high-altitude station of Jungfraujoch, Switzerland [Manning et al., 2011, 2003, O'Doherty et al., 2004, Reimann et al., 2005]. Other LPDMs could have been used (e.g. FLEXPART, Stohl et al. [2009]) and uncertainties associated with the choice of model have not been quantified.

Figure 3-2 shows example air history maps derived for a measurement in January and July. The January air histories show surface influence from both the east and west of the station, indicating that air from both sides of the site are sampled. This is discussed further in Section 3.4. During the winter, air from Northern India is sampled with high sensitivity and in contrast, summer air histories show dominant sensitivity in the southwesterly direction, which arises from the strong monsoonal flow.

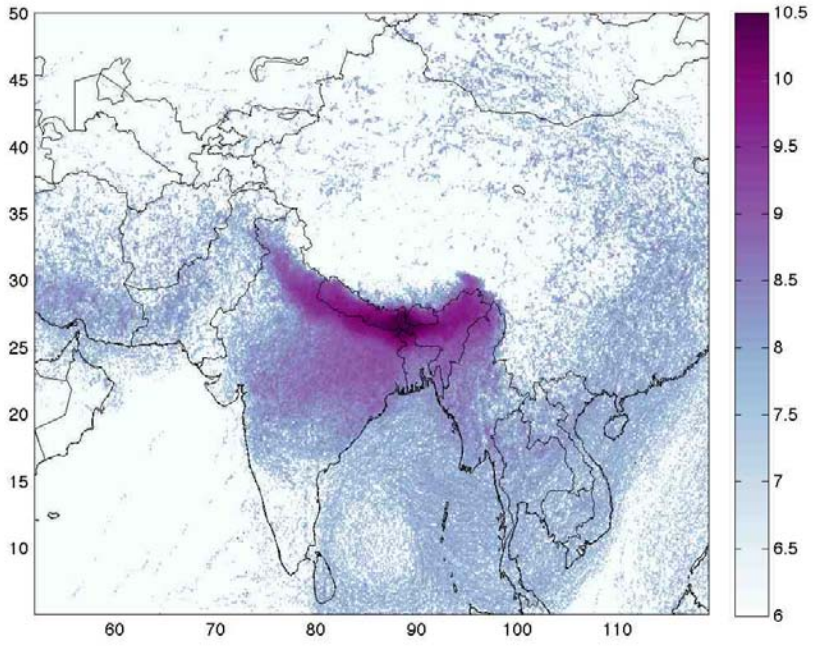

(a)

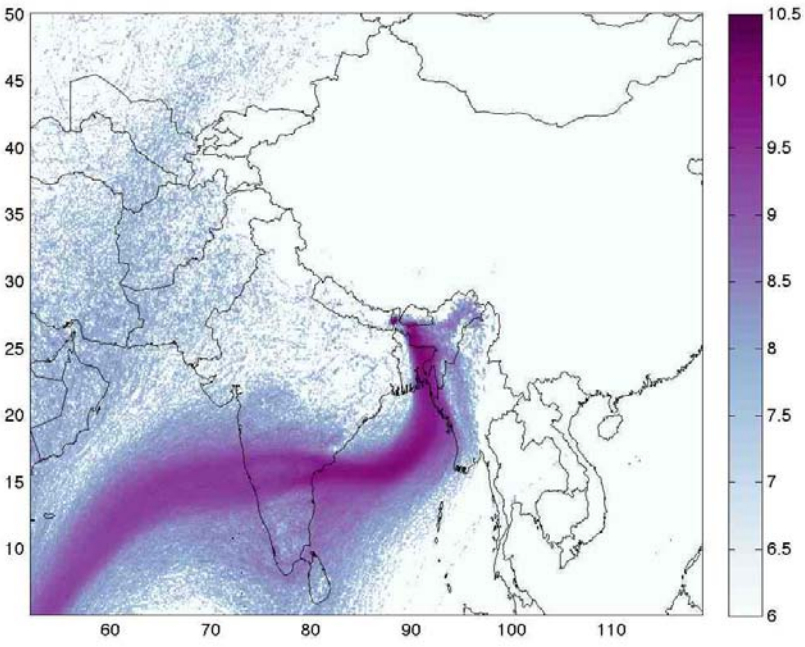

(b)

Figure 3-2: Air history maps derived for a measurement in (a) January 2012 (b) July 2012. Colorbar units are in $\log_{10}$((pmol/mol) / (kg m^{-2} s^{-1})) and indicate the contribution of 1 kg m^{-2} s^{-1} of emissions from each grid cell to mole fractions of any inert gas at Darjeeling.

3.2 Effect of Meteorological Resolution

The effect of meteorological resolution in the derived air history maps is investigated. Air history maps derived using the UM model at different resolutions are compared to a reference run, which consists of running the high-resolution SAM meteorology backwards for 7 days and running the global model for the remainder of the run (this nesting approach is described in Section 3.1.3). Two cases are compared to the reference: (1) exclusively running NAME with the global model meteorology and (2) running NAME for 3-days back from release with SAM meteorology, followed by the global model meteorology.

Figure 3-3 shows the difference in the air history maps between the perturbed and reference runs. The difference between running SAM for 3-days and 7-days is small, with a maximum difference of ±10%. This suggests that particles have mostly left the Himalayas after 3 days into the flat plains region, where the effect of model resolution is small and where sensitivities are also smaller. When running NAME exclusively with the global model meteorology, differences are significant, with a ± 100% change in the surface influence in areas nearby the site. Changes in the air history maps are converted to a corresponding difference in simulated mole fraction at the site using an *a priori* emissions field (information about these emissions fields are found in Chapter 5). Simulated January mole fractions change up to 100 nmol mol^{-1}, 1.5 nmol mol^{-1} and 0.15 pmol mol^{-1} for CH_4, N_2O and SF_6, respectively, by using the global model meteorology, while very little change is present if SAM is used for 3-days or 7-days (Figure 3-4).

This comparison suggests that the effect of model resolution is critical in modeling mountain sites. This finding may even be important to sites that are flat but where nearby sources are large, as most of the difference in simulated mole fractions comes from the emissions of grid cells close to the site.

Wind speed and wind direction at 500 magl at Darjeeling during January 2012 are compared in the two meteorological models and are shown as wind roses during the day (12-4pm) and night (12-4am) in Figure 3-5. The two show similarity in

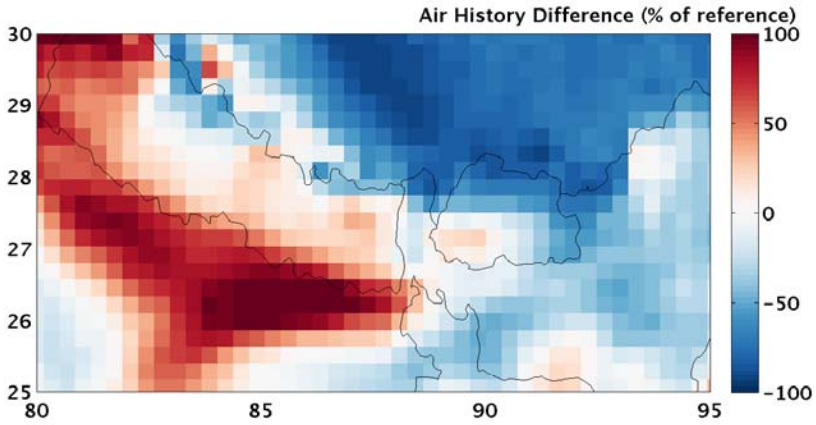

(a)

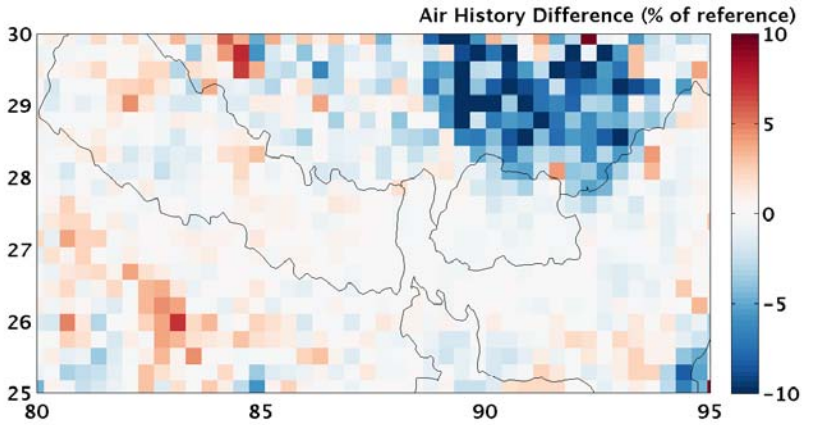

(b)

Figure 3-3: Average January percentage difference in surface influence of the reference run and (a) running with the global model meteorology and (b) running with SAM meteorology for 3-days backward, followed by the global meteorology.

overall wind speed and direction and both capture the diurnal cycle in wind direction, suggesting that the origin of this diurnal shift in wind direction is a feature that is larger than the global NWP model's ∼25 km scale. During the day, however, SAM has one predominant wind direction while the global model has greater variability and the opposite is seen at night. Though it appears that the differences in horizontal winds are small, they could contribute to variations in the simulated flow in the two models. In addition to horizontal wind speed and wind direction, vertical transport and convection will be resolved differently and could contribute significantly to the transport of particles to/from altitude from/to the surface. This transport is expected

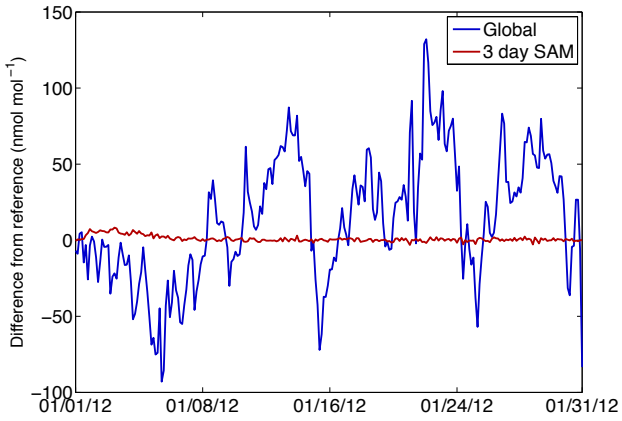

(a) CH_4

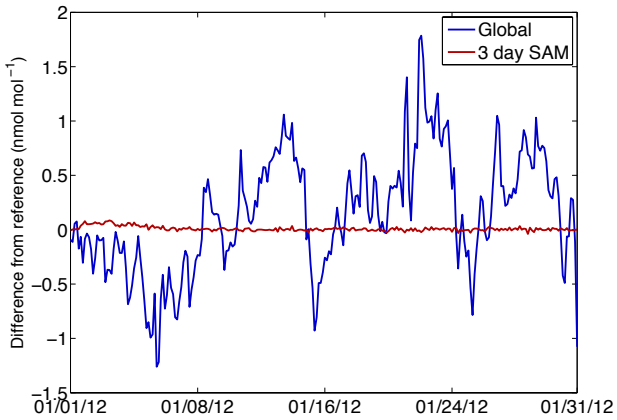

(b) N_2O

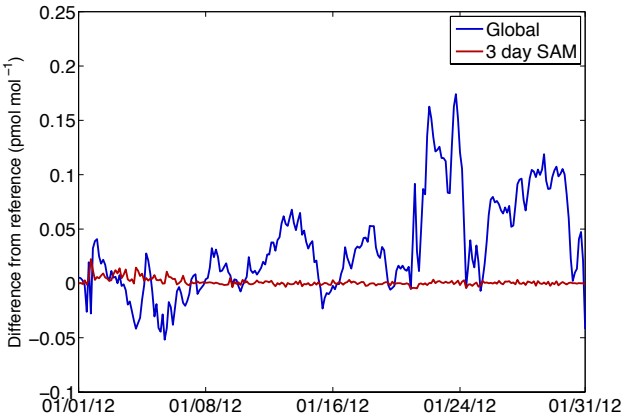

(c) SF_6

Figure 3-4: Effect of meteorological resolution on mole fractions simulated at Darjeeling for January. Figures are shown as a difference in mole fractions from using a perturbed resolution (global model meteorology, blue and 3-days SAM meteorology, red) and the reference resolution (7-days SAM) for (a) CH_4 (b) N_2O (c) SF_6.

to be important in the subtropics and particularly during the summer monsoon.

The effect of resolution on emissions estimation is investigated further in Chapter 5.

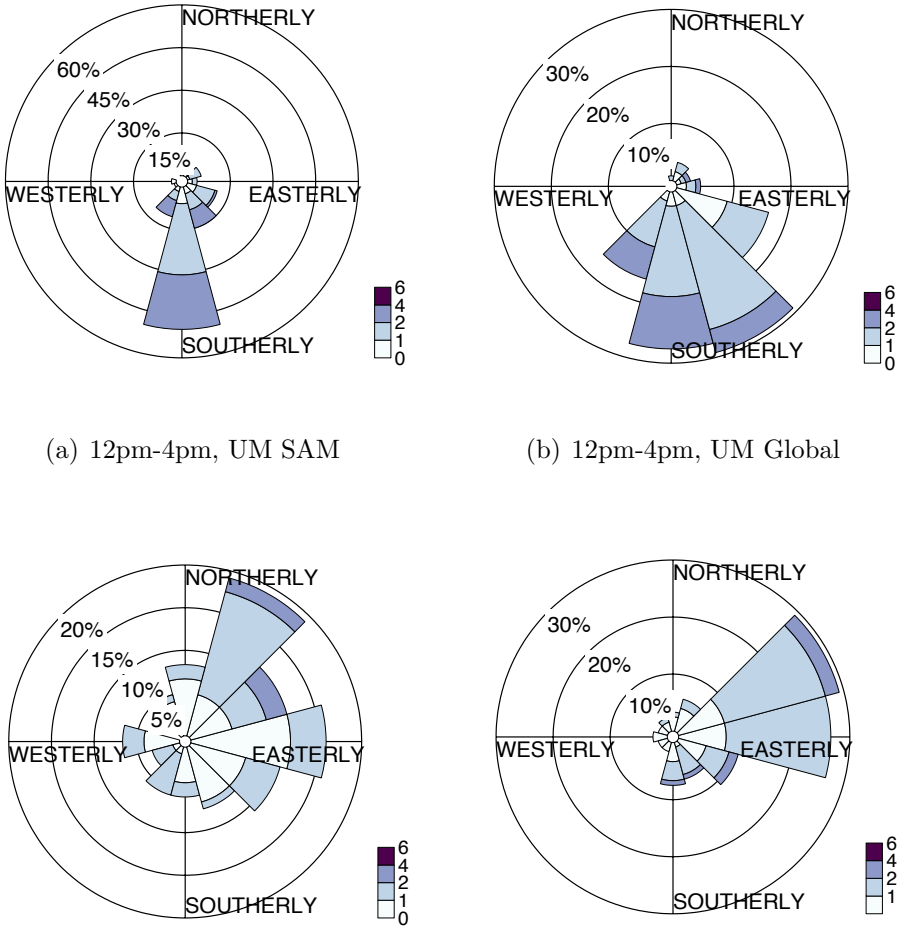

(a) 12pm-4pm, UM SAM

(b) 12pm-4pm, UM Global

(c) 12am-4am, UM SAM

(d) 12pm-4pm, UM Global

Figure 3-5: January wind roses at 500 magl, showing percentage of time with given wind direction and speed (colorbar, m/s) for (a) 12pm-4pm, SAM model (b) 12pm-4pm, global model (c) 12am-4am, SAM model (d) 12am-4am, global model

3.3 Effect of Particle Release Height

The particle release height for the model runs used in this study is 500 magl (with a 100 m release column) and was chosen as a compromise between the model surface height (1340 m) and the true surface (∼2220 m at sampling point). This height is a compromise between capturing surface flows at the model surface, and capturing the flows that would occur at the true altitude of the station. At mountain sites, this is generally an important parameter that strongly impacts resulting emissions inversions [Brunner et al., 2012, Tuzson et al., 2011]. A particle release height that is too high could underestimate the sensitivity of surface emissions at the site, while a release height that is too low could overestimate the sensitivity. Furthermore, the release height impacts the wind direction, speed and effect of friction at the release point, which could greatly alter the trajectories of particles as they leave the site. In previous studies, several methods have been used to determine the particle release height at mountain sites. In Brunner et al. [2012], air history maps were created for a range of release heights and the release height that best matched the observations (i.e. release height that gave the highest correlation between simulated and observed mole fractions) was used for emissions estimation. This was not done in this study at it was desired to have a more physical basis for choosing the release height. In another study, release height was determined by comparison of specific humidity at the mountain site with nearby vertical soundings [Tuzson et al., 2011]. However, this meteorological data was not available at Darjeeling.

Figures 3-6 and 3-7 show the effect of particle release height on the air histories derived in January and July. Three cases were investigated using release heights of 400 magl and 600 magl and compared to the reference release height (500 magl). In all cases, a 100 m column is assumed, centered on the release height. The largest change occurs in the region surrounding the site and results in up to a 50% difference when increasing or decreasing the release height by 100 m. The distribution of the percentage change between the 400 magl and 600 magl maps to the reference map is relatively symmetrical but with opposite sign.

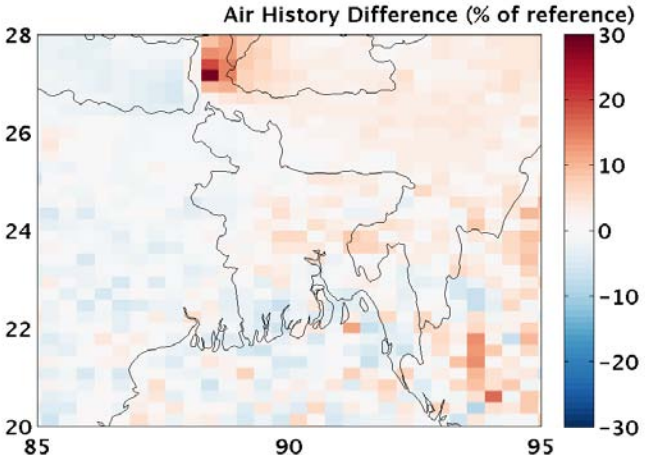

(a)

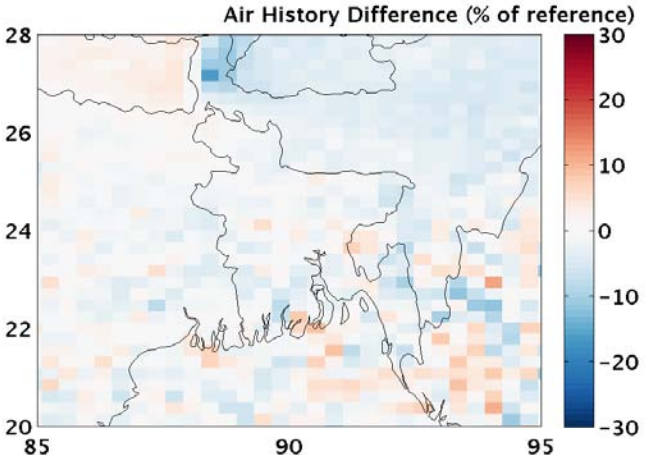

(b)

Figure 3-6: Average January percentage difference in surface influence from the reference (500 magl) particle release height for a (a) 400 magl release height and (b) 600 magl release height.

Using a constant emissions field (discussed in Chapter 5), the difference in mole fractions simulated at Darjeeling between different release heights and the reference case is shown in Figures 3-8 and 3-9. The difference in simulated mole fractions from a 100m change in particle release height can lead to up to a ± 60 nmol mol^{-1}, ± 0.4 nmol mol^{-1} and ± 0.03 pmol mol^{-1} difference in July CH_4, N_2O and SF_6 mole fractions, respectively. A smaller effect is seen in January mole fractions when convection and vertical mixing at the release point has less of an effect. The majority of the

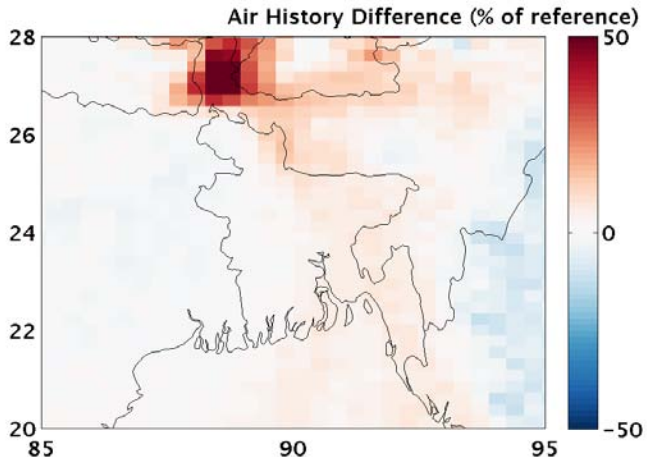

(a)

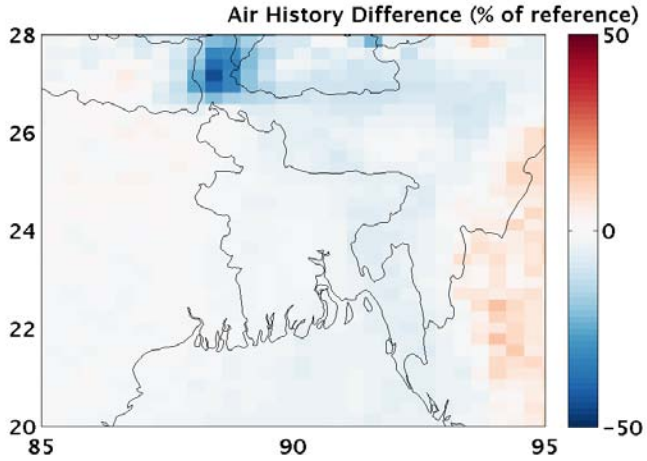

(b)

Figure 3-7: Average July percentage difference in surface influence from the reference (500 magl) particle release height for (a) 400 magl and (b) 600 magl.

contribution to this difference in mole fractions is from the grid cells in close proximity to the release point. Furthermore, it illustrates the effect of using a 100 m release column, an error that is incorporated into the air histories as particles are randomly released within this column but is not quantified in the final uncertainties. This analysis shows that small changes in the particle release height have a relatively small effect on simulated emissions, compared to other sources of error such as resolution. The effect of particle release height on emissions estimation is investigated further in Chapter 5.

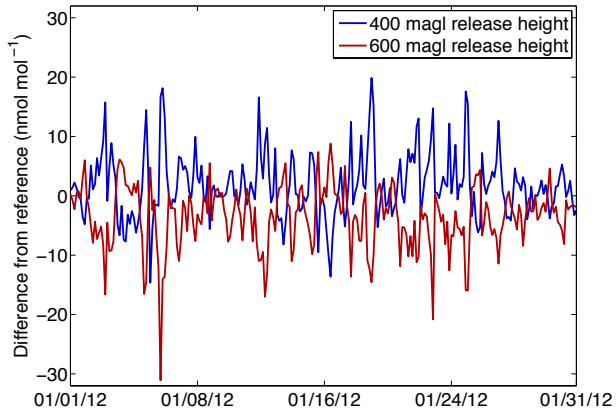

(a) CH_4

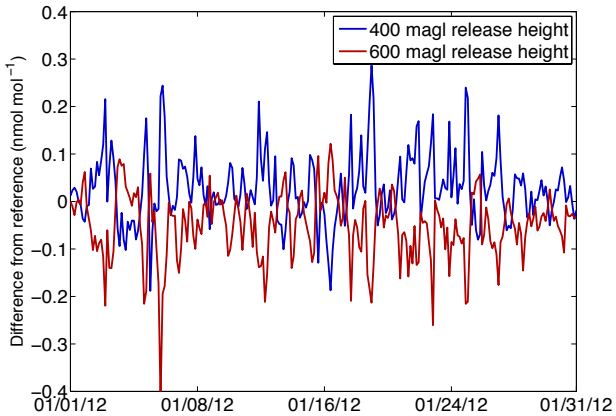

(b) N_2O

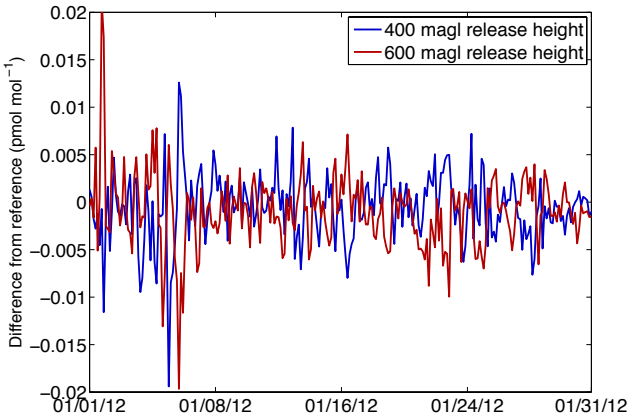

(c) SF_6

Figure 3-8: Effect of particle release height on mole fractions simulated at Darjeeling for January. Figures are shown as a difference in mole fractions between using a perturbed release height (400 magl, blue and 600 magl, red) and the reference release height (500 magl) for (a) CH_4 (b) N_2O (c) SF_6.

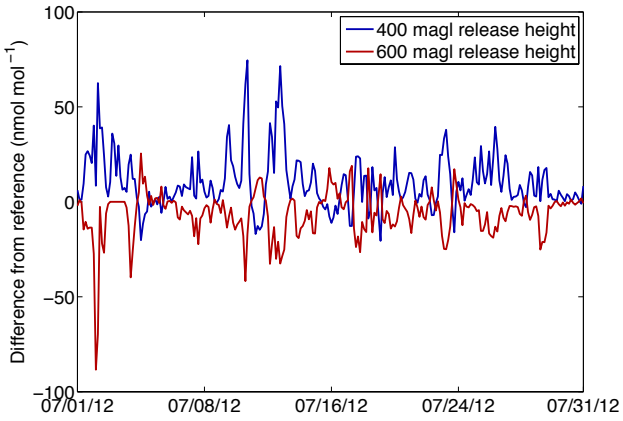

(a) CH_4

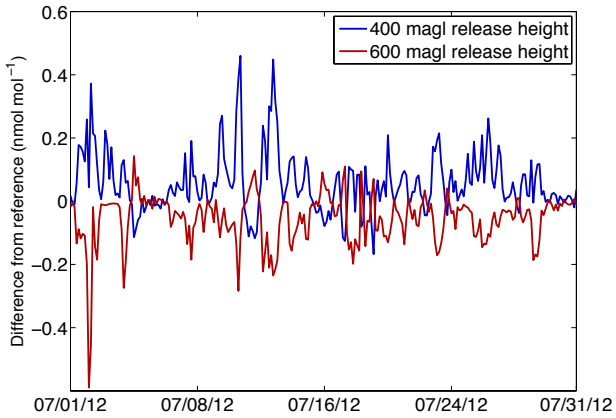

(b) N_2O

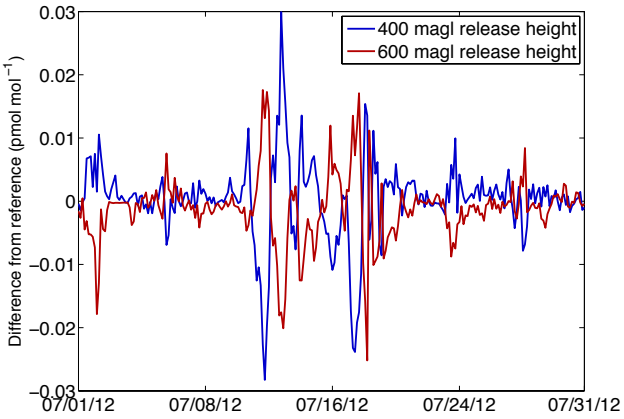

(c) SF_6

Figure 3-9: Effect of particle release height on mole fractions simulated at Darjeeling for July. Figures are shown as a difference in mole fractions between using a perturbed release height (400 magl, blue and 600 magl, red) and the reference release height (500 magl) for (a) CH_4 (b) N_2O (c) SF_6.

3.4 Comparison of Observed and Modeled Meteorology

Observed and model-derived wind speeds and wind directions are compared for each season in Figures 3-10, 3-11, 3-12 and 3-13. Modeled winds are shown at 10 and 500 magl, which are height just above the model surface and the particle release height, respectively. In all seasons, modeled and observed wind directions are generally consistent, though the observed wind directions show more variability. Wind speeds, however, are almost always larger in the 500 magl model winds, because surface friction becomes much smaller at this height in the model. This highlights the important tradeoff between the model's capability to capture the correct wind direction and the correct wind speed at mountain sites, both of which are critical for deriving the correct air histories. Above the boundary layer, winds are assumed to be geostrophically balanced and the Coriolis force is balanced by the pressure gradient force. When friction is introduced and wind speeds must equal zero at the surface, wind direction is turned clockwise with increasing height (in the Northern Hemisphere) so that the sum of the Coriolis and frictional forces balance the pressure gradient term. The decreasing effect of friction with height results in the classic Ekman spiral.

Wind speeds are typically lower at night than during the day, which is more dramatic when the diurnal winds predominate. The cause of this variability is due to the fact that upslope flows result from the heating of unstable air, which becomes turbulent and more unstable, enhancing vertical motion. At night, however, cool air descends and forms a stable nighttime inversion, which acts to suppress flow, the result of which is much weaker, laminar flows at night.

In January, 500 magl modeled and observed winds show very good agreement in wind direction but observed wind speeds are closer to the 10 magl modeled winds. Air flow is southerly during the day and northeasterly at night, which is consistent with the direction of plains-to-mountain winds . This diurnal shift in wind direction, which is well-captured by the model, is responsible for the 'lobes' seen in the winter air history maps (Figure 3-2a). As air shifts diurnally from both sides of Darjeeling,

the integrated effect is to show surface sensitivity to both sides. Wind speeds at Darjeeling maximize in April during the pre-monsoon period. The observed and 500 magl model wind direction show some inconsistency during the day, as the observed winds show more southeasterly flow than is represented in the model. Furthermore, the observed winds speeds are actually larger than the 500 magl modeled winds during the pre-monsoon, suggesting that 500 magl may not be the best particle release height for this period. A better match in wind direction is at 400 magl but wind speeds are again smaller than observed. The measured July wind speeds show slow, often stagnant, winds at Darjeeling and this is not well-captured in the model at 500 magl. Observed winds are more consistent with 10 magl modeled winds. This decrease in wind speed from pre-monsoon to monsoon results from the strong vertical motion in the Himalayas during this highly convective period, as shown in Figure 1-6. A similar comparison exists for October winds. Observed wind speeds are consistent with 10 magl modeled winds, but wind direction is more consistent with 500 magl modeled winds. The variability in agreement between measured and modeled wind direction during day and night and during different seasons suggests that variable particle release heights should be used to better represent the station during different periods, however, this method has not been incorporated in this study, as it requires the generation of new air history maps but will be implemented in the future.

It is assumed that the observed meteorology is representative of the large-scale (i.e., at 12 km model resolution) winds. In reality, the observed meteorology is strongly influenced by the local topography. Sensors are located close to the ridge top but a better representation of large-scale winds would be from observations made significantly above the ridge top. This could affect the conclusions of the comparisons made here, as both observed wind speed and directions would follow flow patterns around the local topography.

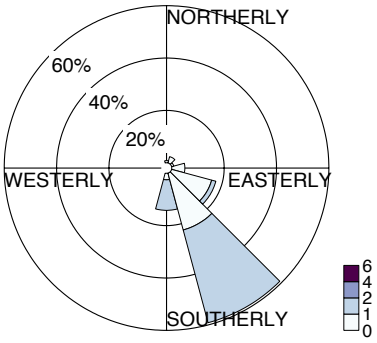

(a) 12pm-4pm, modeled 10 magl

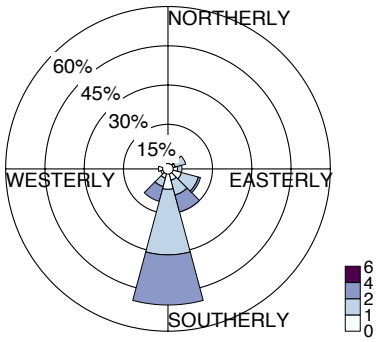

(b) 12pm-4pm, modeled 500 magl

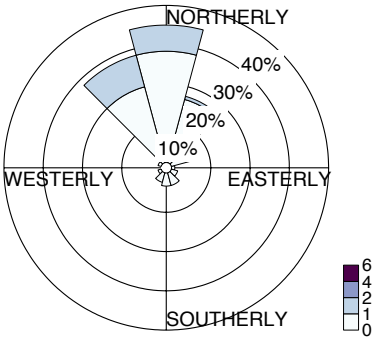

(c) 12am-4am, modeled 10 magl

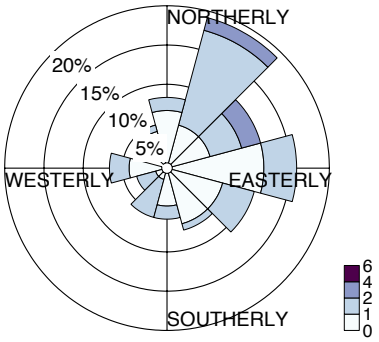

(d) 12am-4am, modeled 500 magl

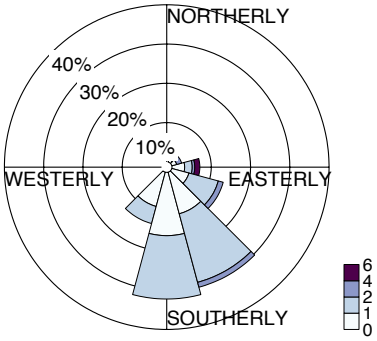

(e) 12pm-4pm, observed

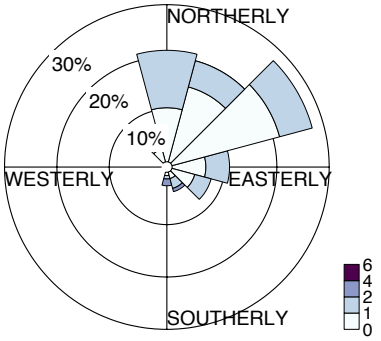

(f) 12am-4am, observed

Figure 3-10: January modeled and observed wind roses showing percentage of time with given wind direction and speed (colorbar, m/s) for (a) 12pm-4pm, 10 magl modeled winds (b) 12pm-4pm, 500 magl modeled winds (c) 12am-4am, 10 magl modeled winds (d) 12am-4am, 500 magl modeled winds (e) 12pm-4pm, observed winds at 15 magl (f) 12am-4am, observed winds at 15 magl.

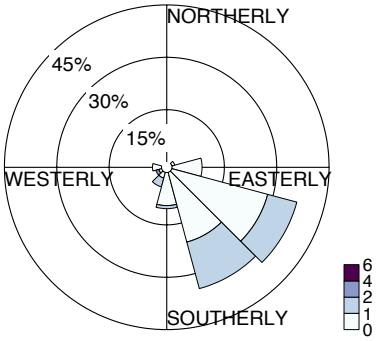

(a) 12pm-4pm, modeled 10 magl

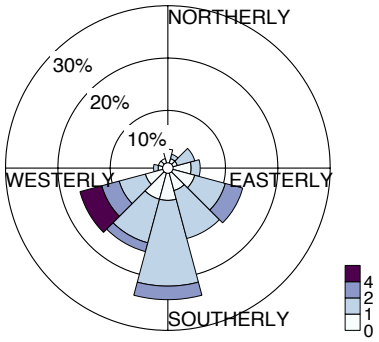

(b) 12pm-4pm, modeled 500 magl

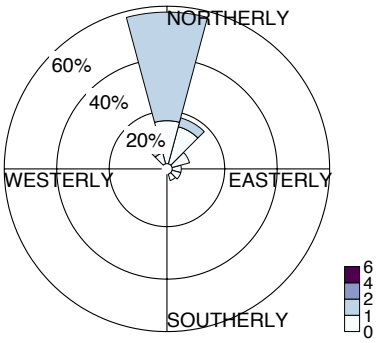

(c) 12am-4am, modeled 10 magl

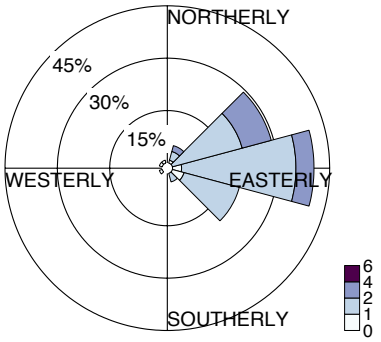

(d) 12am-4am, modeled 500 magl

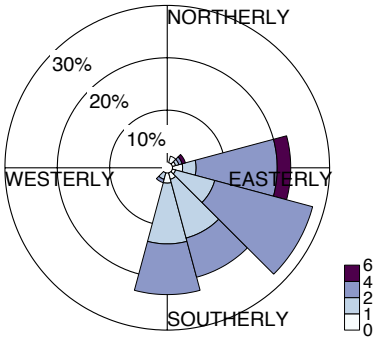

(e) 12pm-4pm, observed

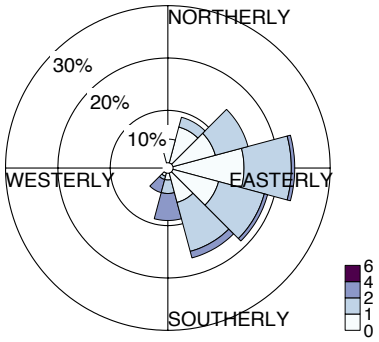

(f) 12am-4am, observed

Figure 3-11: April modeled and observed wind roses showing percentage of time with given wind direction and speed (colorbar, m/s) for (a) 12pm-4pm, 10 magl modeled winds (b) 12pm-4pm, 500 magl modeled winds (c) 12am-4am, 10 magl modeled winds (d) 12am-4am, 500 magl modeled winds (e) 12pm-4pm, observed winds at 15 magl (f) 12am-4am, observed winds at 15 magl.

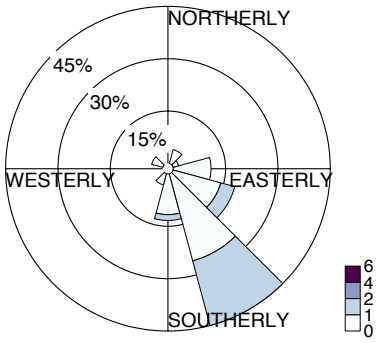

(a) 12pm-4pm, modeled 10 magl

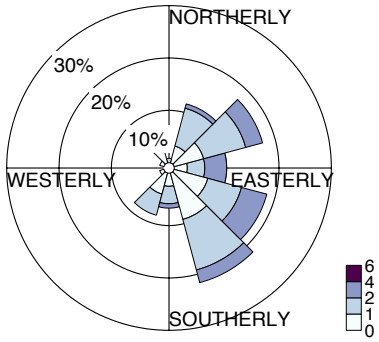

(b) 12pm-4pm, modeled 500 magl

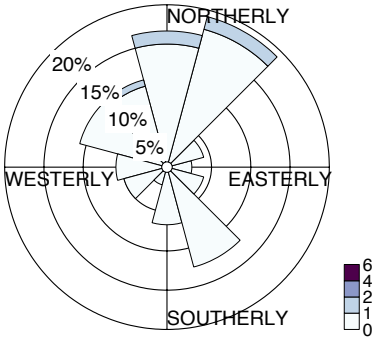

(c) 12am-4am, modeled 10 magl

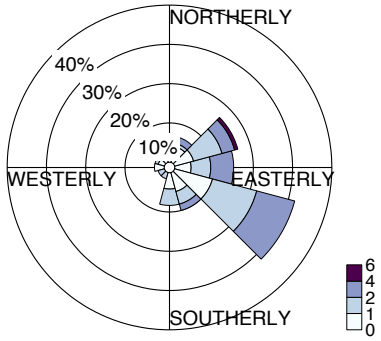

(d) 12am-4am, modeled 500 magl

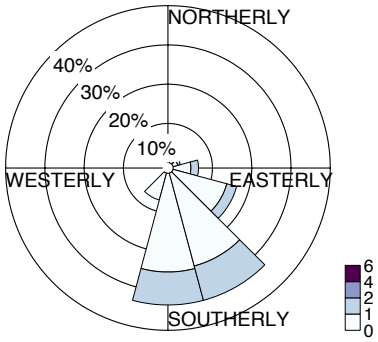

(e) 12pm-4pm, observed

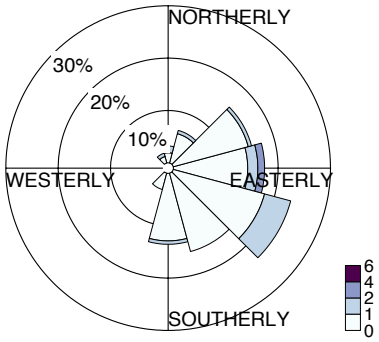

(f) 12am-4am, observed

Figure 3-12: July modeled and observed wind roses showing percentage of time with given wind direction and speed (colorbar, m/s) for (a) 12pm-4pm, 10 magl modeled winds (b) 12pm-4pm, 500 magl modeled winds (c) 12am-4am, 10 magl modeled winds (d) 12am-4am, 500 magl modeled winds (e) 12pm-4pm, observed winds at 15 magl (f) 12am-4am, observed winds at 15 magl.

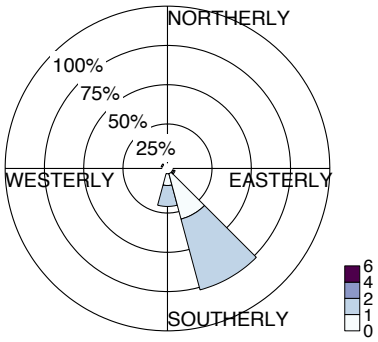

(a) 12pm-4pm, modeled 10 magl

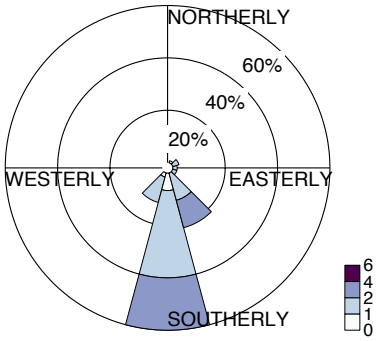

(b) 12pm-4pm, modeled 500 magl

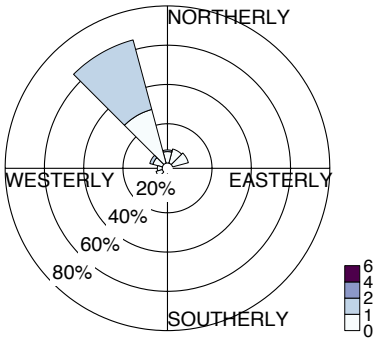

(c) 12am-4am, modeled 10 magl

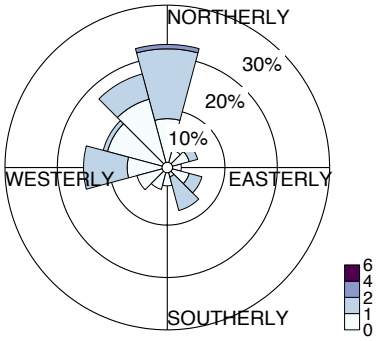

(d) 12am-4am, modeled 500 magl

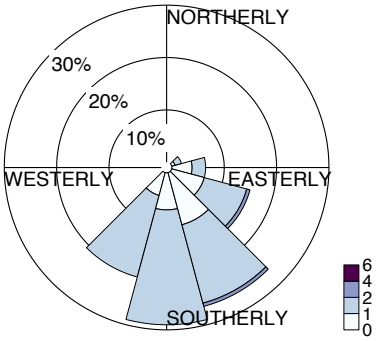

(e) 12pm-4pm, observed

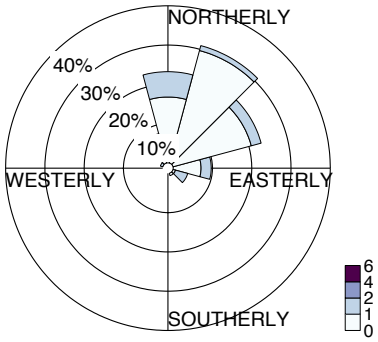

(f) 12am-4am, observed

Figure 3-13: October modeled and observed wind roses showing percentage of time with given wind direction and speed (colorbar, m/s) for (a) 12pm-4pm, 10 magl modeled winds (b) 12pm-4pm, 500 magl modeled winds (c) 12am-4am, 10 magl modeled winds (d) 12am-4am, 500 magl modeled winds (e) 12pm-4pm, observed winds at 15 magl (f) 12am-4am, observed winds at 15 magl.

Chapter 4

Trace Gas Measurements from Darjeeling

Measurements of CH_4, N_2O and SF_6 mole fractions from a new station in Darjeeling, India are presented from December 2011 for CH_4 and March 2012 for N_2O and SF_6 through November 2012 using methodology discussed in Chapter 2. In this chapter, these observations are discussed, including using NAME as a tool to diagnose important features within this dataset. Information about the particle dispersion model is found in Chapter 3.

4.1 Observed and Modeled Signals in Mole Fraction Measurements

Darjeeling regularly intercepts air with surrounding 'regional' pollution, air with 'local' influence and occasionally air that characterizes the 'background.' These three types of signals are defined broadly as characterizing emissions from South Asia, characterizing local Darjeeling emissions, and pertaining to a well-mixed state. Figure 4-1 shows the measurement time series for the three gases at Darjeeling and for comparison, at two AGAGE stations at higher and lower latitudes. Explanations for missing data are provided in Appendix A.

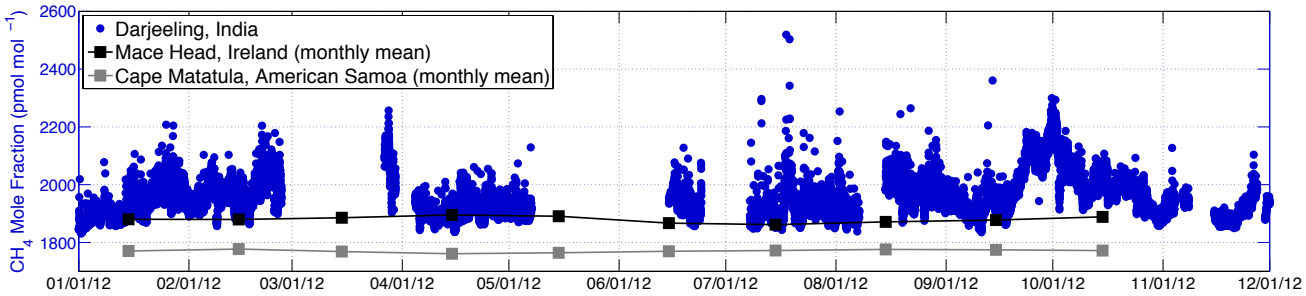

(a)

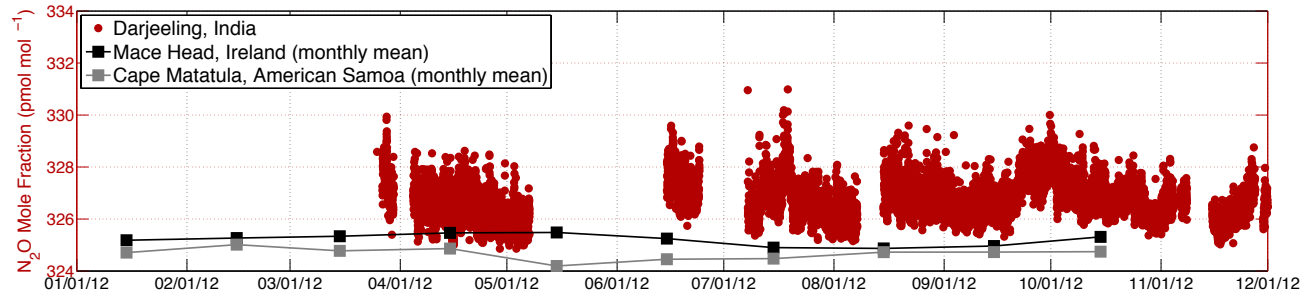

(b)

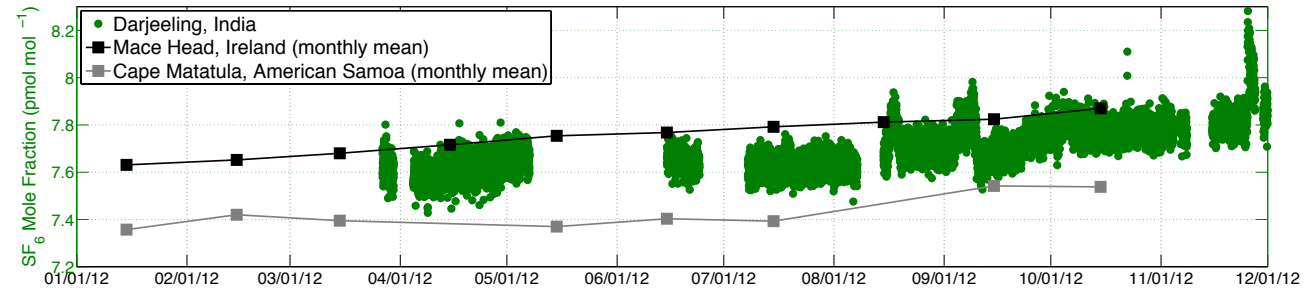

(c)

Figure 4-1: Measurements of (a) CH_4 (blue) (b) N_2O (red) and (c) SF_6 (green) mole fractions from January 2012 for CH_4 and March 2012 (for N_2O and SF_6) through November 2012. Monthly mean mole fractions from Mace Head, Ireland (black) and Cape Matatula, American Samoa (grey) are provided for comparison.

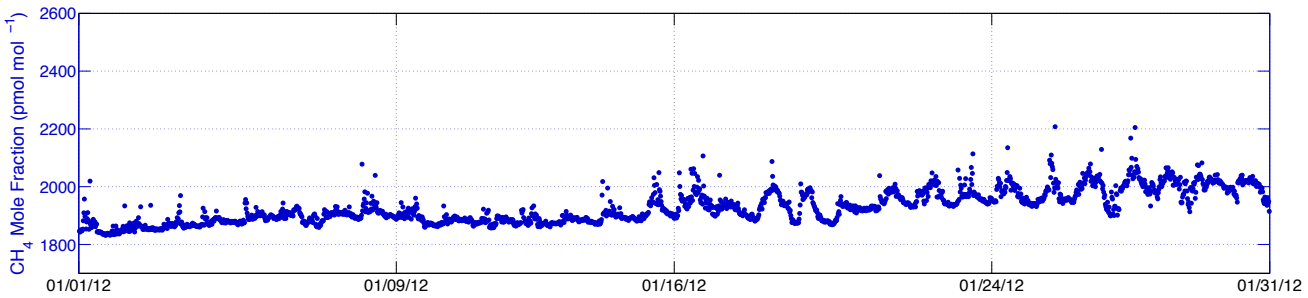

(a)

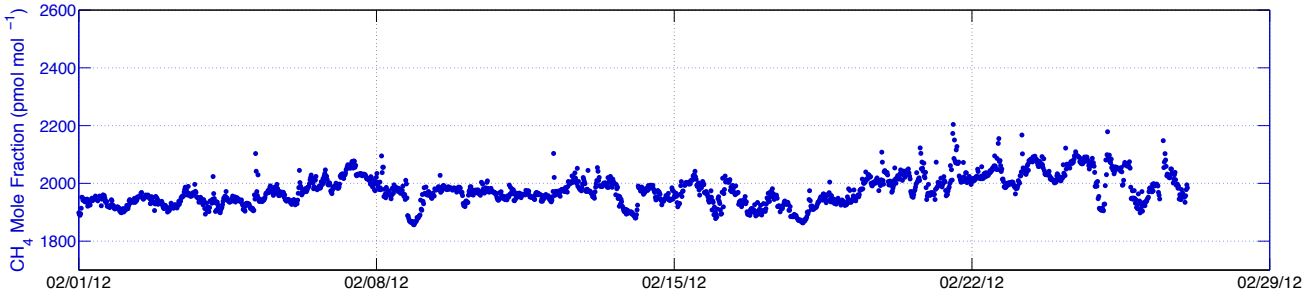

(b)

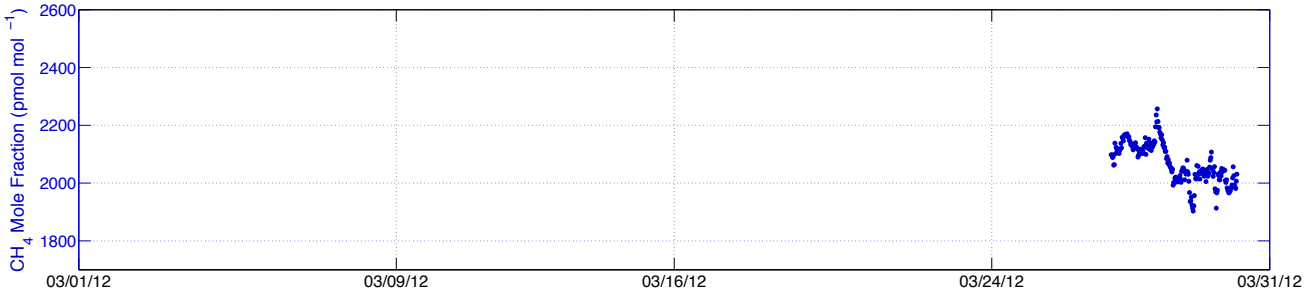

(c)

Figure 4-2: Measurements of CH_4 mole fractions from Darjeeling, India from (a) January (b) February (c) March 2012.

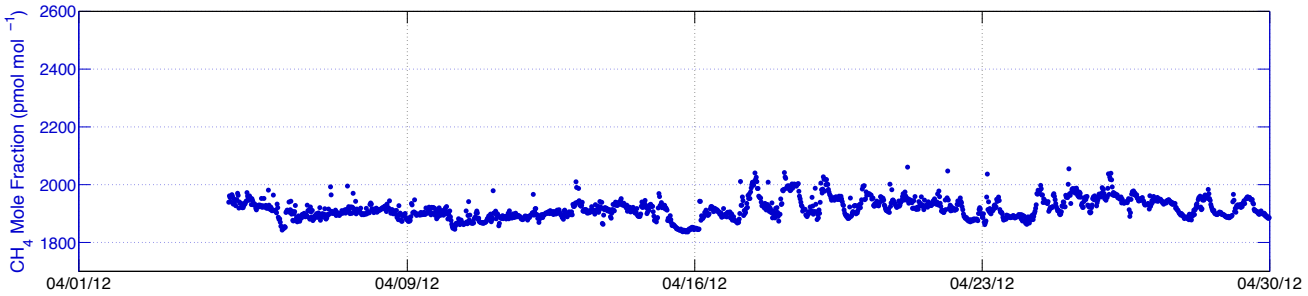

(a)

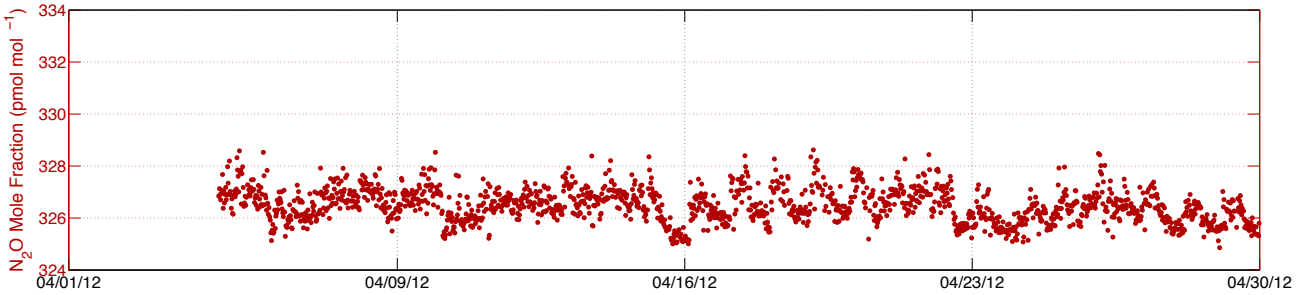

(b)

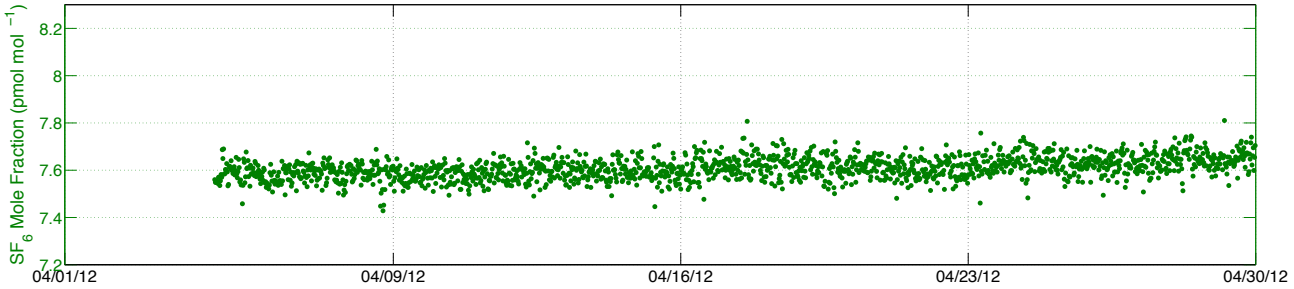

(c)

Figure 4-3: Measurements of (a) CH_4 (blue) (b) N_2O (red) and (c) SF_6 (green) mole fractions from Darjeeling, India from April 2012.

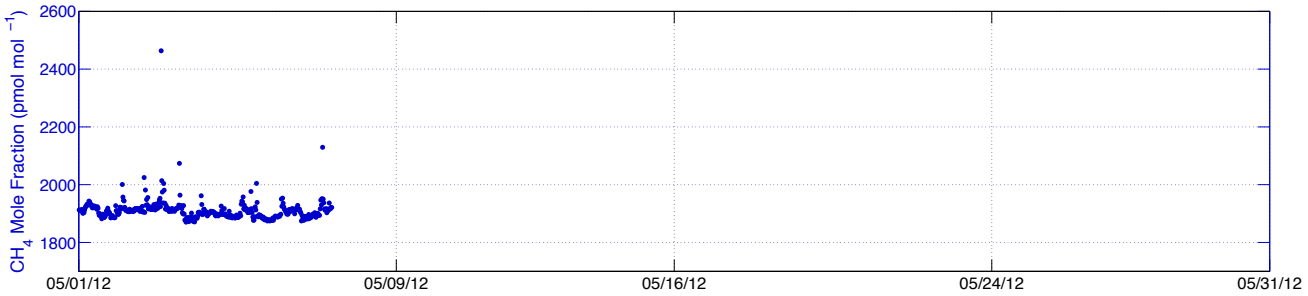

(a)

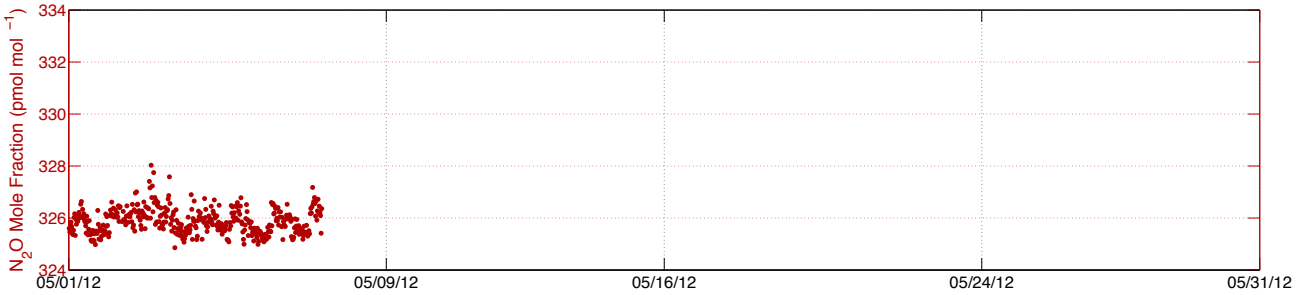

(b)

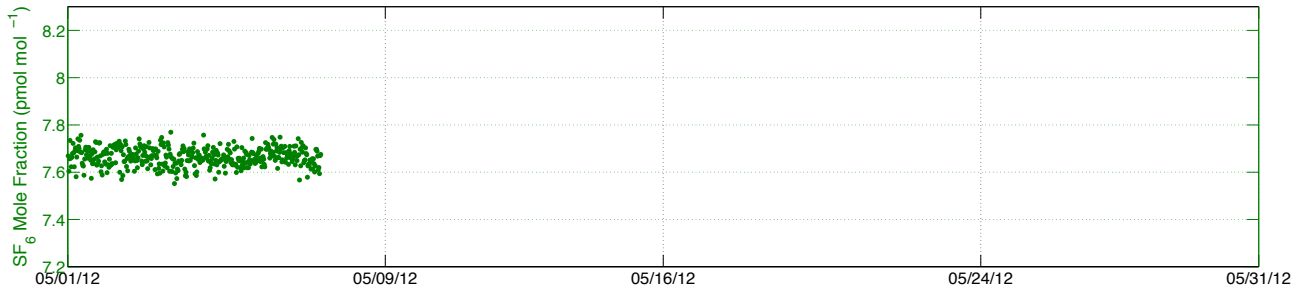

(c)

Figure 4-4: Measurements of (a) CH_4 (blue) (b) N_2O (red) and (c) SF_6 (green) mole fractions from Darjeeling, India from May 2012.

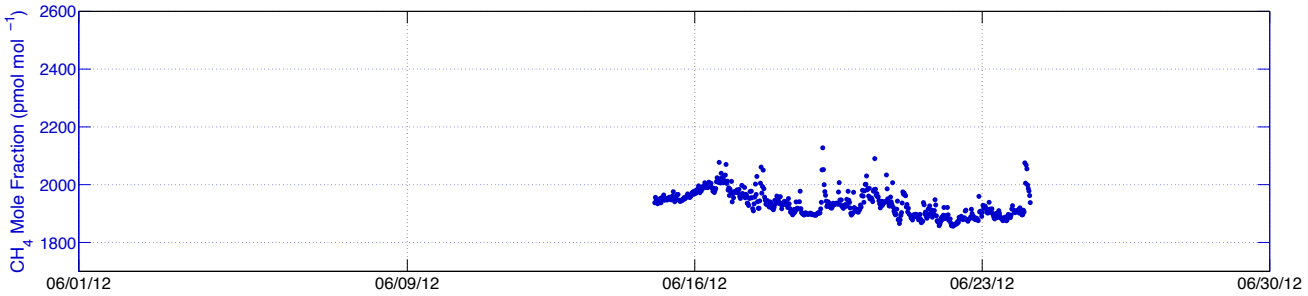

(a)

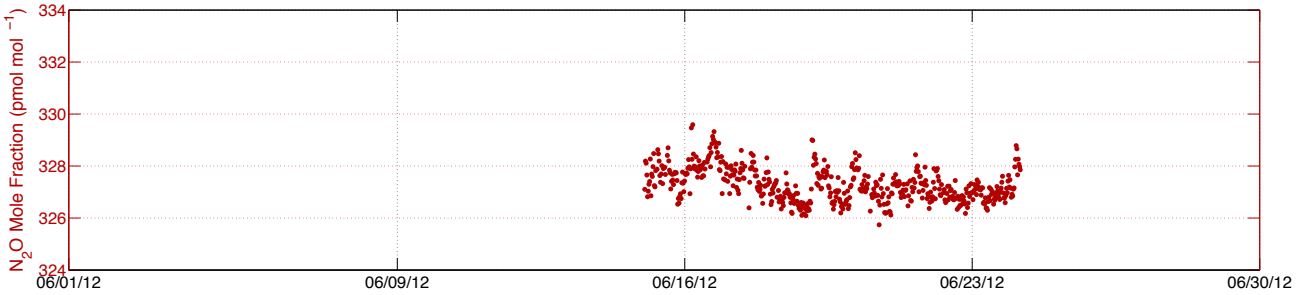

(b)

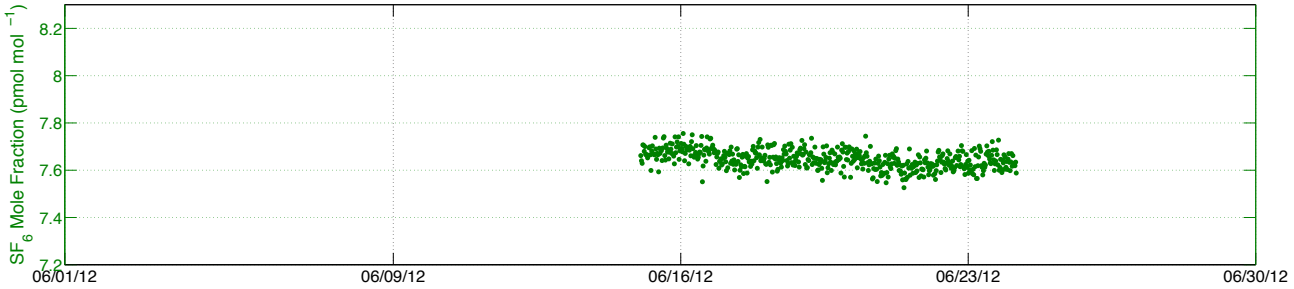

(c)

Figure 4-5: Measurements of (a) CH_4 (blue) (b) N_2O (red) and (c) SF_6 (green) mole fractions from Darjeeling, India from June 2012.

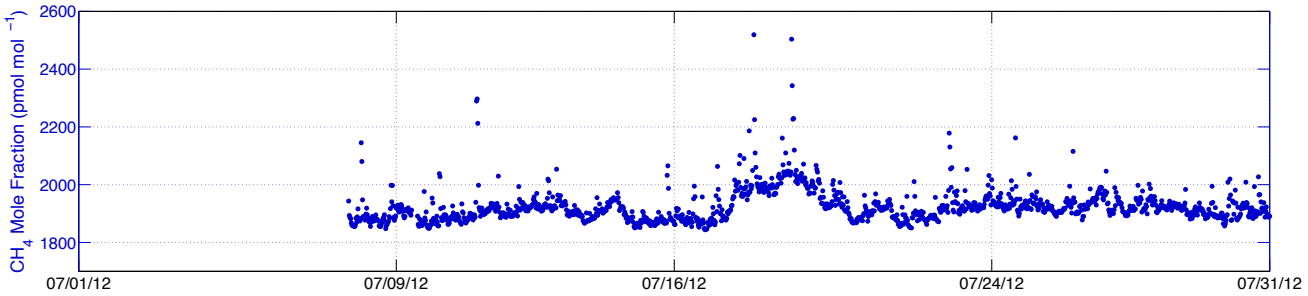

(a)

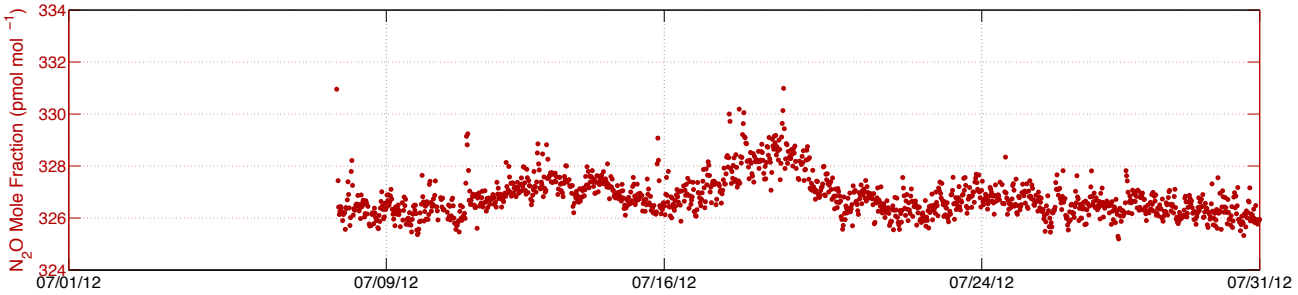

(b)

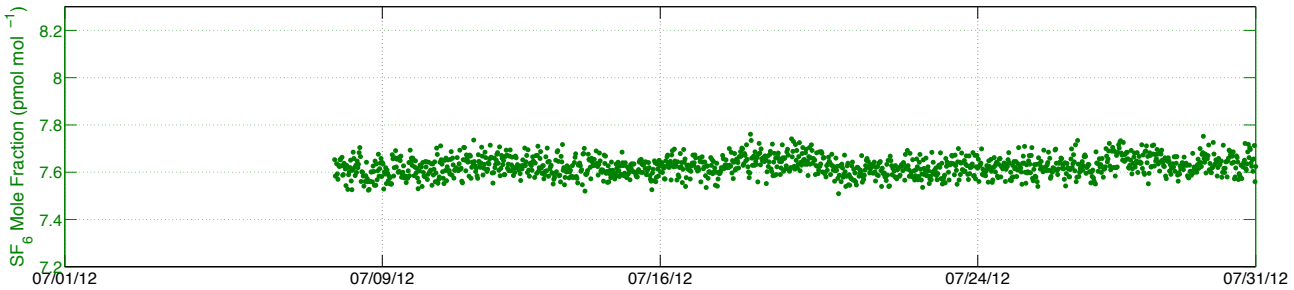

(c)

Figure 4-6: Measurements of (a) CH_4 (blue) (b) N_2O (red) and (c) SF_6 (green) mole fractions from Darjeeling, India from July 2012.

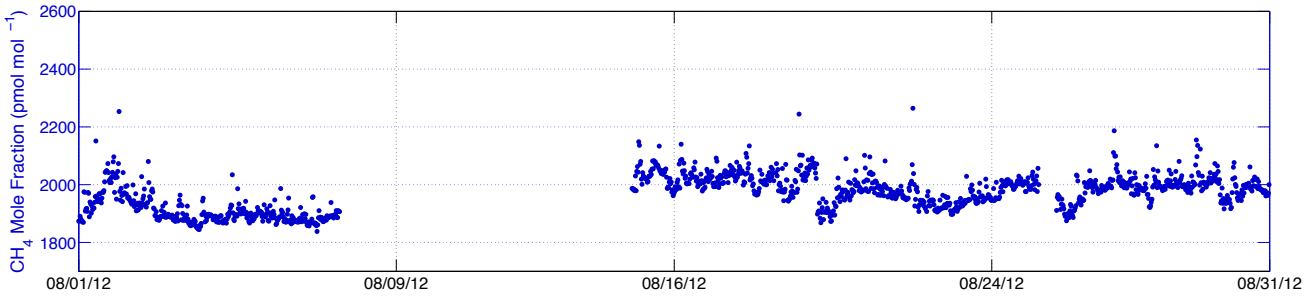

(a)

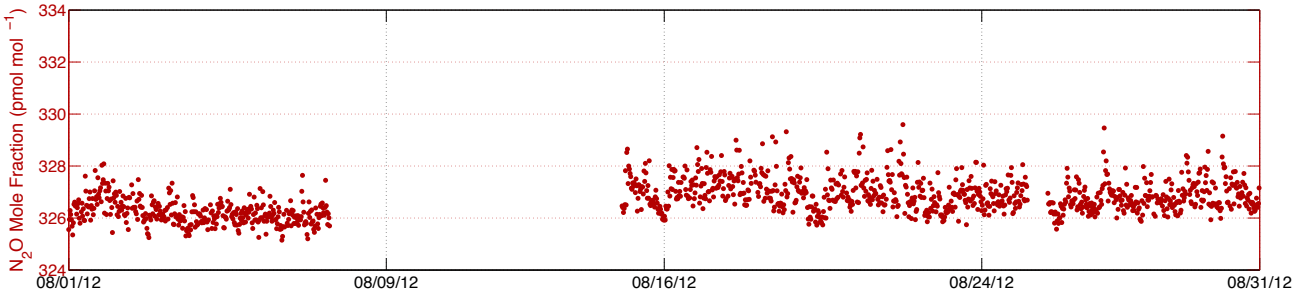

(b)

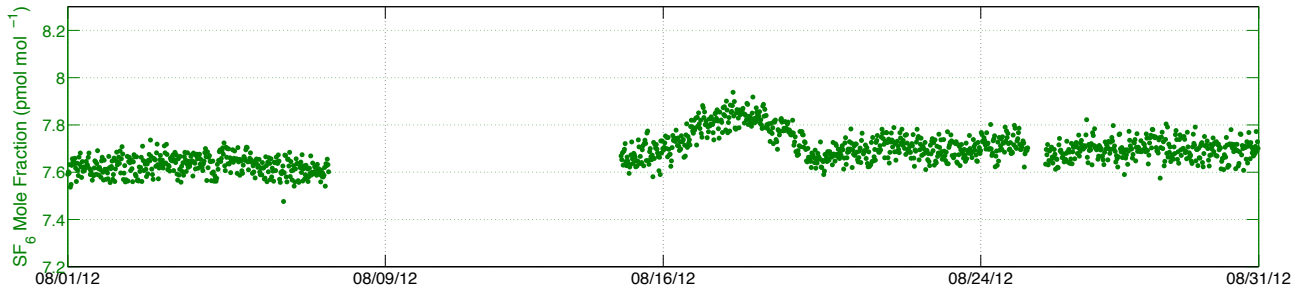

(c)

Figure 4-7: Measurements of (a) CH_4 (blue) (b) N_2O (red) and (c) SF_6 (green) mole fractions from Darjeeling, India from August 2012.

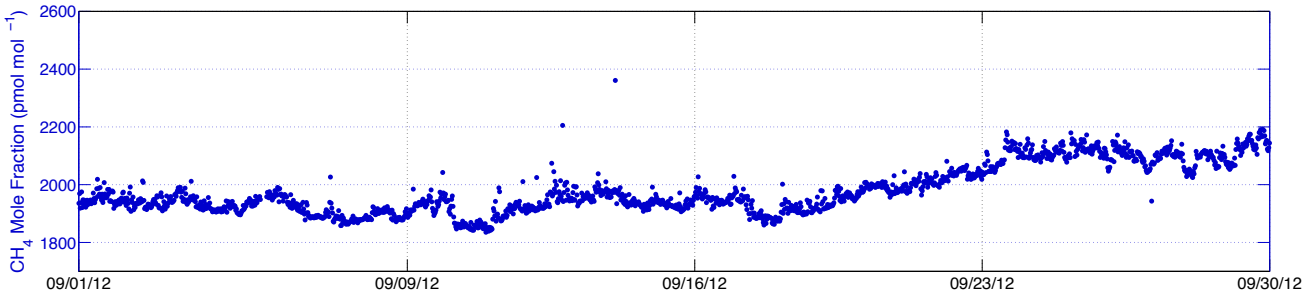

(a)

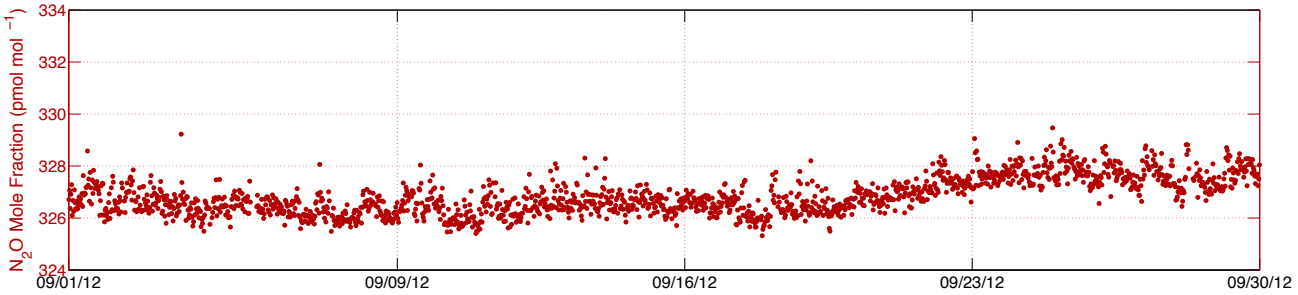

(b)

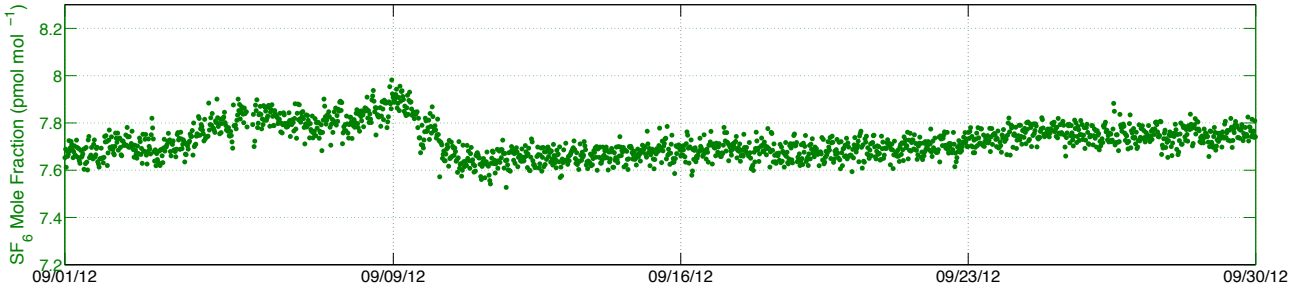

(c)

Figure 4-8: Measurements of (a) CH_4 (blue) (b) N_2O (red) and (c) SF_6 (green) mole fractions from Darjeeling, India from September 2012.

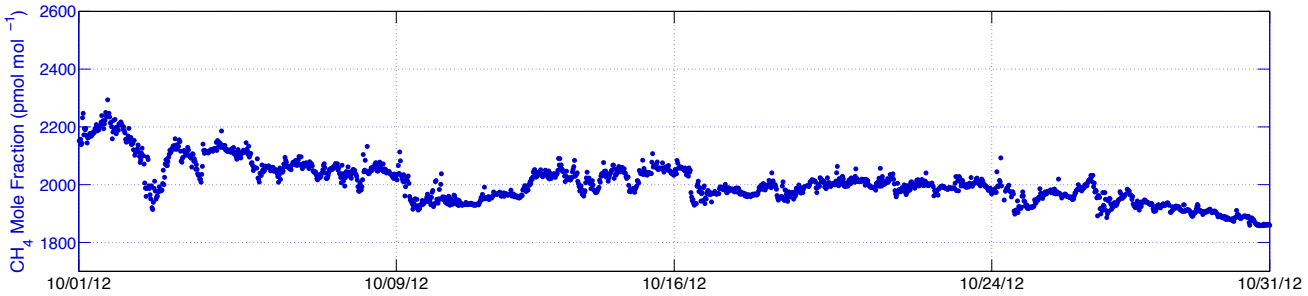

(a)

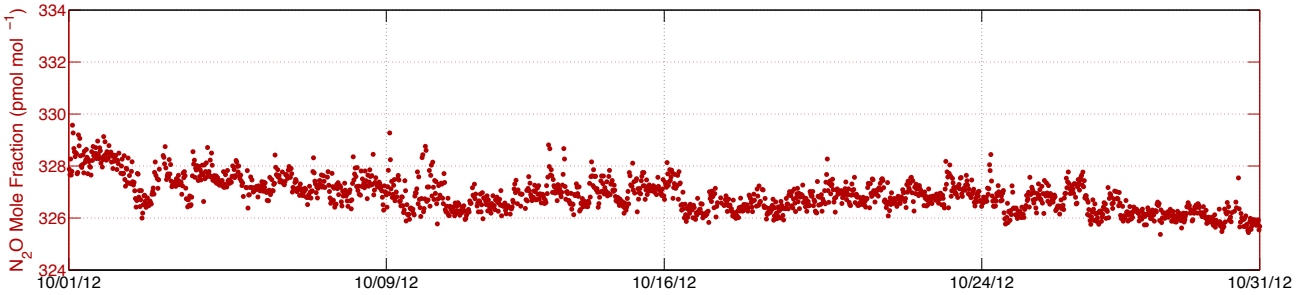

(b)

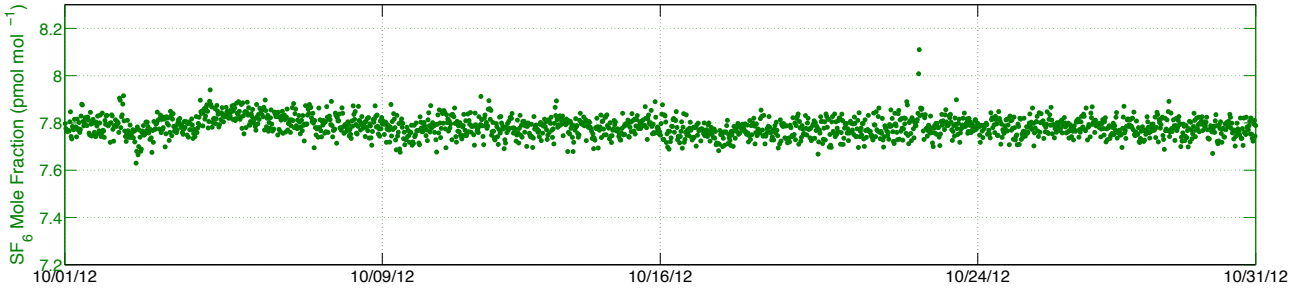

(c)

Figure 4-9: Measurements of (a) CH_4 (blue) (b) N_2O (red) and (c) SF_6 (green) mole fractions from Darjeeling, India from October 2012.

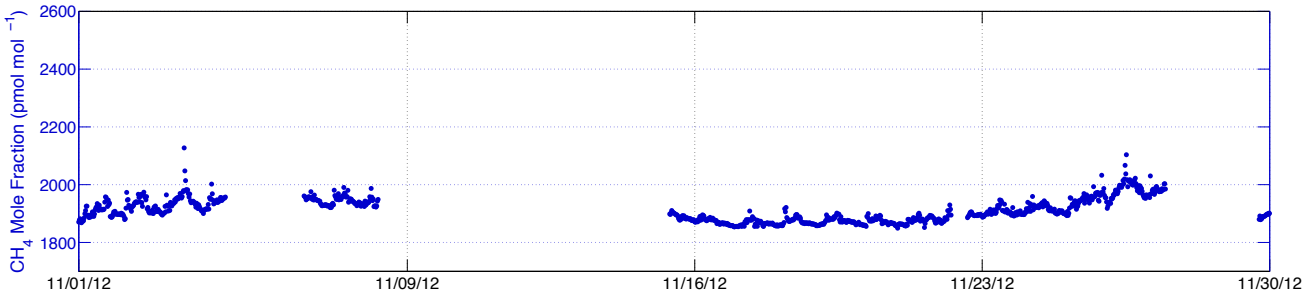

(a)

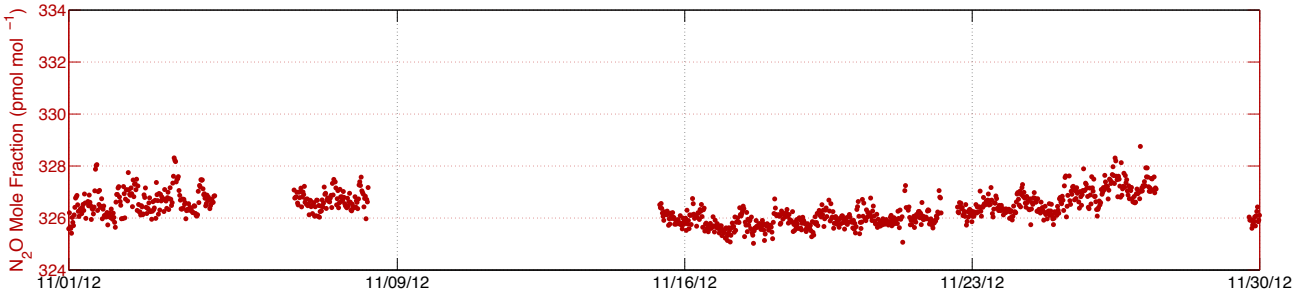

(b)

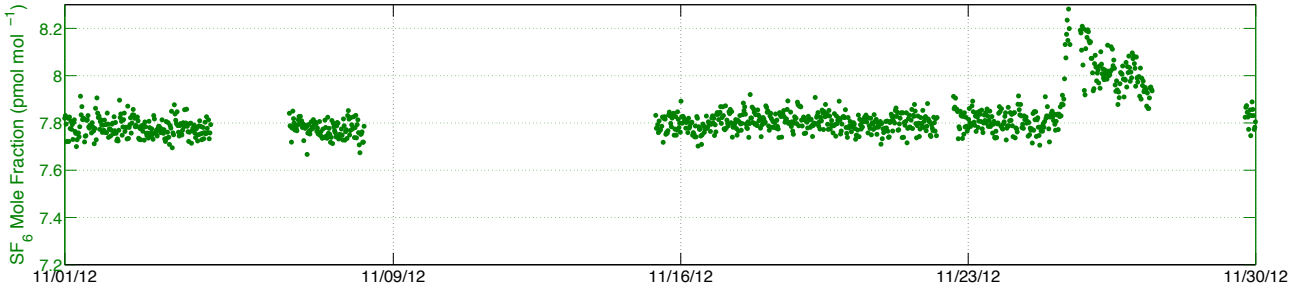

(c)

Figure 4-10: Measurements of (a) CH_4 (blue) (b) N_2O (red) and (c) SF_6 (green) mole fractions from Darjeeling, India from November 2012.

Table 4.1: Number of samples, monthly means, standard deviations for January through November 2012.

	CH_4			N_2O			SF_6		
Month	n	μ	σ	n	μ	σ	n	μ	σ
January	2221	1929.2	55.7						
February	1838	1957.8	51.1						
March	208	2070.0	68.3						
April	1720	1917.8	34.7	1686	326.46	0.65	1718	7.61	0.05
May	417	1910.0	37.7	409	325.88	0.48	417	7.66	0.04
June	537	1934.6	43.8	529	327.29	0.64	549	7.64	0.04
July	1441	1923.6	64.8	1429	326.78	0.77	1451	7.62	0.04
August	1385	1969.0	60.8	1352	326.73	0.67	1390	7.69	0.07
September	1785	1987.1	91.0	1753	326.88	0.74	1787	7.73	0.07
October	1827	2002.0	74.6	1809	326.87	0.66	1855	7.78	0.04
November	1097	1912.4	40.2	1077	326.39	0.57	1102	7.83	0.11

To begin, the SF_6 record is discussed. SF_6 generally has mole fractions that vary slowly with time. Though Darjeeling lies approximately halfway latitudinally between Ireland and Barbados, the signal is most similar in magnitude to that of Ragged Point and is lower than the signal measured at Mace Head. This could result from the Himalayas serving as a barrier to the transport of high latitude air to Darjeeling as well as from the fact that Darjeeling is at a higher altitude compared to Mace Head. In Figure 4-11, simulated mole fractions from the Model for OZone And Related chemical Tracers (MOZART) version 4.5 optimized using AGAGE and NOAA surface stations (excluding Darjeeling) show the SF_6 latitudinal gradient at AGAGE sites and at Darjeeling [Rigby et al., 2010]. Consistent with model output, Darjeeling SF_6 mole fractions are similar to Barbados mole fractions with small pollution events of the magnitude predicted by the model. This suggests that sources of SF_6 near Darjeeling are small, most often resulting in a slowly-varying background signal. Small pollution events typically occur at times when air passes over Southeast Asia prior to arrival at Darjeeling. Assuming that the SF_6 record roughly indicates Darjeeling's place within the latitudinal gradient, CH_4 and N_2O both have signals that are significantly elevated over this background level, and are additionally elevated over Mace Head levels. This suggests that there are strong regional sources present that almost always enhance the CH_4 and N_2O levels over the background, though at occasional times during the winter, their mole fractions exhibit excursions down to Barbados levels. This could imply either that background air is sampled occasionally or that cleaner tropospheric air is being sampled during times of subsidence (i.e. during the night).

CH_4 and N_2O often exhibit similar features and enhancement events, suggesting that regional sources are generally co-located. As the CH_4 and N_2O measurement systems only share common sampling, it is unlikely that measurement artifacts would lead to this correlation. Figure 4-12 shows one short period of the time series and highlights the correlation in pollution enhancements in the two gases. Though the timing of these enhancements are generally correlated, their enhancement ratios (i.e. relative size of the enhancement) are not always the same. This has been shown in CARIBIC measurements of vertical enhancements, suggesting that the temporal

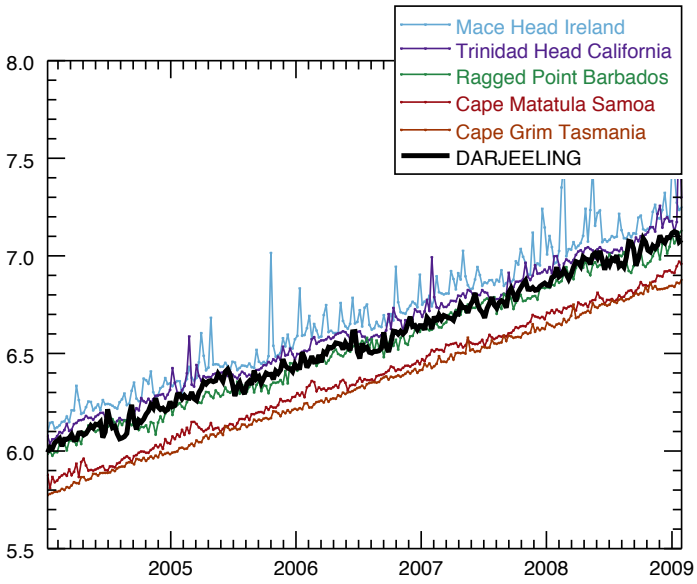

Figure 4-11: SF_6 mole fractions (pmol mol^{-1}) simulated by MOZART v4.5 using optimized emissions assimilated from AGAGE and NOAA surface station data [Rigby et al., 2010]. Modeled mole fractions from Darjeeling are shown by the thick black line. Figure courtesy of M. Rigby.

distribution of CH_4 and N_2O emissions are not concurrent [Schuck et al., 2010]. This finding implies that the enhancement ratios of the two gases would not be constant throughout the year.

The role of transport in enhancement events is illustrated by NAME air history maps derived for a point during a July CH_4 and N_2O enhancement and a point after the enhancement, as shown in Figure 4-12. In this July example, the enhancement shows sensitivity to surface air from Northern India while the period following the enhancement shows sensitivity to Southern India. As most of the sources lie in Northern India, this finding is consistent with the measurements.

The diurnal cycle is a prominent feature of the wintertime signal. The underlying cause of the diurnal cycle stems from orographic flows in the Himalayas, which are discussed in Section 1.6.1. Figures 4-13, 4-14 and 4-15 show median diurnal cycles for all three measured gases along with NAME-generated diurnal cycles for each season. These were normalized by subtracting the median value of each running 24 hour period

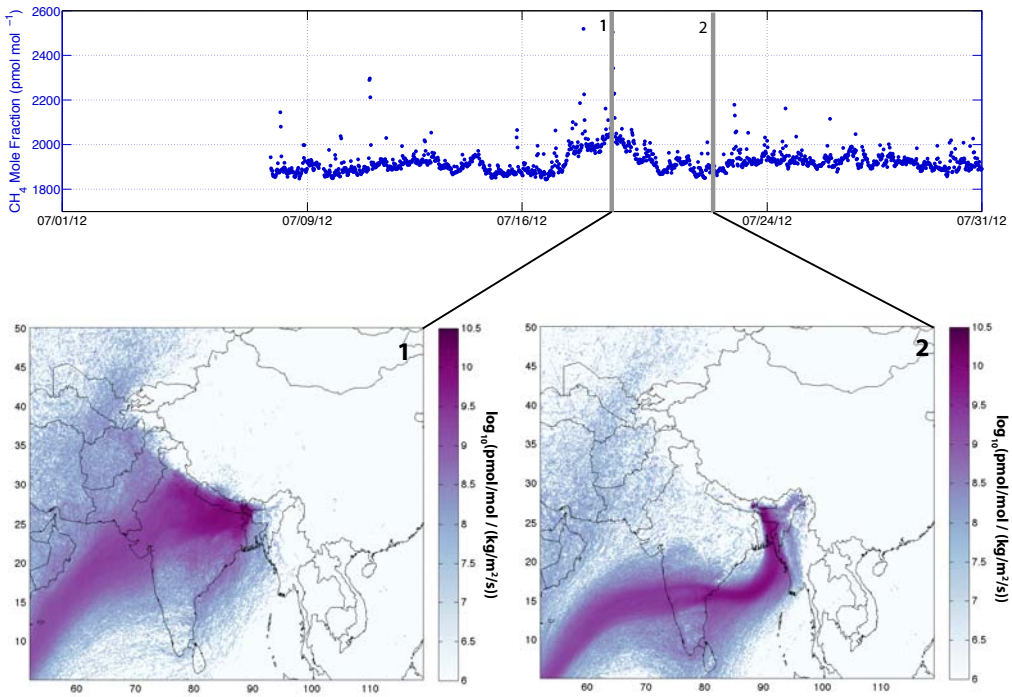

Figure 4-12: CH_4 and N_2O measurements from July 2012 showing a concurrent enhancement event along with air histories for measurements during and after the enhancement

from either the measurement or simulated time series and averaging over the month. The median was chosen for de-trending so that outliers (such as local pollution) would have less impact on the profile. Simulated mole fractions were generated using constant monthly emissions fields from inventories, which are discussed in Chapter 5. Variability in both the observed and simulated diurnal cycles were calculated as the 16th and 84th percentile values (equivalent to 1σ of Normal distribution).

The observed median diurnal cycles in CH_4 and N_2O mole fractions are significant during the winter and to a lesser degree during the spring and autumn but are not observed in the summer when variability during the month is greatest. Both CH_4 and N_2O mole fractions maximize in the afternoon and minimize during the night, though the N_2O diurnal cycle is smaller. A double peak is observed in both the CH_4 and N_2O diurnal cycles, with one peak between 7-9 am and a second peak at 3 pm. Small differences are seen between CH_4 and N_2O in both the monthly variability and seasonal differences in diurnal cycles but the general features are consistent. For

CH_4, the prominence of the morning peak changes from winter to summer. While the magnitude of the median morning peak signal remains similar in all seasons, variability in the morning peak grows from winter to summer and is smallest during the autumn. The morning peak may be a result of the ventilation of pollutants up to the site when a stable night-time inversion layer begins to break-up in the morning. This timing of the morning peak also shifts throughout the year as sunrise time shifts. The afternoon peak is much larger during winter than the summer and is likely caused by upslope flows and plains-to-mountain winds, which maximizes in the afternoon when the boundary layer is at its daily maximum. This type of double-peak is often seen in 'urban pollutants' such as carbon monoxide, where morning and evening rush hours lead to elevated mole fractions. However, vehicular emissions are not large sources of CH_4 and N_2O and it is thought that this feature is caused mainly by radiative effects rather than by an emissions signal. In SF_6, the diurnal cycle is not observed in any season. Sources near the Himalayas are too weak to create a diurnal signal that can be seen within the measurement precision.

The model-reproduced diurnal cycles in CH_4 and N_2O match the wintertime phase well, with a maximum in both the observed and modeled cycles at 3 pm. In spring, the timing of the afternoon phase is again well-captured but the morning peak begins to dominate. In summer, no significant diurnal cycle is seen in the model or observations and again, the morning peak is not captured. A small excursion at mid-day is seen in the model only during the summer but the large variability over the summer does not make this feature statistically meaningful. The morning peak is a feature that is not captured in NAME, suggesting that boundary layer processes at the resolution of the mountain-valley system are not captured at this resolution or are not captured using a 500 magl release height. The size and variability of the modeled diurnal cycles are dependent on the magnitude of emissions in the *a priori* emissions field and also assume constant monthly emissions, and is only presented as an approximation. Furthermore, the magnitude and variability of the modeled diurnal cycle is influenced by the choice of particle release height. The agreement of the phase of the diurnal cycle between model and measurements also suggests that

the underlying mechanism results from a large-scale flow. Experiments using NAME involving progressive removal of emissions from a growing radius around the site show that the diurnal cycle is preserved even when emissions are removed up to 100 km away. This suggests that the flow being modeled is a large-scale plains-to-mountain flow.

The seasonal differences in the diurnal cycle throughout the year is confirmed by the diurnal shift in wind direction measured throughout the year. Wind roses for day and night are shown for each season in Section 3.4. During the winter (Figure 3-10), a strong diurnal shift in wind direction is observed, with southerly winds during the day (corresponding to upslope and plains-to-mountain flow) and northerly flows at night (corresponding to downslope and mountain-to-plains flow). During the summer (Figure 3-12), the diurnal shift in wind direction is no longer evident.

Figure 4-16 shows the median sensible heat flux in January and July and is used to further diagnose the seasonal variability in the diurnal cycle. The winter diurnal sensible heat flux is considerably larger than in the summer, which could be a result of several factors: (1) winter days in Darjeeling are very clear and are generally cloud-free, resulting in more solar radiation reaching the surface; (2) the winter is very dry while the summer is moist, which results in solar radiation absorbed by the surface during the summer to be converted to latent heat flux (to evaporate/condense water) rather than to sensible heat flux (to heat/cool the atmosphere); (3) there is a strong southwesterly flow in the summer, which may dominate over the weaker diurnal flows. The change in sensible heat flux between winter and summer correlates with the differences in the size of the afternoon peak in the trace gas diurnal cycle.

CH_4 and N_2O both also exhibit high-frequency pollution, which has more prominence in the summer over the winter. In summer, the high-frequency signal is a larger component of the total signal, while in winter, the dominant signal is diurnal. Some of this high-frequency signal is caused by local emissions of CH_4 and N_2O but it is expected that the majority is caused by greater trace gas transport in the summer, due to the strong flow of the monsoon.

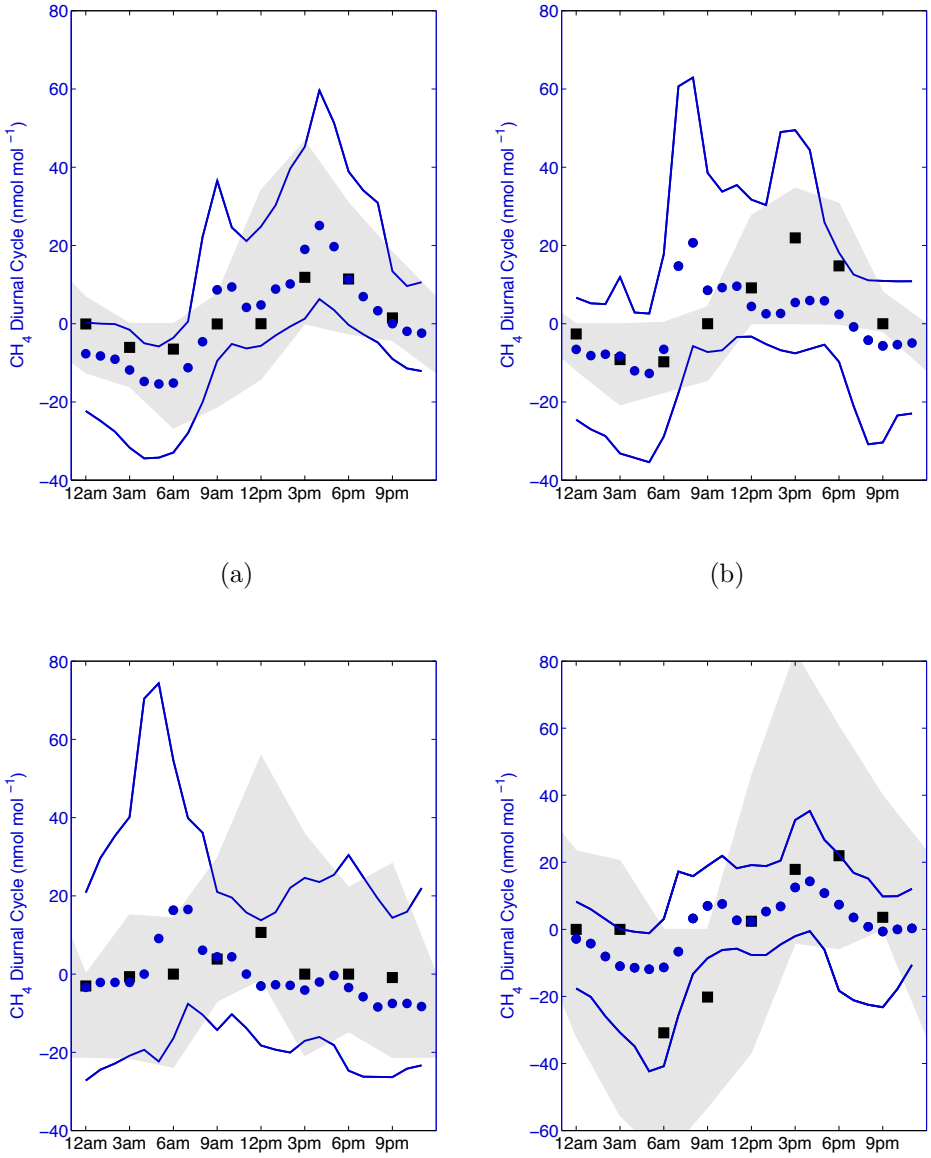

Figure 4-13: Observed (blue circles) and modeled (black squares) median CH_4 diurnal cycle for (a) January (b) April (c) July (d) October. The solid lines and shading show the 16th and 84th percentiles of the observed and modeled values, respectively, during each month.

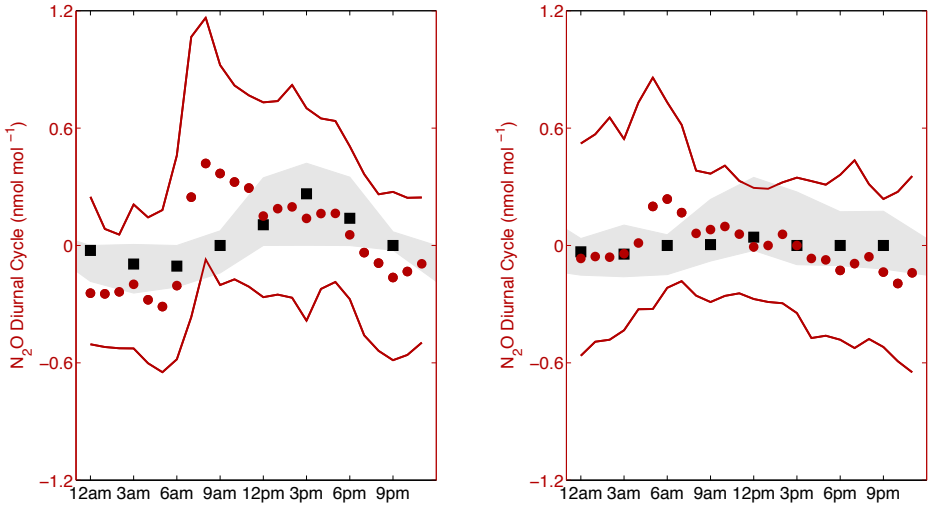

(a)

(b)

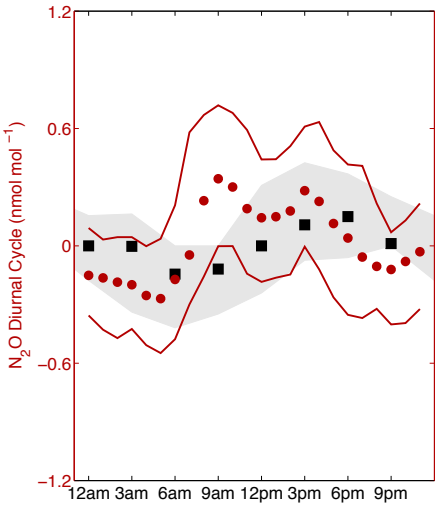

(c)

Figure 4-14: Observed (red circles) and modeled (black squares) median N_2O diurnal cycle for (a) April (b) July (c) October. The solid lines and shading show the 16th and 84th percentiles of the observed and modeled values, respectively, during each month.

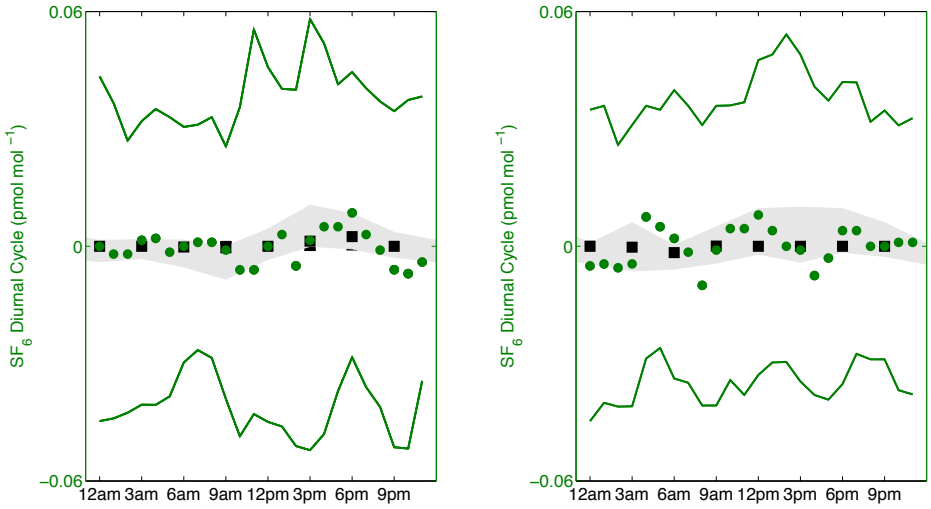

(a) (b)

Figure 4-15: Observed (green circles) and modeled (black squares) median SF_6 diurnal cycle for (a) April and (b) July. The solid lines and shading show the 16th and 84th percentiles of the observed and modeled values, respectively, during each month.

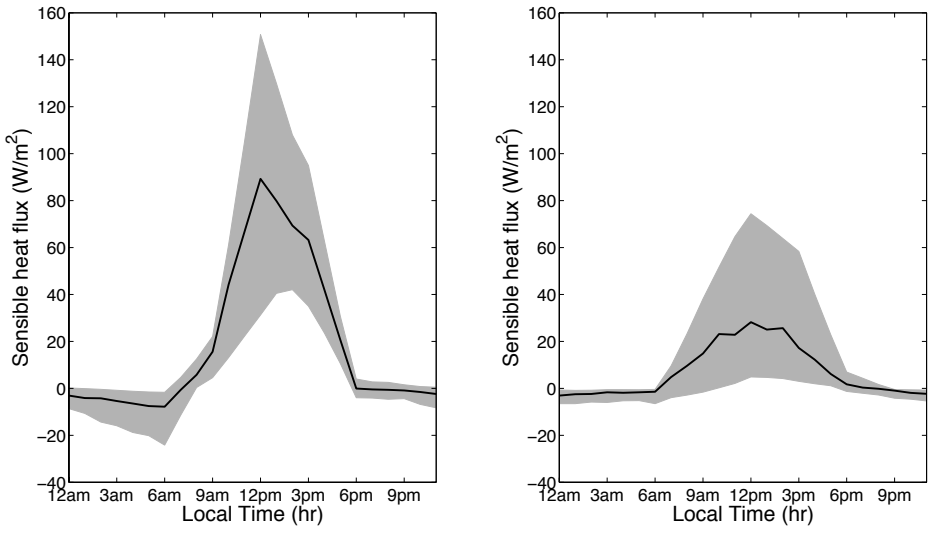

(a) January (b) July

Figure 4-16: Median sensible heat flux (W m^{-2}) generated by the Met Office's South Asia Model (SAM) for (a) January and (b) July. Shading shows the 16th and 84th percentiles.

Chapter 5

Inverse Modeling

The following sections discuss the inverse modeling approach for flux estimation using measurements of CH_4, N_2O and SF_6 mole fractions from Darjeeling, India, which were presented in Chapter 4. Chapter 3 described the Lagrangian Particle Dispersion Model, model inputs and the generation of 'air histories' that are used in these inverse modeling studies.

In Section 5.1, the approach of selecting boundary conditions to the model domain is discussed. Section 5.2 details the inverse modeling approach, including formulation of the method, *a priori* emissions, uncertainties and measurement filtering methods. Lastly, emissions estimates and resulting uncertainties for the three species are presented in Section 5.3.

5.1 Boundary Conditions

Simulated concentrations from the LPDM air histories contain the 'local' contribution to the measured concentration, which is the contribution of emissions from the 30 day period of the back trajectory. Boundary conditions to the domain account for emissions from farther back in time and contain the slowly varying component of the measured concentrations. In to order to meaningfully compare modeled and observed mole fractions, these boundary conditions need to be supplied. Several methods have been used in other studies to determine boundary conditions to the LPDM domain.

These methods include (1) solving for the part of the measured mixing ratio not modeled in the LPDM in the inversion [Stohl et al., 2009]; (2) identifying clean trajectories and utilizing those measurements that correspond to unpolluted air as the boundary conditions [Manning et al., 2011, 2003]; (3) utilizing a Eulerian model to provide boundary conditions to the LPDM [Rigby et al., 2011b].

In this study, boundary conditions were determined as part of the inversion using a modified approach of Stohl et al. [2009] by solving for an 'offset' to the four horizontal boundaries of the domain, which spans from 5-50°N and 50-120°E. In this method, the vertically-integrated number of particles in the edge boxes of the domain were tracked every three hours (to be consistent with the resolution of air histories) of the 30-day back trajectory period. The advantage of this approach is that boundary conditions can be estimated for each boundary independently. Therefore, as wind directions change, the boundary from which air enters the domain can be appropriately tracked. This method would account for a North-South gradient or for air entering one side of the domain with higher mole fractions (for example, air passing over the Middle East on the Western boundary is expected to contribute higher mole fractions than oceanic air entering the domain from the East or South). A fifth boundary that could be used but not implemented here is to add a vertical boundary (e.g., at the tropopause) to assess the impact of descending air.

Emissions and boundary conditions were estimated at monthly resolution. The underlying assumption of this method is that air masses directly outside the boundary are 'well-mixed' prior to reaching the measurement station, resulting in a boundary-induced variability over the month that is less than the measurement precision. An approximation to testing variability in boundary conditions was to test that the contribution of emissions just outside the boundaries (excluding the much larger offset cause by emissions even farther away) was less than the measurement precision. The smallest possible domain was desired to minimize computational expense. This assumption was validated by creating air history maps for 2012 over a very large computational region (∼-20-60°N, ∼45-130°E) and run for 40 days back. The domain was selected to be much larger than the region of interest (South Asia) but was also

limited by the available meteorology. As it is expected that of the three measured gases, CH_4 has the most significant sources in Asia, an *a priori* CH_4 emissions field for this large domain was used to simulate mole fractions (information about this emissions field is found in Section 5.2.1). To test the effect of boundary, a subset of the large domain was selected and emissions within the subset region were removed. This modified emissions field was used to simulate a time series at the measurement site. Each boundary was then moved inward, a new emissions field was generated with emissions removed in the smaller domain and a new time series was simulated. Boundaries were moved inward until the smallest possible domain was achieved that also resulted in emissions from 'outside' the boundary contributing to Darjeeling mole fractions by less than measurement precision of 1.5 nmol mol^{-1} for CH_4 (schematic of this process shown in Figure 5-1). The contribution of emissions 'outside' the boundary, that is emissions between the small boundary and large boundary, to Darjeeling mole fractions are shown in Figure 5-2.

The choice of running the model backwards for 30-days was validated by tracking the total number of particles in the domain. By the end of the simulation, the majority (>95%) of particles must have left the domain for all air history maps and the run duration was varied from 15 to 30 days to test the effect of run time. A simulation period of 30 days was selected as the requisite run duration for the model studies used here.

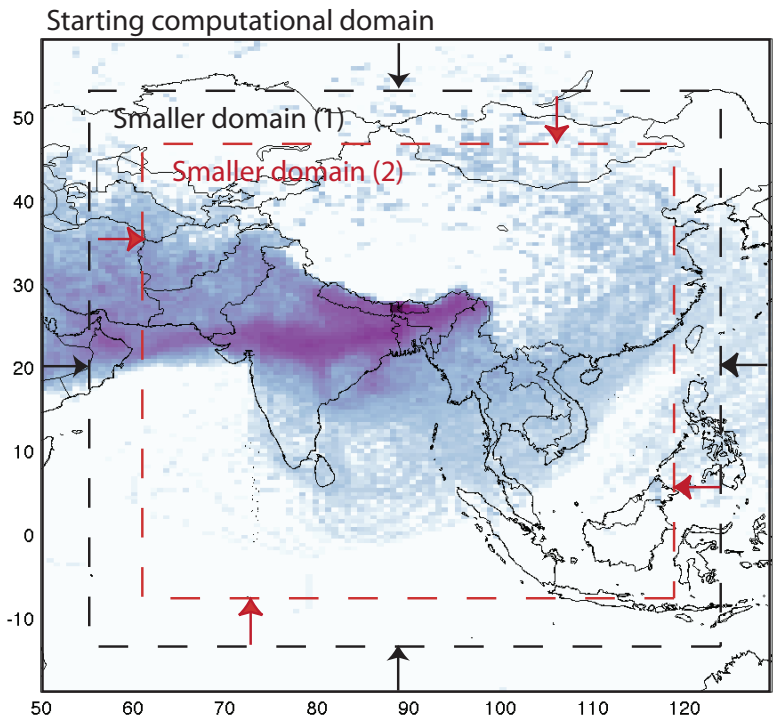

Figure 5-1: Schematic of boundary selection procedure. Domain is moved inward from a large initial computational domain. The contribution of emissions between the smaller region and large, initial region on Darjeeling mole fractions is calculated. The small domain is moved inward until the smallest possible domain is selected where emissions from 'outside' the domain contribute to Darjeeling mole fractions by less than the measurement precision.

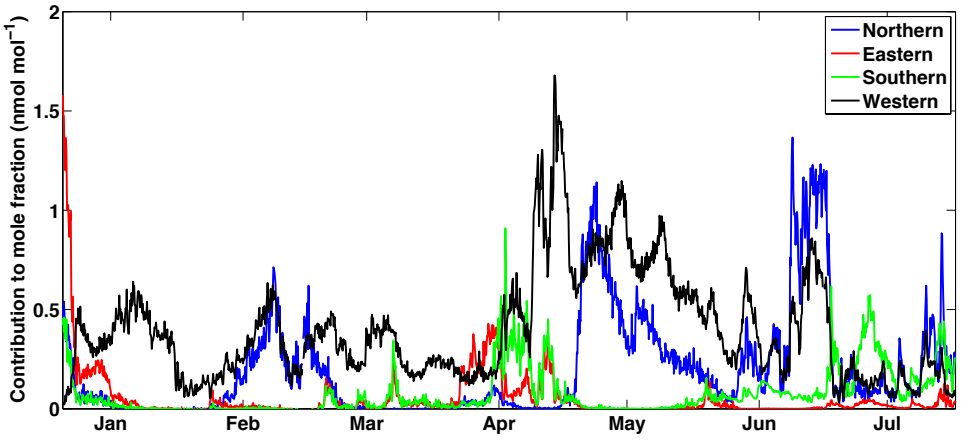

Figure 5-2: Contribution of CH_4 emissions from 'outside' each boundary (i.e., between boundary of small domain and the large initial domain) to mole fractions at Darjeeling (excluding the offset caused by emissions much farther away).

5.2 Inverse Method

Using measurements from January 2012 for CH_4 and April 2012 for N_2O and SF_6 through November 2012, surface emissions and boundary conditions to the four horizontal boundaries were estimated monthly. This method assumes constant values over each month, which could result in aggregation errors. Ideally, emissions and boundary conditions would be estimated at the resolution of the measurements and aggregated into monthly emissions, however, this has increased computational expense.

Surface emissions and boundary conditions were estimated by minimizing the cost function in Equation 5.1 and using the definition of the state vector shown in Equation 5.2.

$$J = (\mathbf{y} - \mathbf{y}_{model})^T \mathbf{R}^{-1} (\mathbf{y} - \mathbf{y}_{model}) + (\mathbf{x} - \mathbf{x}_{prior})^T \mathbf{P}^{-1} (\mathbf{x} - \mathbf{x}_{prior}) \tag{5.1}$$

$$\mathbf{x} = [\mathbf{x}_{scalingfactors}; \mathbf{x}_{boundaryconditions}] \tag{5.2}$$

Here, $\mathbf{y}$ is a vector of m observations over k months, $\mathbf{x}$ is the state vector of length n comprising p unitless emissions 'scaling factors' and s mole fractions at each boundary for each monthly period, $\mathbf{H}$ is a mxn Jacobian matrix governing the sensitivity of mole fractions to changes in the scaling factors and boundary mole fractions, $\mathbf{x}_{prior}$ is a set of prior values for $\mathbf{x}$, $\mathbf{R}$ is a mxm measurement error covariance matrix and $\mathbf{P}$ is a nxn prior error covariance matrix. It is assumed here that each measurement and prior emissions from each region are uncorrelated and thus $\mathbf{R}$ and $\mathbf{P}$ only comprise diagonal elements.

Mole fractions are simulated through Equations 5.3 and 5.4 as illustrated in Figure 5-3. By choosing this exponential formulation, it is constrained so that emissions cannot be negative.

$$\mathbf{q}_j = \mathbf{q}_{prior,j} exp(\mathbf{x}_{scalingfactors,j}) \tag{5.3}$$

$$\mathbf{y}_{model,ij} = \mathbf{f}_i \mathbf{q}_j + \mathbf{g}_i \mathbf{x}_{boundaryconditions,j} \tag{5.4}$$

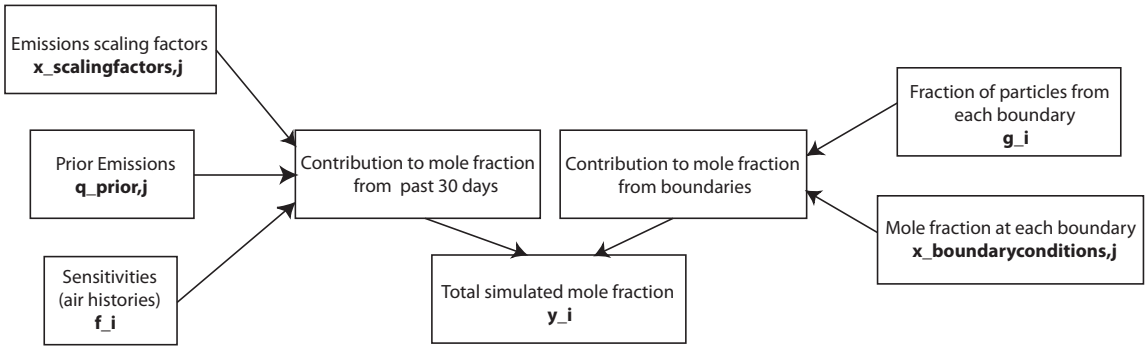

Figure 5-3: Flow diagram of the transformation between the state vector and simulated mole fractions for a given measurement time i and month j.

where i corresponds to a specific measurement ($i = 1 \ldots m$) and j corresponds to a specific month ($j = 1 \ldots k$), $\mathbf{f}_i$ is a vector of p sensitivities (for p regions) corresponding to measurement time i, $\mathbf{g}_i$ is a vector of four boundary condition fractions corresponding to measurement time i and $\mathbf{q}_{prior,j}$ is a vector of p prior emissions (g m^{-2} s^{-1}) corresponding to month j.

NAME air histories were output at 0.352°x0.234° and three-hourly resolution. For the inversion, grid cells were aggregated into small emitting regions (following the procedure in Rigby et al. [2011b] supplemental material). This was done for computational efficiency and so that each aggregated region contributed roughly equally to mole fractions at Darjeeling. The domain was first transformed into a distribution of mole fractions by multiplying annual mean sensitivity (i.e., derived from air histories) and annual mean *a priori* emissions for each grid cell. A region began around the grid cell with maximum contribution to mole fraction and this region grew in size until the total contribution from the region reached a threshold (in this case, 10% of average measurement uncertainty). Upon reaching the threshold, a new region grew from the next largest contributor to mole fraction that had not been already allocated. By following this procedure, regions were defined so that an area with

low sensitivity but high *a priori* emissions would be estimated at higher resolution than a region with low sensitivity and low emissions. By using the annual mean sensitivity and *a priori* emissions, one set of regions was assumed for each gas for the entire period. Grid cells with zero *a priori* emissions were aggregated into one region. Maps depicting the regions created for each species are found in Appendix B. It is not expected for inversion results to be highly sensitive to this process. The greatest difference will arise between an inversion using a large number of regions versus one with few regions, as aggregation errors will be more significant with fewer regions.

Emissions ($\mathbf{q}$) and sensitivities ($\mathbf{f}$) for each region were aggregated following Equation 5.5 and 5.6 for c grid cells comprising region b. Sensitivities in each region were weighted by the distribution in the *a priori* emissions field, therefore accounting for variations in emissions within each region. This weighting assumes that the *a priori* distribution within each region is correct. An a priori distribution that is incorrect, would lead to aggregation errors, though likely smaller than the errors that would result if a uniform distribution were assumed.

$$q_b = \sum_c q_c \tag{5.5}$$

$$f_b = \frac{\sum_c f_c q_c}{\sum_c q_c} \tag{5.6}$$

Newton's method of optimization iteratively 'descends' down the cost function by computing the Hessian (i.e., second derivative) to determine the local curvature of the cost function. The cost function is approximated by a quadratic that is tangent to the cost function at a local position and a minimum of the quadratic is used at each local position (Equations 5.7 and 5.8). From each point, a new quadratic is fit and in this iterative fashion, the cost function is 'mapped' (Figure 5-4). In the Quasi-Newton method, which was employed here, some small terms that arise from the calculation of the Hessian are discarded to simplify the calculation (see Tarantola [2005] for full discussion). $\mathbf{H_n}$ was determined by perturbing each element of $\mathbf{x}_{scalingfactor}$ by a small

value during each iteration and computing sensitivities using Equation 5.4. It is clear from Equations 5.3 and 5.4 that $\frac{\partial \mathbf{y}}{\partial \mathbf{x}}$ is nonlinear, so $\mathbf{H}_n$ is linearized around the local value of $\mathbf{x}$ at each iteration. By design, the partial derivatives governing the change in mole fraction at the receptor to changes in the boundary conditions are always unity and is kept linear for simplicity.

$$\mathbf{x}_{n+1} = \mathbf{x}_n - \mu_n \mathbf{Q}_n \left(\mathbf{H}_n^T \mathbf{R}^{-1} (\mathbf{y}_{model,n} - \mathbf{y}) + \mathbf{P}^{-1} (\mathbf{x}_n - \mathbf{x}_{prior}) \right) \tag{5.7}$$

$$\mathbf{Q}_n = \left(\mathbf{H}_n^T \mathbf{R}^{-1} \mathbf{H}_n + \mathbf{P}^{-1} \right)^{-1} \tag{5.8}$$

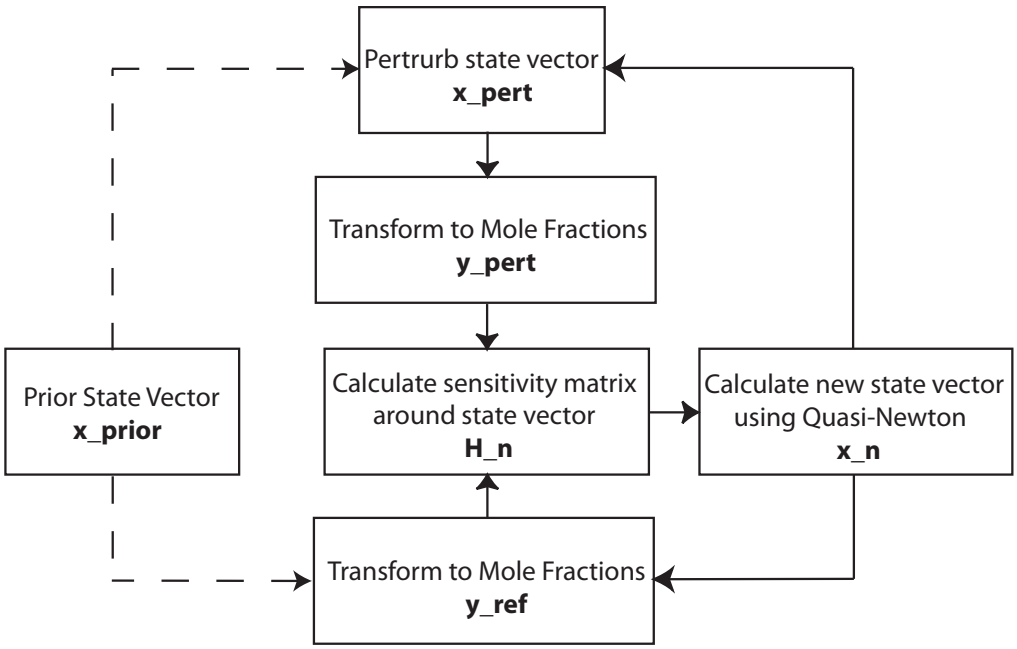

Figure 5-4: Flow diagram of the Quasi-Newton method, showing the iterative calculations for computing local minima to the quadratic fits to the cost function at iteration n. The input to the method is shown with dashed lines.

where, μ is a parameter governing the size of each step. If μ is too small, the solution will take many iterations to converge and if too large, the true minimum may be missed. In practice, a value of unity is used because the Hessian already accounts for the local curvature. $\mathbf{x}$ has converged when the value of the cost function has

reached a minimum and has stabilized (Equation 5.1). This value corresponds to the maximum likelihood point, $\tilde{\mathbf{x}}$, assuming that nonlinearities in $\mathbf{H}$ are small around each local point. At the maximum likelihood point, the state error covariance matrix is estimated from a linearization of $\mathbf{H}$ around $\tilde{\mathbf{x}}$ (Equation 5.9).

$$\tilde{\mathbf{P}} = (\mathbf{H}|_{\tilde{\mathbf{x}}}{}^{T}\mathbf{R}^{-1}\mathbf{H}|_{\tilde{\mathbf{x}}} + \mathbf{P}^{-1})^{-1} \tag{5.9}$$

5.2.1 *A Priori* Information

Emissions

Equation 5.3 transforms the state vector into emissions by scaling the *a priori* emissions for each gas. A summary of the *a priori* emissions used and corresponding references can be found in Table 5.1. Figures 5-5 and 5-6 show the spatial distribution of emissions for the three gases.

A priori CH_4 emissions were used from the TransCom model inter-comparison study. This set of emissions is comprised of fluxes from natural wetlands, domestic and large-scale biomass burning and termites from the Goddard Institute for Space Sciences (GISS) database, rice paddies from Yan et al. [2009], ocean exchange from Lambert and Schmidt [1993], volcano emissions from Etiope and Milkov [2004], and anthropogenic emissions from the Emissions Database for Global Atmospheric Research (EDGAR) v4.0 [Patra et al., 2011]. Anthropogenic emissions source categories include agricultural waste, aviation, road and non-road transportation, fossil fuel, industrial processes, livestock, oil and gas production and waste. Emissions were scaled following Patra et al. [2011].

A priori N_2O emissions include natural and agricultural soil emissions from the Global Emissions Inventory Activity (GEIA), oceanic emissions from GEIA and anthropogenic emissions from EDGAR v4.2. Anthropogenic emissions source categories are manure management, agricultural waste burning, large-scale biomass burning, energy production, industrial processes, combustion, road and non-road transportation, oil production, indirect emissions from NO_x and NH_3, indirect emissions from agri-

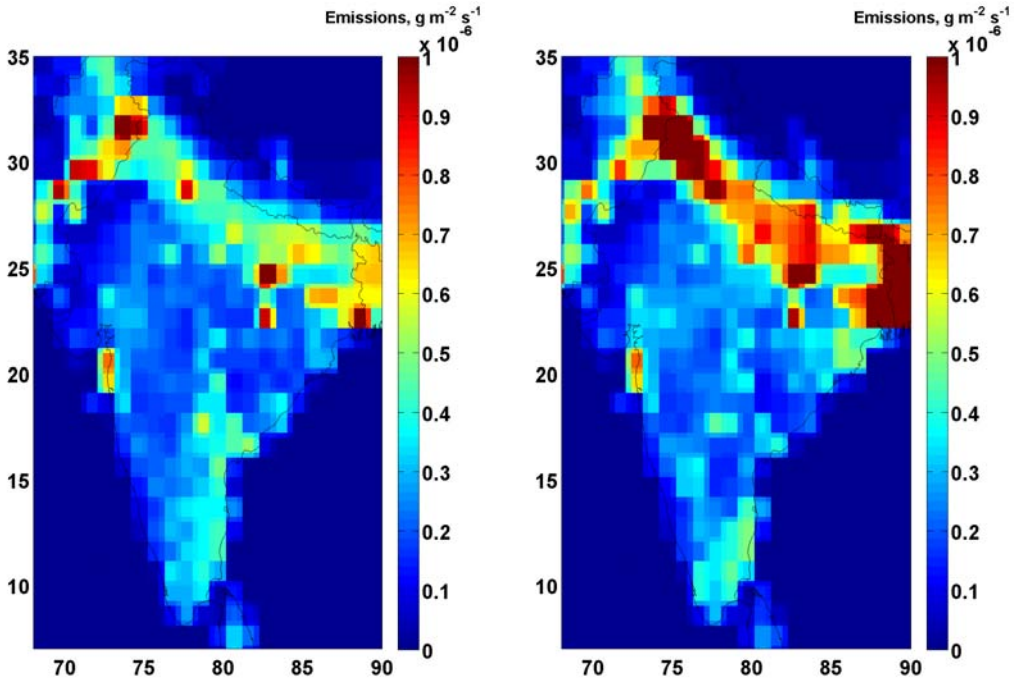

(a) (b)

Figure 5-5: *A priori* monthly CH_4 emissions (g m^{-2} s^{-1}) compiled from GISS, EDGAR v4.0, Yan et al. [2009], Lambert and Schmidt [1993] and Etiope and Milkov [2004] for (a) January and (b) July.

culture, and residential buildings.

A priori SF_6 emissions were compiled from anthropogenic, industrial source categories from EDGAR v4.2. Emissions sources mainly include the electronics and semiconductor industries.

The most recent year available (as shown in Table 5.1) was assumed for 2012 emissions and were interpolated to the grid resolution of the air histories (0.352°x0.254°) using mass conserving re-gridding routines created by Martin Schultz (MPI-Hamburg).

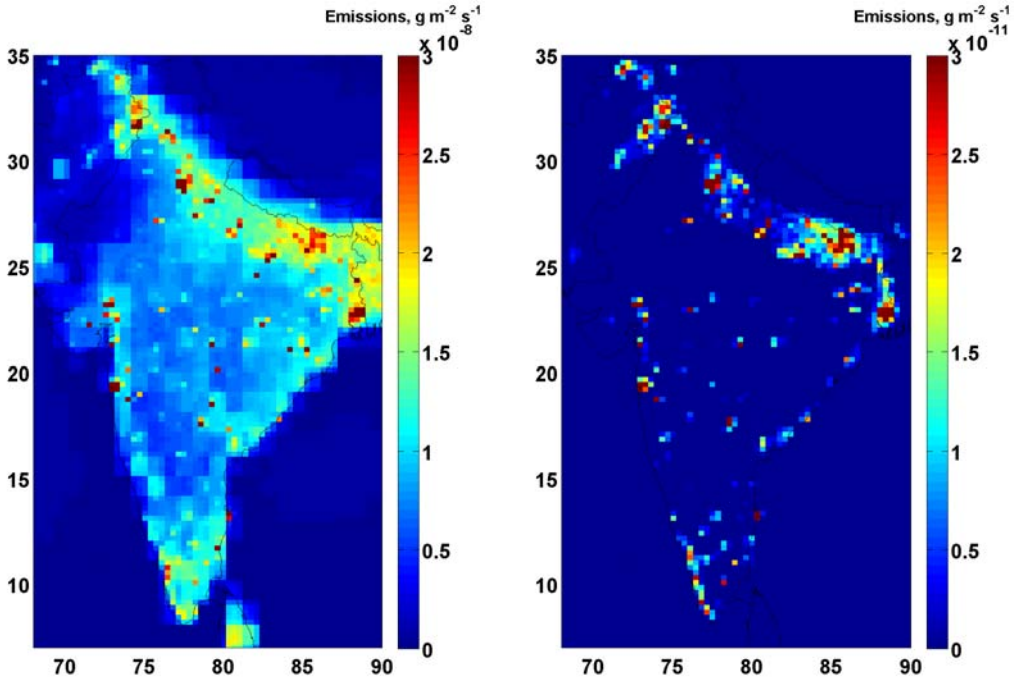

(a) (b)

Figure 5-6: *A priori* annual emissions (g m^{-2} s^{-1}) for (a) N_2O, compiled from GEIA and EDGAR v4.2. (b) SF_6, compiled from EDGAR v4.2 .

Table 5.1: Components and source categories of the CH_4, N_2O and SF_6 *a priori* emissions used in the inversions. Temporal resolution, inter-annual variability (IAV) and spatial resolution are specified.

Species	Database	Resolution (Year)	Source Categories
CH_4	GISS	Monthly, No IAV, 1°x1° (1987,1991)	Natural Wetland, Biomass Burning, Termites[a]
		Monthly, No IAV, 0.5°x0.5° (2000)	Rice Paddy[b]
	EDGAR v4.0	Annual, IAV, 1°x1° (2005)	Anthropogenic[c]
		Annual, No IAV, Uniform	Ocean Exchange[d]
		Annual, No IAV, Uniform	Volcano[e]
N_2O	GEIA	Annual, No IAV, 1°x1° (1990)	Natural and Agricultural Soil, Ocean[f]
	EDGAR v4.2	Annual, IAV, 0.1°x0.1° (2008)	Anthropogenic incl. biomass burning[g]
SF_6	EDGAR v4.2	Annual, IAV, 0.1°x0.1° (2008)	Anthropogenic[g]

[a]Fung et al. [1991]
[b]Yan et al. [2009]
[c]JRC/PBL [2009]
[d]Lambert and Schmidt [1993]
[e]Etiope and Milkov [2004]
[f]Bouwman et al. [1995]
[g]JRC/PBL [2011]

Beginning the first iteration in Equation 5.7, $\mathbf{x}_{prior}$ was zero for all scaling factor elements (resulting in emissions equal to the inventory values). Uncertainties on these scaling factor elements were normally distributed, resulting in a log-normal distribution on emissions. Standard deviations (1σ) on the scaling factor elements for CH_4 and N_2O were assumed to be one, translating to errors of +172% and -63% on emissions. Uncertainties on CH_4 and N_2O emissions are generally assumed to be on the order of 100% [Bergamaschi et al., 2009]. SF_6 emissions are thought to be better constrained than CH_4 and N_2O emissions and an uncertainty of 0.5 was used, translating to errors of +65% and -39%. Previous studies have used uncertainties of ±40% on EDGAR v4 emissions for SF_6 [Rigby et al., 2010]. For consistency, the maximum likelihood of the log-normal distribution is presented throughout.

Regions with small prior emissions will have smaller absolute uncertainties, which means that they will be more tightly fixed to the prior. This could be a greater source of error for gases such as SF_6 where emissions are point sources surrounded by areas of low emissions. If the location of the point source were incorrect or if new point sources have come online since the prior was compiled, the inversion would not be able to significantly alter those emissions.

Boundary Conditions

For all months except the summer months (for CH_4 and N_2O), Northern and Southern boundary condition elements were determined using AGAGE measurements from Mace Head, Ireland and Cape Matatula, American Samoa, which are the closest stations North and South of the domain. First, the mean mole fraction from 2012 was computed for each site. Polluted air was included to give a measure of the continental emissions North of the domain. A latitudinal gradient was then derived between these two stations and a mean boundary mole fraction was computed for the Northern and Southern boundaries based on this latitudinal gradient. Eastern and Western boundary conditions were based on Ragged Point, Barbados average 2012 mole fractions. Uncertainties for Northern and Southern boundaries were computed as the standard deviation in the 2012 mole fractions at each corresponding site. Uncertainties for the

Eastern and Western boundaries were the average of the Mace Head and Cape Matatula uncertainties. Since measurements from AGAGE stations were not additionally used in the inversion, there is no loss of independence by utilizing these measurements as the *a priori* boundary conditions.

During the summer, measurements from Cape Rama, India were used for the Western and Southern boundaries for CH_4 and N_2O, with an uncertainty on this value equal to the measurement uncertainty on the monthly mean [Bhattacharya et al., 2009, updated measurements courtesy of P. Krummel]. Cape Rama measurements were only available through July 2012, so the July monthly mean was assumed for the entire summer period. It is expected that the boundary conditions would be more accurately constrained during the summer when these measurements were utilized.

Table 5.2 and 5.3 contain mean and standard deviations of measurements from Mace Head and Cape Matatula stations and the *a priori* boundary conditions and uncertainties used in the inversion.

Table 5.2: Mean and standard deviation of 2012 mole fractions from Mace Head, Ireland and Cape Matatula, American Samoa AGAGE measurements.

Station	Location	Species	μ (nmol mol^{-1})	σ (nmol mol^{-1})
Mace Head, Ireland	53°N, 10°W	CH_4	1897	35.9
		N_2O	325.40	0.58
		SF_6	7.76 x 10^{-3}	0.12 x 10^{-3}
Cape Matatula, American Samoa	14°S, 171°W	CH_4	1771	9.3
		N_2O	324.71	0.37
		SF_6	7.42 x 10^{-3}	0.08 x 10^{-3}

5.2.2 Measurement Uncertainty

Measurements from Darjeeling were aggregated into daily values with the assumption that measurements at higher frequency would be correlated. It is therefore assumed

Table 5.3: *A priori* boundary conditions and uncertainties for each boundary by month. Values are based on latitudinal gradients derived from Mace Head, Ireland, Cape Matatula, American Samoa and Ragged Point, Barbados AGAGE measurements. (Cape Rama values were used for the Southern and Western boundaries during June-August for CH_4 and N_2O.)

Boundary	Species	μ (nmol mol^{-1})	σ (nmol mol^{-1})
Northern	CH_4	1893.5	35.9
	N_2O	325.38	0.58
	SF_6	7.75 x 10^{-3}	0.12 x 10^{-3}
Eastern	CH_4	1827.4	22.6
	N_2O	325.19	0.48
	SF_6	7.61 x 10^{-3}	0.10 x 10^{-3}
Southern	CH_4	1806.7 (1804)	9.3 (1.3)
	N_2O	324.96 (325.59)	0.37 (0.34)
	SF_6	7.42 x 10^{-3}	0.08 x 10^{-3}
Western	CH_4	1827.4 (1804)	22.6 (1.3)
	N_2O	325.19 (325.59)	0.48 (0.34)
	SF_6	7.61 x 10^{-3}	0.10 x 10^{-3}

that each daily value is an independent observation. Uncertainties on these measurements were assumed Gaussian and calculated using Equation 5.10 for n daily measurements. Equation 5.10 includes three terms: repeatability, scale propagation error and model representation error. Repeatability is a metric for establishing uncertainty on the instrument by determining the standard deviation of the standards measured each day. Scale propagation uncertainty is assumed to be equal to the repeatability uncertainty and is an instrumental uncertainty associated with the propagation of the tertiary standard from the primary standard. Model representation error is the uncertainty associated with how the model is able to represent the measurement station in the three-dimensional grid cell in which it is located. In previous stud-

ies, the model representation error has been calculated as the standard deviation of the variability in the averaging period (such as variability in a monthly mean), or the variability in the grid cells neighboring the site (in a Eulerian model) [Chen and Prinn, 2006, Rigby et al., 2011b]. It was calculated here as the uncertainty associated with a ±100 m error in particle release height, which represents errors in the vertical representation of the station. There is additionally a large error associated with meteorological resolution (as discussed in Section 3.2). This was not included in the model representation error because it assumes that the global NWP meteorology is of equal value as the high resolution meteorology and 'devalues' the benefit of using the high-resolution model. An alternative method that will be investigated in the future is to generate air history maps for a release point one grid cell away. These maps can be used to simulate mole fractions at the receptor. The difference in mole fractions generated from a release point one grid cell away can provide a means of assessing model representation of the grid cell. The largest term in Equation 5.10 for CH_4 is from the model representation error. Repeatability and model representation error are of approximately equal magnitude for N_2O. Errors due to repeatability and scale propagation error dominate for SF_6.

$$\sigma_n^2 = \left(\sigma_{repeatability}^2 + \sigma_{scaleprop}^2 + \sigma_{modelrep}^2\right) \tag{5.10}$$

5.3 Posterior Emissions Estimates and Uncertainties

Emissions were aggregated into national totals for India and Bangladesh using a Monte Carlo approach. Ten thousand random realizations of the optimized state vector, $\tilde{\mathbf{x}}$, were computed with a random Gaussian perturbation created by the Cholesky decomposition of the posterior error covariance matrix, $\tilde{\mathbf{P}}$. The Cholesky decomposition is the decomposition of a positive-definite matrix ($\tilde{\mathbf{P}}$) into the product of a lower triangular matrix and its conjugate transpose [Tarantola, 2005]. In essence, this decomposition provides the 'square-root' of the covariance matrix, while preserv-

ing correlations. Thus, each random realization has incorporated correlations from each element of the state vector, including correlations with the boundary conditions. The national totals for each country were computed as the sum of the state vector elements corresponding to each country for each random realization, resulting in a probability distribution of emission totals. Using this Monte Carlo approach, it was not necessary to first transform Gaussian errors on the scaling factor elements into log-normal errors on emissions, which could not easily be summed. Uncertainties on the national totals were taken as the 16th and 84th percentiles in the distributions (equivalent to 1σ of Normal distribution).

It should be noted that national total emissions computed through this Monte Carlo approach are often larger than the sum of the individual maximum likelihood values from each region. Furthermore, uncertainties on the distributions are smaller than the errors computed simply by transforming the uncertainties on scaling factors into emissions uncertainties, as a large fraction of the error on emissions from each region will cancel with other regions. For consistency, prior national emissions were computed using the same method with prior error covariance matrix $\mathbf{P}$ and state vector $\mathbf{x}_{prior}$ and so similar statistics are compared.

5.3.1 Reference Inversion

The reference inversion utilized air histories generated at a 500 magl release height using SAM meteorology for 7 days followed by the global NWP meteorological fields. Measurements have been averaged into daily values with no filtering for local emissions. Emissions and boundary conditions for the three gases were estimated monthly (excluding March, May and June when electrical problems resulted in significant measurement loss).

Figures 5-7, 5-9 and 5-12 show prior and posterior national totals for the three gases with errorbars corresponding to the 16th and 84th percentile values and are tabulated in Appendix B.

Optimized CH_4 Emissions

Posterior emissions are generally smaller than the prior with annual average (excluding December) Indian emissions of $44.3^{54.2}_{38.5}$ Tg yr^{-1}, on average 7 Tg yr^{-1} lower than the prior and average Bangladesh emissions of $4.2^{5.9}_{3.5}$ Tg yr^{-1}, approximately 2 Tg yr^{-1} less than the prior. These estimates are consistent with those derived by Patra et al. [2009], which showed 2009 emissions for India to be 41 Tg yr^{-1} and larger than the 20.5 Tg yr^{-1} reported by INCAA. Indian emissions maximize in August and minimize in February, consistent with the expected seasonal cycle in emissions. However, emissions derived for November are higher than expected but uncertainty reduction is small suggesting low sensitivity to India and little update from the prior. Negative spatial correlations up to 20% exist in emissions of several of the regions and are present every month. However, the effect of these correlations are minimized by presenting national totals.

Most of the uncertainty reduction in emissions from India and/or Bangladesh occur during the summer, when the monsoon driven flow results in high sensitivity over India. Very little uncertainty reduction is seen on Indian emissions during the winter, when sensitivity is limited to the Himalayan region. Almost all of the uncertainty reduction in the estimated boundary conditions are in the Western boundary, the dominant direction from which air enters the domain and to a lesser extent from the Eastern boundary during the winter.

Figure 5-8 shows the model-measurement comparison with shading corresponding to the measurement uncertainty along with total value of the boundary condition (sum of fractional components). The inversion simulates the overall monthly trend in emissions and is able to simulate most pollution events, though occasionally underestimates the size of these events. A large step is seen in the boundary conditions between January and February but overall shows lower values during the summer.

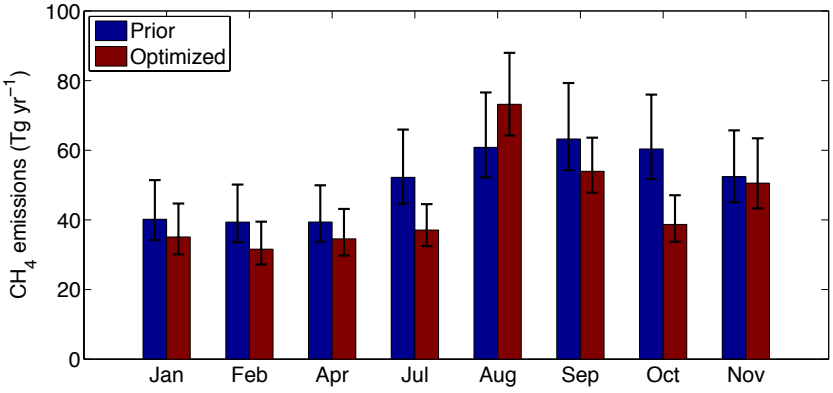

(a)

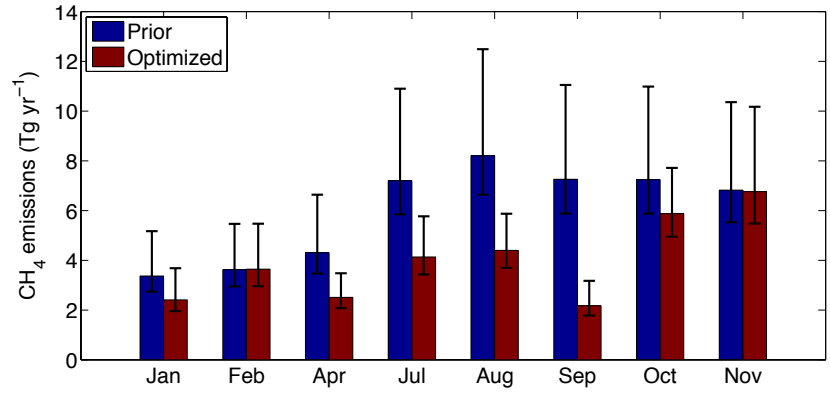

(b)

Figure 5-7: National prior (blue) and posterior (red) CH_4 emissions by month (Tg yr^{-1}) for (a) India and (b) Bangladesh.

Optimized N_2O Emissions

Posterior Indian N_2O emissions are statistically in agreement with the prior except for small decreases in September and October emissions (Figure 5-9). Emissions in all months are greater than those reported by INCAA. Similar to CH_4, the largest derived emissions are in August and November, suggesting similar conclusions that little update has been made to the prior in November. Even though constant annual emissions were assumed on the prior, a clearly defined seasonal cycle is not apparent in these monthly estimates, suggesting that the magnitude of the seasonal cycle lies within these uncertainties.

Uncertainty reduction is smaller on N_2O emissions than on CH_4 emissions because

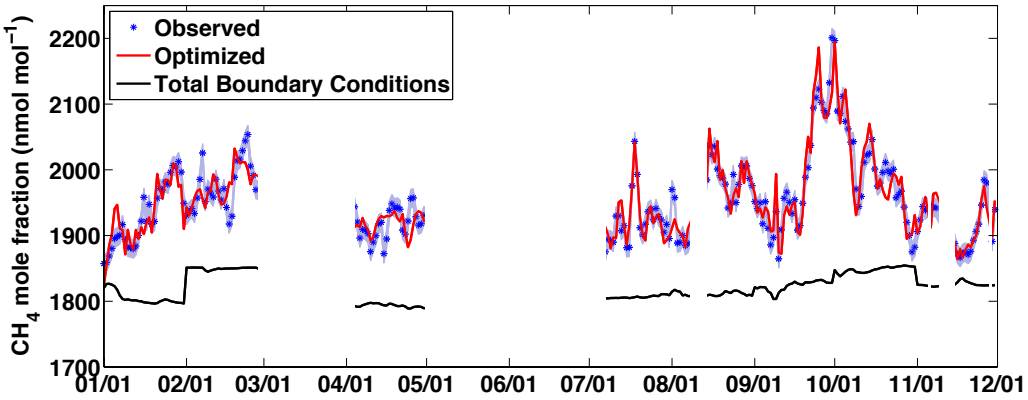

Figure 5-8: Optimized CH_4 daily mole fractions (red) and observations (blue) with shading corresponding to the 1σ measurement uncertainty.

measurement uncertainty is larger relative to the size of pollution events at Darjeeling. For N_2O, model representation error is approximately the same magnitude as the errors in repeatability and scale propagation. For comparison, emissions were derived using measurements with no model representation error and therefore reduced measurement uncertainty. Figure 5-10 shows these derived emissions and the largest reduction of uncertainty possible by assuming a perfect model. Indian emissions derived for November are higher than expected, suggesting either an underestimate of sensitivities or that 'local' emissions are contributing to the signal. Similar to the other gases, the majority of error reduction in the estimated boundary conditions are in the Western boundary, the direction from which the majority of air enters the domain. Correlations are generally smaller in N_2O than in CH_4 and for most months are only a few percent.

Model-measurement comparison is shown along with total value of the boundary condition in Figure 5-11. The model is generally able to capture most pollution events and captures the overall monthly trends but occasionally underestimates the size of signals (e.g., April mole fractions). A step change is seen in the boundary conditions between October and November and a large decrease is seen in September when air moves quickly from the southwest to the southeast.

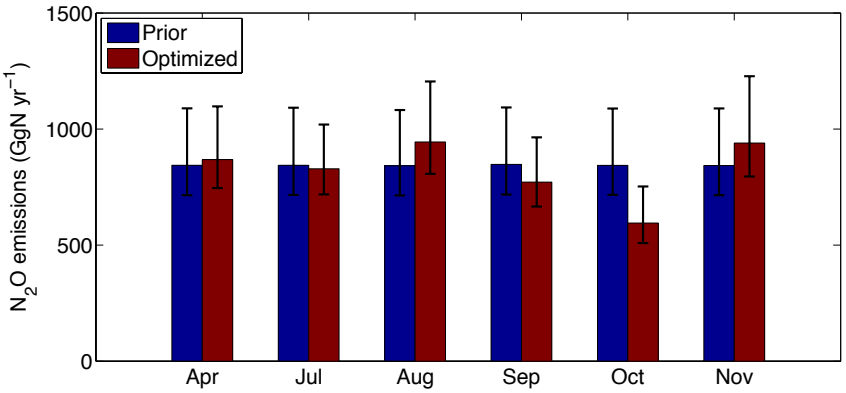

(a)

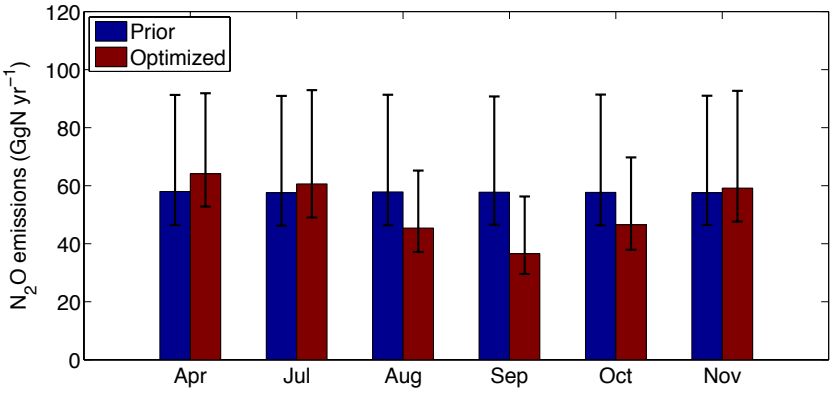

(b)

Figure 5-9: National prior (blue) and posterior (red) N_2O emissions by month (GgN yr^{-1}) for (a) India and (b) Bangladesh.

Optimized SF_6 Emissions

SF_6 measurements from Darjeeling most often are smoothly varying, reflecting the general Northern Hemispheric background signal. Occasionally, pollution events are sampled but this occurs infrequently. Figure 5-12 shows prior and posterior SF_6 emissions for India by month (Bangladesh emissions were not included since emissions are very low). Posterior emissions are consistent with the prior for most months but show a small statistically significant decrease in July, September and October. Similar to the other gases, November emissions are high, likely resulting from local influence or errors in the air history maps. SF_6 measurement uncertainty is dominated by the errors induced by repeatability and scale propagation. These errors are large compared

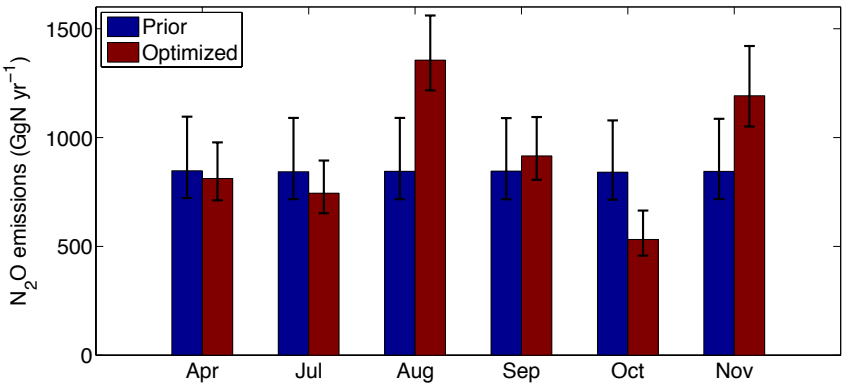

(a)

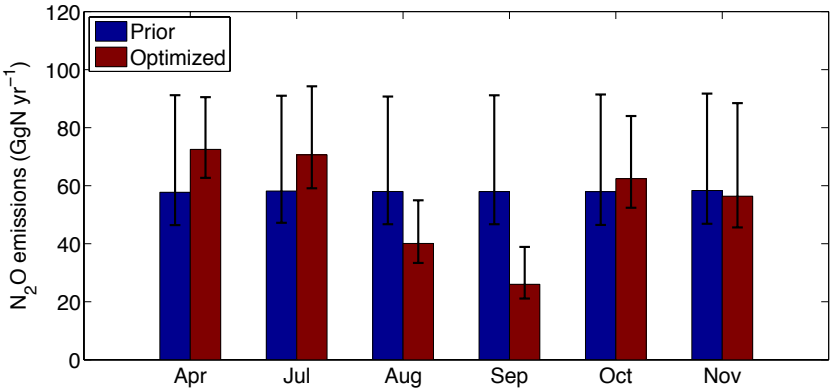

(b)

Figure 5-10: National prior (blue) and posterior (red) N_2O emissions by month (GgN yr^{-1}) for (a) India and (b) Bangladesh derived from measurements that do not contain model representation error.

to the size of pollution episodes at Darjeeling, resulting in small uncertainty reduction on emissions. Additionally, as with CH_4 and N_2O, the majority of uncertainty reduction occurs on the Western boundary condition. Regional correlations in SF_6 emissions are negligible.

While the model is able to capture many pollution signals, several pollution episodes are not captured. A model-measurement comparison along with total value of the boundary condition is shown in Figure 5-13. Furthermore, the model predicts variability that is often within the measurement uncertainty, thus limiting the ability of the inversion to reduce uncertainty on emissions. The largest model-measurement

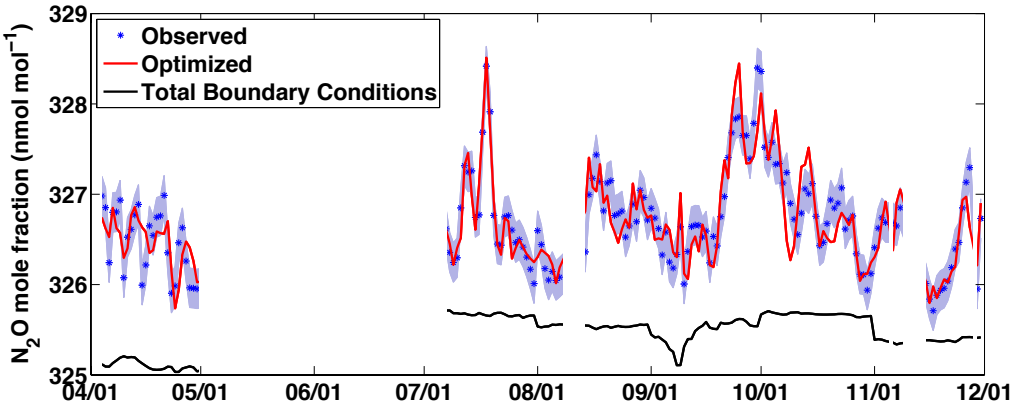

Figure 5-11: Optimized N_2O daily mole fractions (red) and observations (blue) with shading corresponding to the 1σ measurement uncertainty.

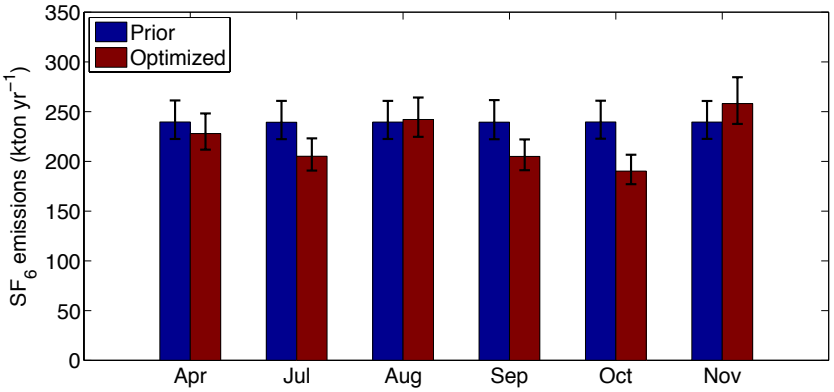

Figure 5-12: Indian prior (blue) and posterior (red) SF_6 emissions by month (kton yr^{-1}).

residuals occur in April, when the overall trend is not well-captured and this is consistent with simulated mole fractions for the other gases. The November pollution event is poorly captured and this signal is largely underestimated. The boundary conditions generally follow the same trend as the mole fractions, reflecting a similar growth rate.

In general, SF_6 residuals are larger than in CH_4 and N_2O. This may result from the fact that SF_6 emissions are from point-sources rather than with the broad distributions of CH_4 and N_2O and many grid cells in the *a priori* emissions do not contain emissions. One problem with the inverse method used is that emissions cannot be

scaled from regions that have zero emissions. If there are new point sources that were not available in the 2008 EDGAR v4.2 fields or if the distributions are slightly incorrect, the model will have to adjust the nearest available region with nonzero emissions and could lead to greater model-measurement residuals. This is difficult to improve without using a strictly Gaussian inversion scheme. To allow the model more flexibility to adjust emissions in low emissions regions, a minimum absolute uncertainty could be used.

Furthermore, SF_6 emissions are more tightly constrained to the prior than CH_4 or N_2O. A preliminary investigation using a larger prior uncertainty results in smaller residuals but in unrealistically high emissions in November (over 1200 kton yr^{-1}), suggesting errors in the derived air history maps at this time or that the local emissions are contributing to the pollution event (Figure 5-14).

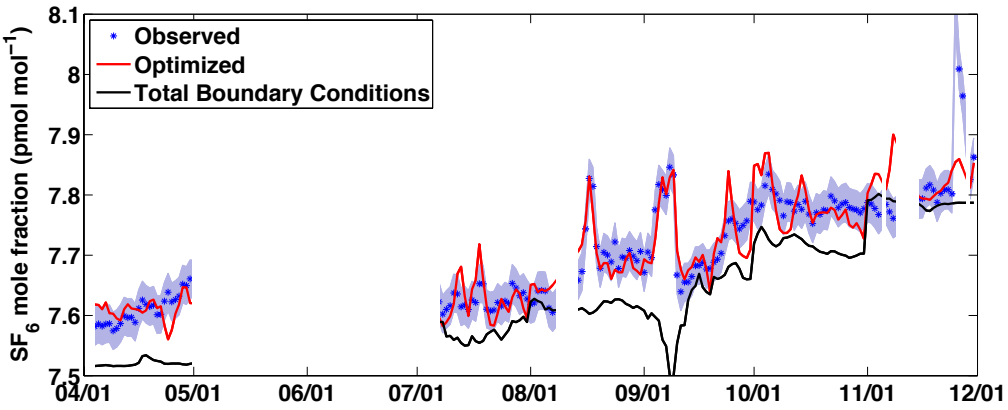

Figure 5-13: Optimized SF_6 daily mole fractions (red) and observations (blue) with shading corresponding to the 1σ measurement uncertainty.

Discussion

Inversions of the three gases suggest several important conclusions. More measurements (ideally from additional stations) or better constraints on model representation error to reduce overall measurement uncertainty (as in Equation 5.10) would allow for greater uncertainty reduction on emissions. These results show that the majority of uncertainty reduction occurs on the boundary conditions for N_2O and SF_6, for

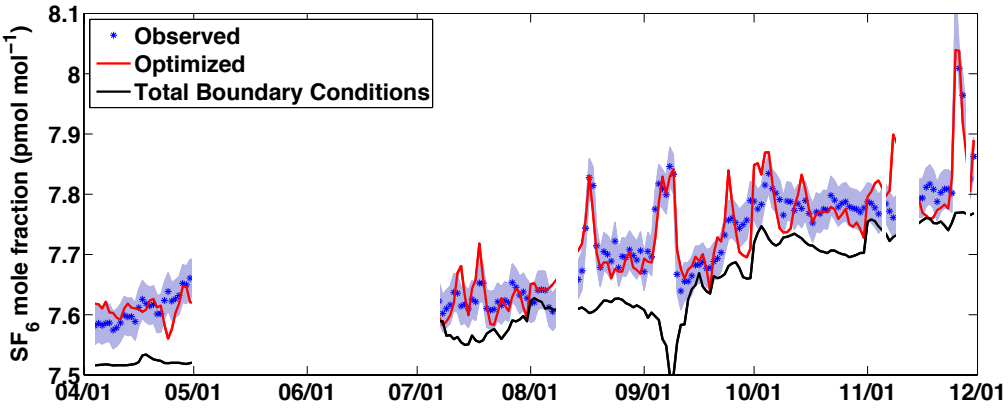

Figure 5-14: Optimized SF_6 daily mole fractions (red) and observations (blue) with shading corresponding to the 1σ measurement uncertainty. Emissions are derived with a prior uncertainty on scaling factor elements of 1.

which the measurement uncertainty is large relative to the magnitude of pollution events. A demonstration of uncertainty reduction was shown for N_2O for the case where model representation was assumed zero. In this example, a noticeable gain in uncertainty reduction was achieved. SF_6, on the other hand, has measurement uncertainty dominated by repeatability and scale propagation error. Because Darjeeling mostly samples the background signal, only small uncertainty reduction is achieved on emissions and this is limited by the magnitude of signals measured at the station. In contrast, CH_4 exhibits large pollution events, allowing for the inversion to better constrain emissions. Greater uncertainty reduction on boundary conditions over emissions occurs because every measurement provides information on boundary conditions, while only a fraction of measurements provides constraints on emissions from each region. Because of measurement uncertainty, there is flexibility for the model to scale mole fractions by refining boundary conditions (with a large measurement uncertainty, this flexibility becomes greater).

Application of this method toward gases with point source distributions could result in errors if the *a priori* distribution is incorrect. The inversion would have to compensate for the inability to adjust emissions in areas with zero prior emissions by adjusting nearby regions. The alternate method that could be employed is to use a

standard least-squares inversion with Gaussian uncertainties on emissions (which are not constrained to be positive).

Temporal correlations, which are not explicitly included, could limit month-to-month predictability. A growth constraint will be implemented following Rigby et al. [2011a] to add temporal correlation between boundary conditions and emissions in order to prevent unrealistic changes from month-to-month. For example, small step changes occur in the boundary conditions each month. While this is an unavoidable feature of the methodology, implementing a growth rate constraint will prevent large unrealistic changes. Furthermore, this will allow information to be passed forwards and backwards through the inversion, rather than allowing each month to be treated in isolation.

The first top-down emissions estimates using high-frequency data from India show that CH_4 emissions are on average 7 Tg yr^{-1} smaller than the prior. N_2O and SF_6 emissions are generally consistent with the prior or show small decreases and this study provides the first validation of these inventories.

5.3.2 Data Filtering for Local Emissions

As local sources of CH_4 (and N_2O/SF_6 to a lesser degree) exist in Darjeeling, removal of measurements that contain significant local influence was investigated to determine their effect on derived emissions estimates. Emissions estimates were compared using measurements that are daily averages of the full dataset, nighttime (12-4 am), morning (6-10am) and afternoon (12-4 pm) measurements. Sensitivities were similarly averaged into daily nighttime, morning and afternoon air histories. Previous studies have used various methods for filtering data at mountain sites [Peters et al., 2010, Brooks et al., 2012]. The most common method is time-of-day filtering. It is believed that sampling of local emissions would be minimized at night, as air is more likely to have subsided from the free troposphere. However, errors in air histories are minimized during the afternoon when the boundary layer height is at its highest because free tropospheric circulation is better modeled due to smaller influence from unresolved surface effects. Additionally, data from the morning is used to quantify

the effect of the morning peak in mole fractions. It is believed this peak results from boundary layer ventilation, a process that is not adequately modeled in the Unified Model at the resolutions and/or particle release height used here. As a third case, meteorological observations from the site were used to filter data when wind speeds were less than 1 m s^{-1}, to avoid extremely stagnant conditions when local influence could be high. As an approximation, daily average daytime (9am-3pm) sensitivities were used for the wind speed criterion, as wind speeds greater than the threshold generally occur during this time. A more accurate analysis would weight sensitivities based on the number of measurements used at each time of day. Uncertainties for these four filtered data sets were calculated following the same method described in Section 5.2.2.

Figure 5-15 shows optimized emissions derived using the four modified CH_4 data sets (along with the reference). For most months, the effect of data filtering on estimated emissions lies within uncertainties. In July, there is a significant difference in the optimized emissions derived using data from the morning (6-10 am). As shown in Figure 4-13 and discussed in Section 4.1, July mole fractions peak in the early morning with the breakup of the boundary layer, a feature this is not well-captured in the model. When data from the morning is filtered out, resulting emissions estimates decrease. The morning peak in mole fractions is observed in all months to varying degrees (maximizing in summer) but generally does not impact derived emissions. There is a small difference in January and July emissions whether nighttime or afternoon data is used, leading to higher and lower emissions, respectively. If it is assumed that measurement of local emissions are minimized at night, this suggests that the model is slightly underestimating sensitivities at night or overestimating during the day, though these differences lie within uncertainties. With the exception of July, when the wind speed criterion includes measurements during the morning, there is no difference in emissions derived with the wind speed criterion and using the full dataset.

These results draw several conclusions: (1) morning data corresponding to the breakup of a stable nighttime boundary layer should always be filtered as this process

is not well-captured in the model; (2) emissions derived using nighttime or afternoon data are generally (with largest difference seen in the summer) not significantly different, confirming that the model is able to simulate diurnal transport variations; (3) the effect of local processes that occur outside of the morning hours are not substantial and do not significantly impact derived emissions.

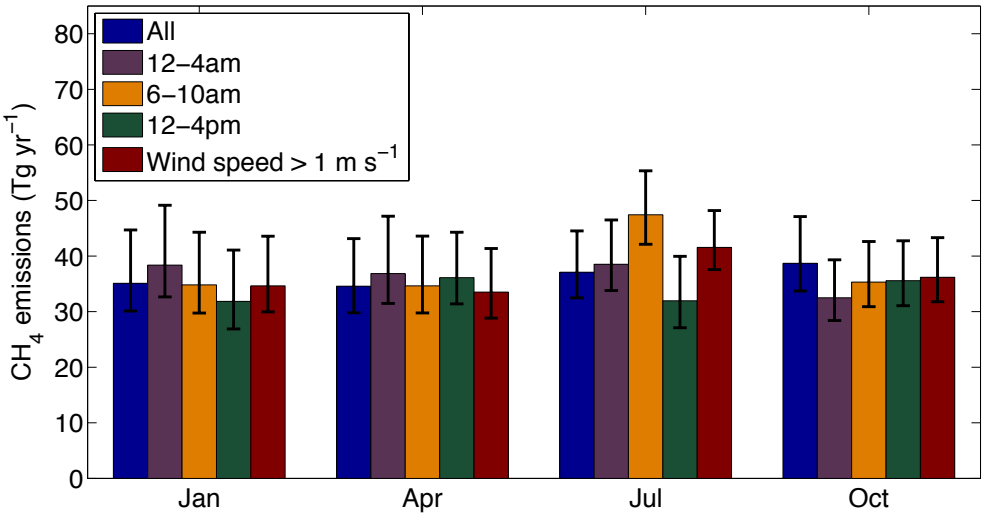

Figure 5-15: Effect of data filtering on Indian total CH_4 emissions derived using all data (reference, blue), 12-4am data (purple), 6-10am (orange), 12-4pm data (green) and data when wind speeds were greater than 1 m s^{-1} (red).

5.3.3 Sensitivity to Meteorological Resolution

The effect of meteorological resolution on simulated mole fractions was discussed in Section 3.2 but is discussed here in the context of emissions estimation. The sensitivity of resolution on derived emissions was investigated for January and July and is only discussed here for CH_4 for brevity.

Figure 5-16 shows aggregated national totals for India and Bangladesh for January and July under two scenarios and Figure 5-17 shows the distribution of emissions in each case. The first scenario uses SAM meteorology for 7-days followed by the global NWP meteorology and the second only uses the global NWP meteorology.

In January, aggregated total emissions for the two countries are in agreement and

there is only a small change in the distribution of emissions in Northern India. In July, the differences in national total emissions are significant, with a large increase seen in Indian emissions and large decrease in Bangladesh emissions when only global meteorology is used. This is reflected in the emissions maps, where greater emissions are seen in Northern India in the global scenario and greater emissions from Bangladesh in the SAM scenario (since Bangladesh is closer to Darjeeling than Northern India, fewer emissions are required to result in the same contribution to mole fractions at Darjeeling).

This suggests that resolution plays a greater role during certain seasons. During the summer, the monsoon-driven flow is very strong and results in transport of air masses from across the subcontinent. Furthermore, convection plays a significant role and is likely to be more accurately resolved at higher resolution. As a result, sensitivities are re-distributed from regions hundreds of kilometers apart using the two resolutions (e.g., Bangladesh and Northern India). In January when flows are more localized to the Himalayan region, resolution appears to have less of an impact and results in a more localized re-distribution. Though a large difference in mole fraction was simulated in January using the two resolutions and a prior emissions field (shown in Figure 3-4), the inversion redistributed emissions according to the differences in the derived air histories and most of this re-distribution remained close to the release point. This redistribution follows from the fact that using lower resolution meteorology tends to smooth out features but generally maintains the average signal.

5.3.4 Sensitivity to Particle Release Height

The effect of particle release height used to generate the air history maps was introduced in Section 3.3 and now is discussed for its effect on inversions for CH_4 emissions (Figure 5-18). Three scenarios were compared: the reference at 500 magl, and modified release heights of 400 and 600 magl. In both January and July, there is little effect on the aggregated total and any differences lie within the uncertainties. The effect of release height on simulated mole fractions using a prior emissions field was shown in Figures 3-8 and 3-9. Much larger changes were observed in July than January, which

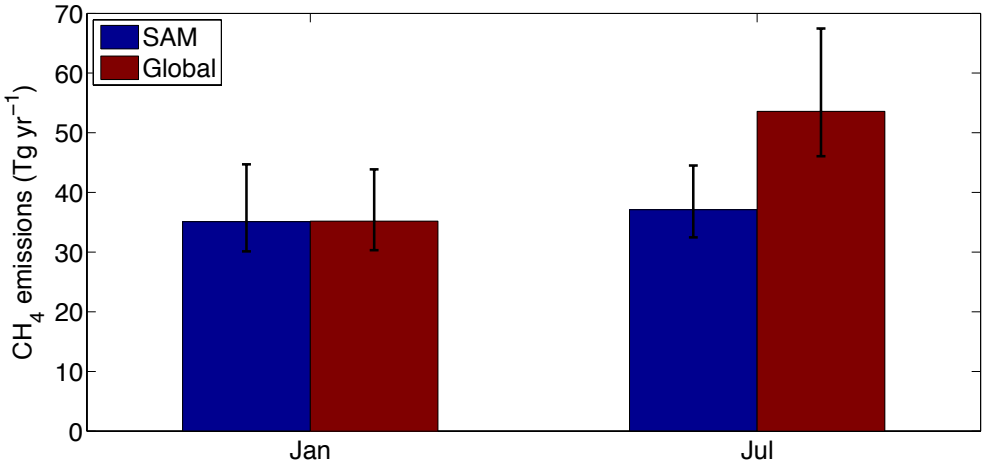

(a)

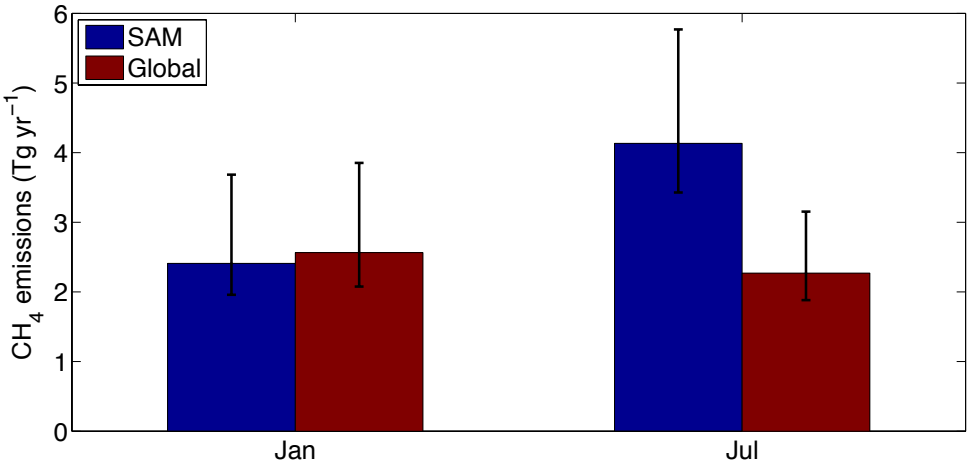

(b)

Figure 5-16: Effect of resolution on CH_4 emissions for January and July using the reference SAM meteorology (blue) and global meteorology (red) for (a) India (b) Bangladesh.

is consistent with the differences seen in the January and July emissions totals. The small differences in the July emissions confirms that the lower release height results in smaller emissions, as more particles are sensitive to the surface than those that originated above. Emissions maps shown in Figure 5-19 show that the effect of small changes in release height is to alter the magnitude of emissions and has little effect on the distribution. These tests provide validation that changes in particle release height

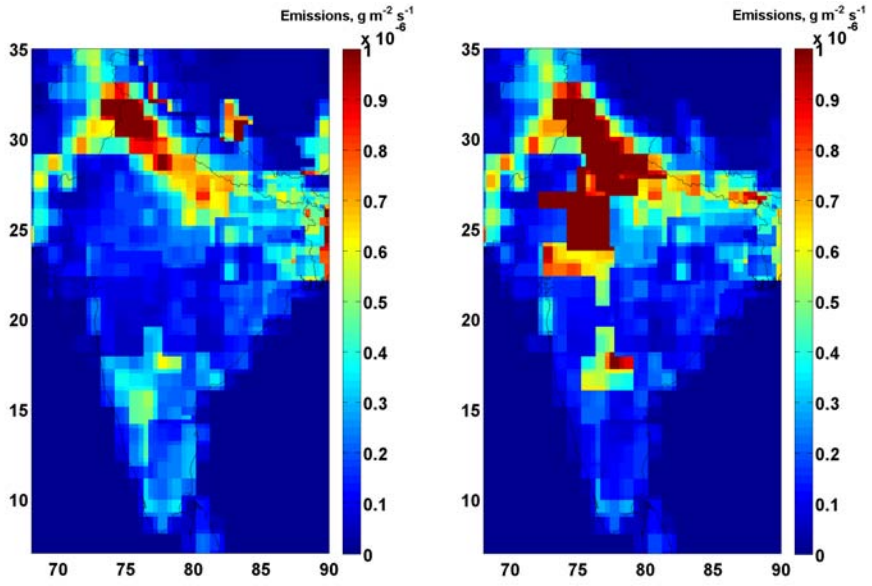

(a) (b)

Figure 5-17: Distribution of July CH_4 emissions (g m^{-2} s^{-1}) using (a) high-resolution SAM meteorology (b) low-resolution global model meteorology

within ±100m at the midpoint of model surface and true surface only has a small effect on the distribution of emissions and aggregated totals. This effect is larger in the summer than in winter when vertical transport is greater, though changes are still not statistically significant.

5.3.5 Unquantified Uncertainties

Several uncertainties or correlations have not been quantified in this study. Model uncertainties such as errors in the boundary layer scheme have not been determined, and is considered an important uncertainty, especially in mountain sites. This source of uncertainty could be investigated by determining sensitivities of meteorological fields to perturbations in the boundary layer formulation in the NWP model. Uncertainties in the NWP model could also be quantified by using different models. NAME is currently configured to also run the European Centre for Medium Range Weather Forecasting (ECMWF) reanalysis and could be configured to run others (e.g. NCEP). Choice of NWP could also be important for mountain sites, where slight perturba-

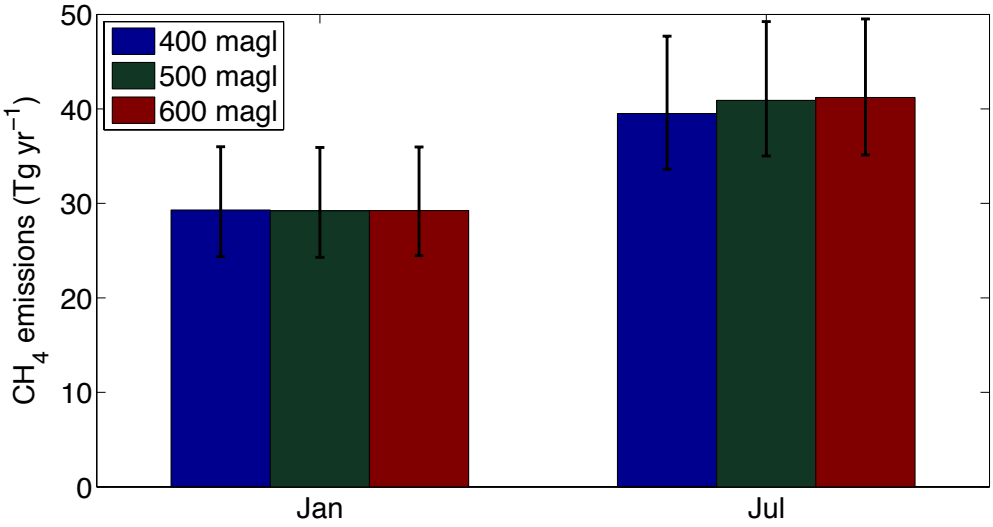

Figure 5-18: Effect of particle release height on Indian CH_4 emissions for January and July using 400 (blue), 500 (reference, green) and 600 (red) magl release heights.

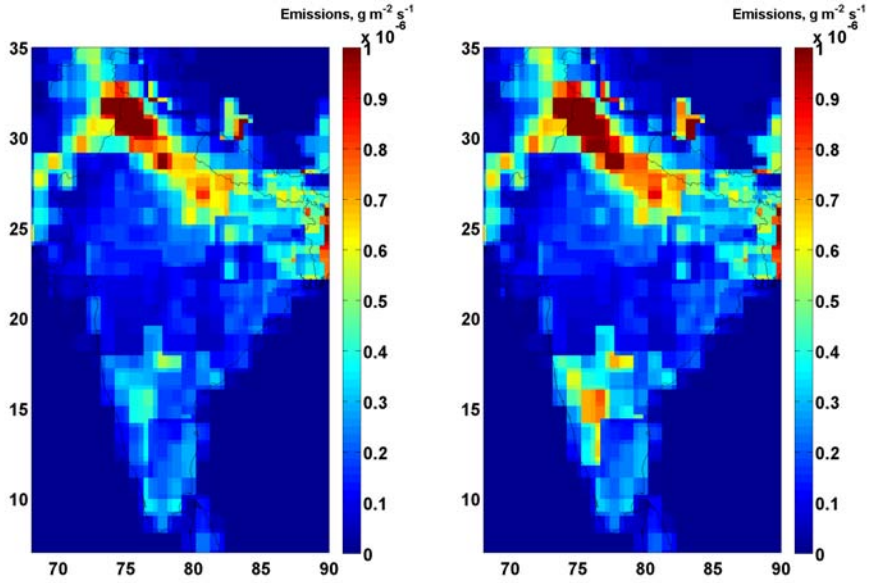

(a) (b)

Figure 5-19: Distribution of July CH_4 emissions maps (g m^{-2} s^{-1}) using (a) a 400 magl release height (b) a 600 magl release height

tions in model drivers could greatly impact flow in mountain terrain [Baker et al., 2006, Zhao et al., 2009].

Temporal and spatial aggregation errors are unquantified. Emissions and bound-

ary conditions were deduced at monthly resolution and therefore, any underlying structure would not be modeled. Similarly, spatial aggregation errors result from grid cells that were aggregated into larger regions [Kaminski et al., 2001, Thompson et al., 2011]. In principle, emissions could be determined at the three-hourly resolution of the measurements for each grid cell and aggregated into monthly and yearly emissions while properly accounting for covariance, but this is limited by computational resources.

Temporal correlations in the air history maps were not incorporated. For each measurement, air histories are created as integrated surface influence over the previous 30-days. When solving for monthly emissions, we assume that each measurement only informs the model about emissions from that month, when in actuality, the air histories contain information from the previous month as well. For example, a measurement on February 1 at midnight almost entirely contains information about January emissions, however, we assume that this measurement informs February emissions. One possible method to disaggregate temporal information in the air histories would be to track sensitivities for each three hour period in the 30-day backward simulation. This would provide additional temporal resolution in the air histories. Boundary conditions on February 1 would also be almost entirely dominated by the boundary conditions of January and this disaggregation should also be incorporated into the inversion. Furthermore, temporal correlations between monthly emissions and boundary conditions are not included.

Temporal correlations in the derived monthly emissions have been discussed. Each month is currently treated in isolation but information from other months should be used to inform month-to-month changes. A growth rate constraint on monthly emissions and boundary condition elements should be implemented to prevent large changes between months. Furthermore, temporal correlations should be incorporated in uncertainty analysis.

Uncertainties associated with choice of *a priori* emissions have not been quantified. For CH_4 and N_2O, several choices of inventories of emissions could have been used. For example, N_2O natural soil emissions generated by the Community Land Model

(personal communication, E. Saikawa, manuscript in preparation) show a substantial increase in Indian emissions from those generated by GEIA, which are used in this study. In future work, systematic biases resulting from the prior will be incorporated in uncertainty estimates.

Chapter 6

Conclusions

The main scientific objectives of this thesis were to collect the first *in situ* measurements from India of the powerful greenhouse gases, CH_4, N_2O and SF_6 and to utilize these measurements to deduce the South Asian emissions. A summary of the main findings are presented along with future developments to the project and long-term research directions that follow from this work.

6.1 Summary of Findings

The data collected in this thesis represent the first *in situ* measurements of the three gases from India and are a significant contribution to the sparse data that had previously been collected. The thesis also presents the first high-resolution emissions estimates for the three gases utilizing these *in situ* measurements.

Measurement of atmospheric CH_4, N_2O and SF_6 mole fractions were collected using a custom-built, automated instrument that allowed for high-precision *in situ* monitoring. The average repeatability of standards measured throughout the duration of this project was 0.07%, 0.05% and 0.40 % for each gas, respectively. The instrument was rigorously characterized prior to deployment. Non-linearities in the ECD were quantified and a correction was implemented to the data. The instrument was deployed to a new field site in Darjeeling, India in November 2011 with collaboration from the Bose Institute, Kolkata. Several site modifications were made to

the existing infrastructure to mainly improve power stability and the instrument has functioned well since deployment. No malfunctions have been reported in instrument function throughout the duration of the project. Details of the instrument design and testing are found in Chapter 2. Details of the field site and site characterization are found throughout Chapters 1, 2 and 3.

A Lagrangian Particle Dispersion Model developed by the UK Met Office known as NAME was used to simulate atmospheric transport to the measurement site. 'Air histories,' which contain the sensitivity of measured mole fractions at Darjeeling to a surface emissions field, were created every three hours for the duration of this study. The robustness of the model in simulating transport in the complex Himalayan terrain was investigated in Chapter 3. The roles of meteorological resolution and particle release height were introduced and investigated for their effect on simulations at Darjeeling. Meteorological observations from the site, including wind speed and wind direction, and the trace gas measurements were used to investigate the ability of the model to correctly capture transport. It was found that the model generally is able to capture large-scale transport events as well as mesoscale flows limited to the Himalayan region, which result in a seasonally-varying diurnal cycle in winds and in trace gas mole fractions. Furthermore, the model was able to reproduce many of the seasonal differences in this diurnal cycle.

Measurements of CH_4, N_2O and SF_6 are presented from January 2012 through November 2012 and is currently ongoing. Signals in the mole fractions of the three gases show emissions and transport processes of varying timescale that were discussed in Chapter 4. The dominant signal in SF_6 mole fractions was the slowly-varying signal characteristic of the Northern Hemisphere background. Occasional sampling of pollution events showed small enhancements in SF_6 mole fractions over the background, suggesting small emissions sources in the region. CH_4 and N_2O mole fractions, in contrast, were generally enhanced over the Northern Hemispheric background signal and were typically larger than the signals seen at stations even farther North, suggesting that strong regional sources were present that led to almost continuously elevated mole fractions. A diurnal cycle in these two gases was evident in the wintertime but

not present during the summer, which is consistent with the modeled and observed diurnal cycles in wind direction.

Top-down emissions estimates and sensitivity analyses were presented in Chapter 5. A Quasi-Newton method was employed to estimate emissions and boundary conditions at monthly resolution. CH_4 emissions from India were approximately $44.3^{54.2}_{38.5}$ Tg yr^{-1}, approximately 7 Tg yr^{-1} lower than the prior. Significant uncertainty reduction was seen on emissions from India and Bangladesh during the summer, when the monsoon-driven flow resulted in high sensitivity over India. N_2O and SF_6 emissions were generally consistent with the prior, with derived emissions of 825^{1045}_{707} GgN yr^{-1} and 221^{241}_{205} kton yr^{-1}, respectively. Larger measurement uncertainty for these gases, relative to the size of pollution events, led to smaller emissions uncertainty reductions than seen in CH_4. The roles of data filtering, meteorological resolution and particle height were presented as sensitivity studies. Resolution had the most significant impact on derived emissions during the summer, when emissions were redistributed to India from Bangladesh when air histories were generated using low resolution meteorology.

6.2 Ongoing Developments

Several modifications will be made to this work based on the conclusions of this thesis. Improvements to the quantification of model representation error will allow for more accurate constraints on measurement uncertainty. One possible method to more accurately ascertain model representation error will be to generate air history maps for a release point that is one grid cell away from Darjeeling and determine the difference in simulated mole fractions. This would provide an additional metric on station representation in the model to the one currently used that quantifies the sensitivity to particle release height.

Particle release height will be modified to include diurnal and seasonal differences to more accurately represent changes in station representation in the model. At night when surface air is very stable, the true observation point could be strongly

disconnected from air below and a release height closer to the true height could be used. During the day when there is strong vertical mixing, a release point at the model surface height could be used.

A growth rate constraint will be implemented following Rigby et al. [2011b] to constrain month-to-month changes in emissions and boundary conditions. Furthermore, this will allow information to be passed 'forwards' and 'backwards' through the inversion so that each month is not treated in isolation (temporal correlation within the air histories will have to be addressed separately and was discussed previously). This method could prevent large step changes in emissions and boundary conditions at each month and further would allow temporal correlations to be quantified. These temporal correlations can then be included in the final uncertainty analysis.

A Markov Chain Monte Carlo method will be investigated to determine the effect of the prior (by sampling from different probability distributions) on derived SF_6 emissions because SF_6 has a point-source distribution in which many grid cells do not contain any emissions and few have very large emissions in the *a priori* emissions field. This method will be compared with the quasi-Newton method used in this thesis.

6.3 Future Work

Several important avenues for long-term research follow from the work presented in this thesis. The most obvious area with need for significant expansion is in the number of stations monitoring these important greenhouse gases in India. Currently, the station in Darjeeling is the only operating station that is continuously monitoring concentrations of CH_4, N_2O and SF_6. More stations are required for greater uncertainty reduction on emissions estimates. The majority of uncertainty reduction in inversions results from regions that are within several hundred kilometers of the station. For a country the size of India, this requires many more dedicated stations. Furthermore, stations that sample 'boundary conditions' such as the Cape Rama measurements that were used as boundary conditions in this study are crucial for characterizing

regional pollution.

Isotopic information for CH_4 and N_2O would provide important constraints on source disaggregation. Measurement of the primary isotopologues of CH_4 ($^{13}CH_4$, CH_3D) and N_2O ($^{14}N^{15}N^{16}O$, $^{15}N^{14}N^{16}O$, $^{14}N^{14}N^{18}O$), which provide additional constraints on the sources of emissions due to the distinct source signatures of each emissions process (i.e., CH_4 emitted from microbial origins such as rice paddies are significantly more depleted in ^{13}C than CH_4 emitted from fossil fuels as shown in Figure 6-1) could be combined with the existing measurements to provide additional information about source apportionment [Rigby et al., 2012]. Measurements of CO and $^{14}CO_2$ could also provide additional constraints on fossil fuel emissions and could also be used to help identify local emissions.

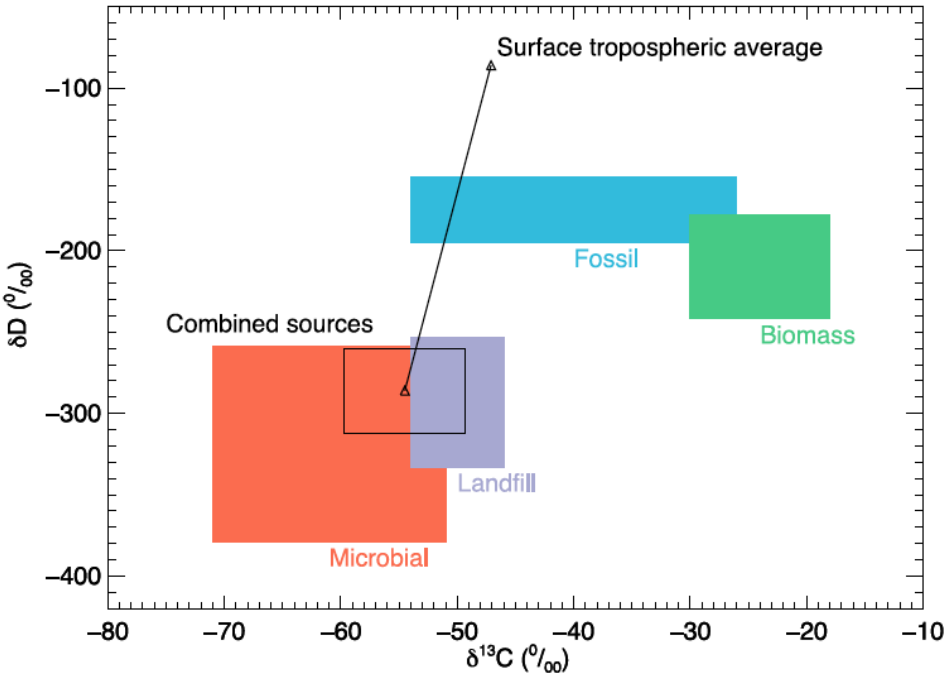

Figure 6-1: δ^{13} and δ^{D} signatures for four main emissions pathways for CH_4: microbial, landfill, fossil fuel and biomass burning. Figure from Rigby et al. [2012].

Quantification of structural uncertainty in NAME is required both to understand limitations of the model as well as to appropriately quantify the effects on derived emissions. These include (but are not limited to) a study of boundary layer representation, study of the convection scheme and even choice of NWP reanalysis data.

Boundary layer formulation is quite critical to the sensitivities derived by NAME as it can significantly impact simulated concentrations. With the obvious effect of changing concentrations within the boundary layer, it also significantly impacts the derived flows in the NWP model. The current convection scheme in NAME is quite simplistic, in that particles are randomly redistributed between a convective cloud base and cloud top. Parametrization of convection is often a significant element of modeling flow in the tropics, and is highly applicable to India. Choice of NWP model should be investigated to quantify the systematic biases associated with choice of meteorological drivers. While this is true for any inversion, it is more likely to have a significant influence at mountain sites.

Appendix A

Supplemental Experimental Material

Meteorological Measurements

Meteorological measurements were collected for air temperature, barometric pressure, wind speed and direction, solar radiation and precipitation using sensors that were implemented by the Bose Institute in 2010. Components of the meteorological station are listed in table A.1. These sensors were mounted five meters above the instrument inlet at the top of the tower as described in Chapter 2. The measurements used in this study were one minute averages of 10Hz data.

Table A.1: Components, make and model of the sensors used in the meteorological station at the Bose Institute, Darjeeling.

Component	Make	Model
Wind speed and direction monitor	Campbell Scientific	05103
Temperature and relative humidity probe	Campbell Scientific	HC-S3
Barometric pressure sensor	Campbell Scientific	61302V
Solar radiation	Campbell Scientific	SP LITE
Rain gauge	Campbell Scientific	TE525
Data logger	Campbell Scientific	CR1000

Table A.2: Instrument power requirements by component.

Component	Maximum consumption (W)	Nominal consumption (W)
Valves	180	12
Sample module fan	N/A	14
Sample module heater	150	75
Basic GC function	N/A	210
GC oven	1600	64
GC detectors	140	56
GC column oven	70	25
Gas purifiers	N/A	163
Air pump module	N/A	82
Pure air generator	N/A	800
Computer	N/A	225

Table A.3: Trace gas instrument components and manufacturers for major parts

Component	Make	Model	Location
Gas chromatograph	Agilent	6890N	Santa Clara, CA
Stream selector valve	Vici Valco	EMT2	Houston, TX
Two position valves	Vici Valco	ED2	Houston, TX
Micrometering valves	Vici Valco	ZBNV1-D	Houston, TX
Nafion dryer	Permapure	MD-050-72S-1	Toms River, NJ
$\frac{1}{16}$" - $\frac{1}{2}$" fittings	Swagelok	various	Billerica, MA
$\frac{1}{16}$" valve fittings	Vici Valco	EN1, ZF1	Houston, TX
$\frac{1}{16}$" - $\frac{1}{8}$" tubing	Vici Valco	TSS285	Houston, TX
$\frac{1}{4}$" tubing	Swagelok	SS-T4-S-035	Billerica, MA
$\frac{1}{8}$" copper tubing	Restek	21590	Bellefonte, PA
Uninterruptible Power Supply	Falcon Electric	SG Series 5kVA	Irwindale, CA
Two-stage standard gas regulator	Air Liquide Specialty Gases	Model 14	Houston, TX
Single stage carrier gas regulators	Air Gas	Y11 T265SC	Salem, NH
Heated gas purifier	Supelco	23800-U	St. Louis, MO
Moisture S trap	Agilent	5060-9077	Santa Clara, CA
Standard cylinder	Scott Marrin	03S-150A-590B	Riverside, CA
Drift cylinders	Scott Marrin	03S-030A-590B	Riverside, CA
Pure air generator	Aadco	737-1A	Cleves, OH
Inlet line	Goodrich	Synflex Type 1300	Geneva, IL
Diaphragm pump	KNF Neuberger	UN86	Trenton, NJ
Aquarium-style pump	Gast Manufacturing	DDL8BS	Benton Harbor, MI
Back pressure regulator	Go Regulators	LB1-2A01ACE111	Spartanburg, SC
Solid state relay	Tyco Electronics Corporation	SSRT-240D25	Berwyn, PA
7-micron filter	Swagelok	SS-4FW-7	Billerica, MA

(a)

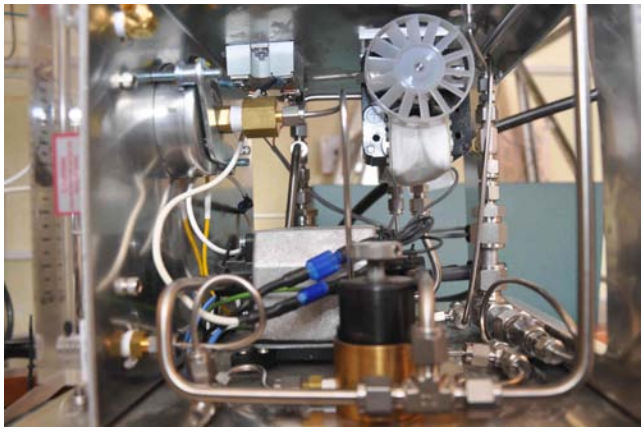

(b)

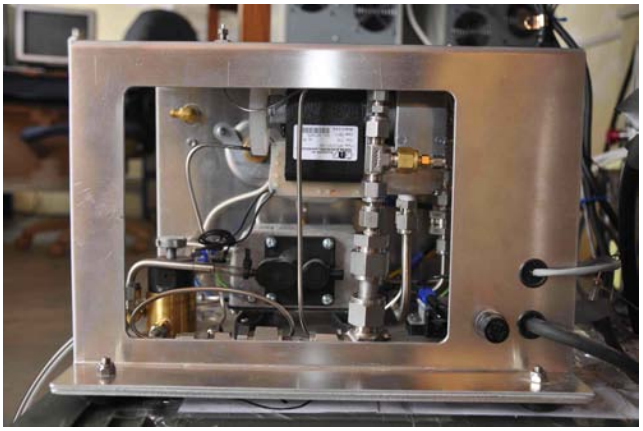

(c)

Figure A-1: (a) Water trap installed in the pump module to remove water droplets from the sample. (b,c) Images of the pump module.

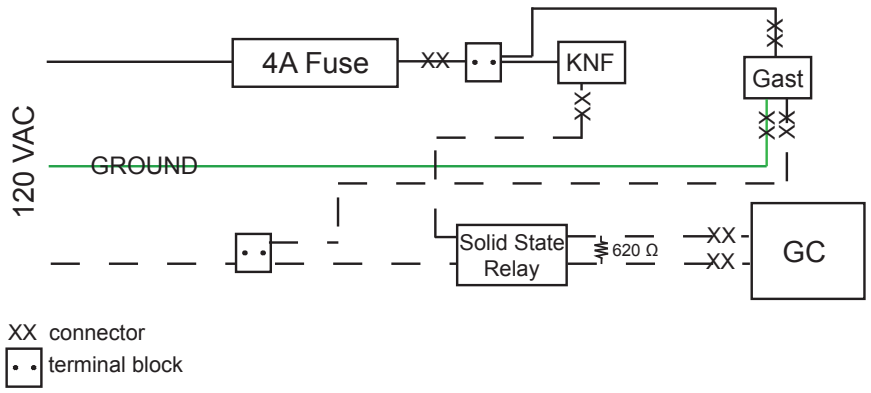

Figure A-2: Electrical wiring diagram of pump module.

Data Loss

Table A.4: Data loss between December 2011-December 2012

Date	Cause
December 2011 - March 2012	Delays in shipping ECD to India
February 27-March 25, 2012	Malfunctioning isolation transformer and low mains voltage
March 30 -April 4, 2012	Implementation of ECD
May 7 - June 14, 2012	Problem with company manufacturing carrier gases
June 24 - July 7, 2012	Malfunctioning isolation transformer and installment of new isolation transformer
August 7- August 13, 2012	Malfunctioning generator
November 4 - November 6, 2012	Problem with incoming electricity in Darjeeling and low voltage
November 9 - November 14, 2012	Continuing problems with incoming electricity in Darjeeling

Appendix B

Supplemental Inverse Modeling Material

Inversion Setup

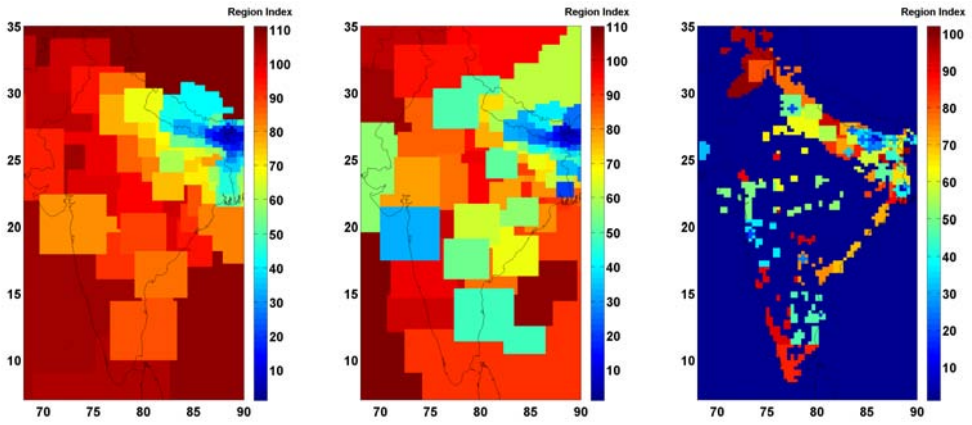

(a) (b) (c)

Figure B-1: Aggregated regions used in the inversion for (a) CH_4 (b) N_2O (c) SF_6, determined using the approach discussed in Chapter 5. Regions are based on the mean annual sensitivities and mean annual *a priori* emissions for each gas.

Reference Inversion

Tabulated Emissions and Boundary Conditions

Table B.1: National prior and optimized CH_4 emissions and uncertainties (Tg yr^{-1})

	Prior		Optimized	
	India	Bangladesh	India	Bangladesh
January	$40.2^{51.4}_{34.2}$	$3.4^{5.2}_{2.7}$	$35.1^{44.7}_{30.1}$	$2.4^{3.7}_{2.0}$
February	$39.4^{50.1}_{33.6}$	$3.6^{5.5}_{2.9}$	$31.6^{39.4}_{27.2}$	$3.6^{5.5}_{3.0}$
April	$39.4^{50.0}_{33.7}$	$4.3^{6.6}_{3.5}$	$34.5^{43.1}_{29.8}$	$2.5^{3.5}_{2.1}$
July	$52.2^{65.9}_{44.5}$	$7.2^{10.9}_{5.8}$	$37.1^{44.5}_{32.4}$	$4.1^{5.8}_{3.4}$
August	$60.8^{76.6}_{52.1}$	$8.2^{12.5}_{6.6}$	$73.2^{88.0}_{64.2}$	$4.4^{5.9}_{3.7}$
September	$63.2^{79.3}_{54.2}$	$7.3^{11.0}_{5.9}$	$54.0^{63.6}_{47.8}$	$2.2^{3.2}_{1.8}$
October	$60.4^{76.0}_{51.7}$	$7.2^{11.0}_{5.9}$	$38.7^{47.1}_{33.7}$	$5.9^{7.7}_{4.9}$
November	$34.0^{41.5}_{28.5}$	$4.7^{6.6}_{3.5}$	$38.3^{46.5}_{32.1}$	$4.8^{6.7}_{3.6}$

Table B.2: National prior and optimized N_2O emissions and uncertainties (GgN yr^{-1})

	Prior		Optimized	
	India	Bangladesh	India	Bangladesh
April	844^{1089}_{715}	58^{91}_{46}	869^{1098}_{746}	64^{92}_{53}
July	844^{1089}_{715}	58^{91}_{46}	829^{1019}_{718}	61^{93}_{49}
August	844^{1089}_{715}	58^{91}_{46}	944^{1205}_{807}	45^{65}_{37}
September	844^{1089}_{715}	58^{91}_{46}	771^{964}_{666}	37^{56}_{30}
October	844^{1089}_{715}	58^{91}_{46}	595^{753}_{509}	47^{70}_{38}
November	844^{1089}_{715}	58^{91}_{46}	940^{1228}_{796}	59^{93}_{48}

Table B.3: Indian prior and optimized SF_6 emissions and uncertainties (kton yr^{-1}). Emissions from Bangladesh are less than 1 kton yr^{-1} and have been omitted.

	Prior	Optimized
April	240^{261}_{222}	228^{248}_{212}
July	240^{261}_{222}	205^{223}_{191}
August	240^{261}_{222}	242^{264}_{225}
September	240^{261}_{222}	205^{222}_{191}
October	240^{261}_{222}	190^{207}_{177}
November	240^{261}_{222}	240^{262}_{223}

Table B.4: Optimized CH_4 boundary conditions and uncertainties in nmol mol^{-1}

	North	East	South	West
January	1911.7 (35.2)	1878.9 (21.5)	1819.4 (9.1)	1795.4 (8.5)
February	1849.0 (35.3)	1826.7 (22.6)	1804.5 (9.3)	1851.3 (10.9)
April	1863.6 (34.5)	1828.1 (22.5)	1813.8 (8.9)	1784.4 (13.4)
July	1861.2 (34.8)	1827.6 (22.6)	1804.2 (1.3)	1803.6 (1.3)
August	1898.4 (33.9)	1805.0 (21.1)	1804.2 (1.3)	1804.2 (1.3)
September	1875.4 (35.4)	1776.9 (20.1)	1811.9 (8.4)	1839.6 (12.1)
October	1876.2 (35.5)	1846.3 (21.8)	1822.9 (8.6)	1853.5 (11.6)
November	1897.5 (35.6)	1840.3 (22.0)	1808.0 (9.2)	1820.0 (9.3)

Table B.5: Optimized N_2O boundary conditions and uncertainties in nmol mol^{-1}

	North	East	South	West
April	325.31 (0.56)	325.31 (0.48)	325.58 (0.26)	324.95 (0.17)
July	325.28 (0.57)	325.32 (0.48)	325.57 (0.22)	325.57 (0.16)
August	325.27 (0.56)	325.16 (0.40)	325.71 (0.23)	325.81 (0.21)
September	325.31 (0.57)	325.67 (0.39)	325.31 (0.20)	325.76 (0.18)
October	325.12 (0.57)	325.63 (0.44)	325.76 (0.23)	325.67 (0.14)
November	325.30 (0.57)	325.84 (0.44)	325.20 (0.32)	325.92 (0.10)

Table B.6: Optimized Indian SF_6 boundary conditions and uncertainties in pmol mol^{-1}.

	North	East	South	West
April	7.63 (0.11)	7.63 (0.10)	7.52(0.04)	7.53 (0.02)
July	7.76 (0.12)	7.66 (0.10)	7.69 (0.03)	7.52 (0.01)
August	7.74 (0.11)	7.58 (0.07)	7.61(0.03)	7.61 (0.03)
September	7.74 (0.11)	7.25 (0.06)	7.52(0.02)	7.77 (0.02)
October	7.54 (0.12)	7.74 (0.09)	7.83 (0.04)	7.67 (0.01)
November	7.74 (0.12)	8.00 (0.09)	7.57 (0.07)	7.82 (0.01)

Bibliography

D. F. Baker, R. M. Law, K. R. Gurney, P. Rayner, P. Peylin, A. S. Denning, P. Bousquet, L. Bruhwiler, Y.-H. Chen, P. Ciais, I. Y. Fung, M. Heimann, J. John, T. Maki, S. Maksyutov, K. Masarie, M. Prather, B. Pak, S. Taguchi, and Z. Zhu. TransCom 3 inversion intercomparison: Impact of transport model errors on the interannual variability of regional CO_2 fluxes, 19882003. *Global Biogeochemical Cycles*, 20(1), 2006.

P. Bergamaschi, C. Frankenberg, J.F. Meirink, M. Krol, M.G. Villani, S. Houweling, F. Dentener, E.J. Dlugokencky, J.B. Miller, L.V. Gatti, A. Engel, and I. Levin. Inverse modeling of global and regional CH_4 emissions using SCIAMACHY satellite retrievals. *Journal of Geophysical Research*, 114(D22):1–28, 2009.

S.K. Bhattacharya, D.V. Borole, R.J. Francey, C.E. Allison, L.P. Steele, P. Krummel, R. Langenfelds, K. A. Masarie, Y.K. Tiwari, and P. K. Patra. Trace gases and CO_2 isotope records from Cabo de Rama, India. *Current Science*, 97(9):1336–1344, 2009.

P. Bousquet, P. Ciais, J.B. Miller, E.J. Dlugokencky, D.A. Hauglustaine, C. Prigent, G.R. Van der Werf, P. Peylin, E.G. Brunke, C. Carouge, R. L. Langenfelds, J. Lathière, F. Papa, M. Ramonet, M. Schmidt, L. P. Steele, S.C. Tyler, and J. White. Contribution of anthropogenic and natural sources to atmospheric methane variability. *Nature*, 443(7110):439–443, 2006.

P. Bousquet, B. Ringeval, I. Pison, E. J. Dlugokencky, E.-G. Brunke, C. Carouge, F. Chevallier, A. Fortems-Cheiney, C. Frankenberg, D. A. Hauglustaine, P. B. Krummel, R. L. Langenfelds, M. Ramonet, M. Schmidt, L. P. Steele, S. Szopa, C. Yver, N. Viovy, and P. Ciais. Source attribution of the changes in atmospheric methane for 20062008. *Atmospheric Chemistry and Physics*, 11(8):3689–3700, 2011.

A. F. Bouwman, K. W. Van der Hoek, and J. G. J. Olivier. Uncertainties in the global source distribution of nitrous oxide. *Journal of Geophysical Research*, 100 (D2):2785–2800, 1995.

B.-G. J. Brooks, A. R. Desai, B. B. Stephens, D. R. Bowling, S. P. Burns, A. S. Watt, S. L. Heck, and C. Sweeney. Assessing filtering of mountaintop CO_2 mole fractions for application to inverse models of biosphere-atmosphere carbon exchange. *Atmospheric Chemistry and Physics*, 12(4):2099–2115, 2012.

D. Brunner, S. Henne, C. A. Keller, S. Reimann, M. K. Vollmer, S. O'Doherty, and M. Maione. An extended Kalman-filter for regional scale inverse emission estimation. *Atmospheric Chemistry and Physics*, 12(7):3455–3478, 2012.

A. Chatterjee, A. Adak, A.K. Singh, M.K. Srivastava, S.K. Ghosh, S. Tiwari, P.C.S. Devara, and S. Raha. Aerosol chemistry over a high altitude station at northeastern Himalayas, India. *PloS one*, 5(6):1–20, 2010.

Y.-H. Chen and R.G. Prinn. Atmospheric modeling of high- and low-frequency methane observations: Importance of interannually varying transport. *Journal of Geophysical Research*, 110(D10):1–27, 2005.

Y.-H. Chen and R.G. Prinn. Estimation of atmospheric methane emissions between 1996 and 2001 using a three-dimensional global chemical transport model. *Journal of Geophysical Research*, 111(D10):1–25, 2006.

D. M. Cunnold, L. P. Steele, P.J. Fraser, P.G. Simmonds, R.G. Prinn, R.F. Weiss, L. W. Porter, S.J. ODoherty, R. L. Langenfelds, P. B. Krummel, R.H.J Wang, L. K. Emmons, X.X. Tie, and E.J. Dlugokencky. In situ measurements of atmospheric methane at GAGE/AGAGE sites during 19852000 and resulting source inferences. *Journal of Geophysical Research*, 107(D14):1–20, 2002.

D.A. Deeds, M.K. Vollmer, J.T. Kulongoski, B.R. Miller, J. Mühle, C.M. Harth, J.A. Izbicki, D.R. Hilton, and R.F. Weiss. Evidence for crustal degassing of CF_4 and SF_6 in Mojave Desert groundwaters. *Geochimica et Cosmochimica Acta*, 72(4): 999–1013, 2008.

K.L. Denman, G. Brasseur, A. Chidthaisong, P. Ciais, P.M. Cox, R.E. Dickinson, D. Hauglustaine, C. Heinze, E. Holland, D. Jacob, U. Lohmann, S. Ramachandran, P.L. da Silva Dias, S.C. Wofsy, and X. Zhang. Couplings Between Changes in the Climate System and Biogeochemistry. *Climate Change 2007: The Physical Science Basis. Contribution of Working Group I to the Fourth Assessment Report of the Intergovernmental Panel on Climate Change [Solomon, S., D. Qin, M. Manning, Z. Chen, M. Marquis, K.B. Averyt, M.Tignor and H.L. Miller (eds.)] Cambridge University Press, Cambridge, United Kingdom and New York, NY, USA.*, 2007.

E. J. Dlugokencky, L. Bruhwiler, J. W. C. White, L. K. Emmons, P. C. Novelli, S. A. Montzka, K. A. Masarie, P. M. Lang, A. M. Crotwell, J. B. Miller, and L. V. Gatti. Observational constraints on recent increases in the atmospheric CH_4 burden. *Geophysical Research Letters*, 36(18):1–5, 2009.

E. J. Dlugokencky, R.C. Myers, P.M. Lang, K.A. Masarie, A.M. Crotwell, K.W. Thoning, B. D. Hall, J. W. Elkins, and L.P. Steele. Conversion of NOAA atmospheric dry air CH_4 mole fractions to a gravimetrically prepared standard scale. *Journal of Geophysical Research*, 110(D18):1–8, 2005.

G. Etiope and A.V. Milkov. A new estimate of global methane flux from onshore and shallow submarine mud volcanoes to the atmosphere. *Environmental Geology*, 46 (8):997–1002, 2004.

P. Forster, V. Ramaswamy, P. Artaxo, T. Berntsen, R. Betts, D.W. Fahey, J. Haywood, J. Lean, D.C. Lowe, G. Myhre, J. Nganga, R. Prinn, G. Raga, M. Schulz, and R. Van Dorland. Changes in atmospheric constituents and in radiative forcing. *Climate Change 2007: The Physical Science Basis. Contribution of Working Group I to the Fourth Assessment Report of the Intergovernmental Panel on Climate Change [Solomon, S., D. Qin, M. Manning, Z. Chen, M. Marquis, K.B. Averyt, M.Tignor and H.L. Miller (eds.)] Cambridge University Press, Cambridge, United Kingdom and New York, NY, USA.*, 2007.

I. Fung, J. John, J. Lerner, E. Matthews, M. Prather, L. P. Steele, and P. J. Fraser. Three-dimensional model synthesis of the global methane cycle. *Journal of Geophysical Research*, 96(D7):13033–13065, 1991.

B. D. Hall, G. S. Dutton, and J. W. Elkins. The NOAA nitrous oxide standard scale for atmospheric observations. *Journal of Geophysical Research*, 112(D9):1–9, 2007.

B. D. Hall, G. S. Dutton, D. J. Mondeel, J. D. Nance, M. Rigby, J. H. Butler, F. L. Moore, D. F. Hurst, and J. W. Elkins. Improving measurements of SF_6 for the study of atmospheric transport and emissions. *Atmospheric Measurement Techniques*, 4 (11):2441–2451, 2011.

A. I. Hirsch, A. M. Michalak, L. M. Bruhwiler, W. Peters, E. J. Dlugokencky, and P. P. Tans. Inverse modeling estimates of the global nitrous oxide surface flux from 19982001. *Global Biogeochemical Cycles*, 20(1):1–17, 2006.

http://agage.eas.gatech.edu, 2013. accessed January 2013.

J. Huang, A. Golombek, R. Prinn, R. Weiss, P. Fraser, P. Simmonds, E. J. Dlugokencky, B. Hall, J. Elkins, P. Steele, R. Langenfelds, P. Krummel, G. Dutton, and L. Porter. Estimation of regional emissions of nitrous oxide from 1997 to 2005 using multinetwork measurements, a chemical transport model, and an inverse method. *Journal of Geophysical Research*, 113(D17):1–19, 2008.

Indian Network for Climate Change Assessment. India: Greenhouse Gas Emissions 2007. Technical report, Ministry of Environments and Forests, Government of India, 2007.

A.R. Jones, D. Thompson, M Hort, and B. Devenish. *The U.K. Met Office's Next-Generation Atmospheric Dispersion Model , NAME III.* Springer, New York, 2004.

JRC/PBL. Emission Database for Global Atmospheric Research (EDGAR), release version 4.0, 2009.

JRC/PBL. Emission Database for Global Atmospheric Research (EDGAR), release version 4.2, 2011.

E. Kalnay, M. Kanamitsu, R. Kistler, W. Collins, D. Deaven, L. Gandin, M. Iredell, S. Saha, G. White, J. Woollen, Y. Zhu, A. Leetmaa, and R. Reynolds. Atmospheric inverse estimates of methane emissions from Central California. *Bureau of the American Meteorological Society*, 77(3):437–471, 1996.

T. Kaminski, P.J. Rayner, M. Heimann, and I.G. Enting. On aggregation errors in atmospheric transport inversions. *Journal of Geophysical Research*, 106(D5):4703, 2001.

G. Lambert and S. Schmidt. Reevaluation of the oceanic flux of methane: Uncertainties and long term variations. *Chemosphere*, 26(1):579–589, 1993.

I. Levin, T. Naegler, R. Heinz, D. Osusko, E. Cuevas, a. Engel, J. Ilmberger, R. L. Langenfelds, B. Neininger, C. V. Rohden, L. P. Steele, R. Weller, D. E. Worthy, and S. a. Zimov. The global SF_6 source inferred from long-term high precision atmospheric measurements and its comparison with emission inventories. *Atmospheric Chemistry and Physics*, 10(6):2655–2662, 2010.

M. Maiss and C.A.M. Brenninkmeijer. Atmospheric SF_6 : Trends, Sources, and Prospects. *Environmental Science & Technology*, 32(20):3077–3086, 1998.

A. J. Manning, S O'Doherty, A. R. Jones, P. G. Simmonds, and R. G. Derwent. Estimating UK methane and nitrous oxide emissions from 1990 to 2007 using an inversion modeling approach. *Journal of Geophysical Research*, 116(D2):1–19, 2011.

A. J. Manning, D.B. Ryall, and R. G. Derwent. Estimating European emissions of ozone-depleting and greenhouse gases using observations and a modeling back-attribution technique. *Journal of Geophysical Research*, 108(D14):4405, 2003.

B.R. Miller, R.F. Weiss, P.K. Salameh, T. Tanhua, B.R. Greally, J. Mühle, and P.G. Simmonds. Medusa: a sample preconcentration and GC/MS detector system for in situ measurements of atmospheric trace halocarbons, hydrocarbons, and sulfur compounds. *Analytical chemistry*, 80(5):1536–45, 2008.

F. L. Moore, J. W. Elkins, E. A. Ray, G. S. Dutton, R. E. Dunn, D. W. Fahey, R. J Mclaughlin, T. L Thompson, P. A. Romashkin, D. F. Hurst, and P. R. Wamsley. Balloonborne in situ gas chromatograph for measurements in the troposphere and stratosphere. *Journal of Geophysical Research*, 108(D5):1–20, 2003.

N L Morrison and H N Webster. An Assessment of Turbulence Profiles in Rural and Urban Environments Using Local Measurements and Numerical Weather Prediction Results. *Boundary-Layer Meteorology*, 115(2):223–239, 2005.

L. Niemeyer and F.Y. Chu. SF_6 and the atmosphere. *IEEE Transactions on Electrical Insulation*, 27(1):184–187, 1992.

S. O'Doherty, D. M. Cunnold, A. Manning, B. R. Miller, R. H. J. Wang, P. B. Krummel, P.J. Fraser, P. G. Simmonds, A. McCulloch, R.F. Weiss, P. Salameh,

L. W. Porter, R.G. Prinn, J. Huang, G. Sturrock, D. Ryall, R.G. Derwent, and S.A. Montzka. Rapid growth of hydrofluorocarbon 134a and hydrochlorofluorocarbons 141b, 142b, and 22 from Advanced Global Atmospheric Gases Experiment (AGAGE) observations at Cape Grim, Tasmania, and Mace Head, Ireland. *Journal of Geophysical Research*, 109(D6):1–16, 2004.

R. Parker, H. Boesch, A. Cogan, A. Fraser, L. Feng, P.I. Palmer, J. Messerschmidt, N. Deutscher, D.W.T. Griffith, J. Notholt, P.O. Wennberg, and D. Wunch. Methane observations from the Greenhouse Gases Observing SATellite: Comparison to ground-based TCCON data and model calculations. *Geophysical Research Letters*, 38(15):2–7, 2011.

P. K. Patra, S. Houweling, M. Krol, P. Bousquet, D. Belikov, D. Bergmann, H. Bian, P. Cameron-Smith, M. P. Chipperfield, K. Corbin, a. Fortems-Cheiney, a. Fraser, E. Gloor, P. Hess, a. Ito, S. R. Kawa, R. M. Law, Z. Loh, S. Maksyutov, L. Meng, P. I. Palmer, R. G. Prinn, M. Rigby, R. Saito, and C. Wilson. TransCom model simulations of CH_4 and related species: linking transport, surface flux and chemical loss with CH_4 variability in the troposphere and lower stratosphere. *Atmospheric Chemistry and Physics*, 11(24):12813–12837, 2011.

P.K. Patra, M. Takigawa, K. Ishijima, B.-C. Choi, D. Cunnold, E.J. Dlugokencky, P. Fraser, A.G. Gomez-Pelaez, T.-Y. Goo, J.-S. Kim, P. Krummel, R. Langenfelds, F. Meinhardt, H. Mukai, S. O'Doherty, R.G. Prinn, P. Simmonds, P. Steele, Y. Tohjima, K. Tsuboi, K. Uhse, R. Weiss, D. Worthy, and T. Nakazawa. Growth Rate, Seasonal, Synoptic, Diurnal Variations and Budget of Methane in the Lower Atmosphere. *Journal of the Meteorological Society of Japan*, 87(4):635–663, 2009.

W. Peters, M.C. Krol, G. R. van der Werf, S. Houweling, C. D. Jones, J. Hughes, K. Schaefer, K. A. Masarie, A. R. Jacobson, J. B. Miller, C. H. Cho, M. Ramonet, M. Schmidt, L. Ciattaglia, F. Apadula, D. Heltai, F. Meinhardt, A. G. Di Sarra, S. Piacentino, D. Sferlazzo, T. Aalto, J. Hatakka, J. Strom, L. Haszpra, H. A. J. Meijer, S. Van der Laan, R. E. M. Neubert, A. Jordan, X. Rodo, J.-A. Morgui, A. T. Vermeullen, E. Popa, K. Rozanski, M. Zimnoch, A. C. Manning, M. Leuenberger, C. Uglietti, A. J. Dolman, P. Cias, M. Heimann, and P. P. Tans. Seven years of recent European net terrestrial carbon dioxide exchange constrained by atmospheric observations. *Global Change Biology*, 16(4):1317–1337, 2010.

M.J. Prather, C.D. Holmes, and J. Hsu. Reactive greenhouse gas scenarios: Systematic exploration of uncertainties and the role of atmospheric chemistry. *Geophysical Research Letters*, 39(9):1–5, 2012.

R. G. Prinn, R. F. Weiss, P. J. Fraser, P. G. Simmonds, D. M. Cunnold, F. N. Alyea, S. O'Doherty, P. Salameh, B. R. Miller, J. Huang, R. H. J. Wang, D. E. Hartley, C. Harth, L. P. Steele, G. Sturrock, P. M. Midgley, and A. McCulloch. A history of chemically and radiatively important gases in air deduced from ALE/GAGE/AGAGE. *Journal of Geophysical Research*, 105(D14):17751–17792, 2000.

A R Ravishankara, John S Daniel, and Robert W Portmann. Nitrous oxide (N2O): the dominant ozone-depleting substance emitted in the 21st century. *Science*, 326 (5949):123–125, 2009.

S. Reimann, A.J. Manning, P.G. Simmonds, D.M. Cunnold, R.H.J Wang, J. Li, A. McCulloch, R.G. Prinn, J. Huang, R.F. Weiss, P.J. Fraser, S. O'Doherty, B.R. Greally, K. Stemmler, M. Hill, and D. Folini. Low European methyl chloroform emissions inferred from long-term atmospheric measurements. *Nature*, 433(7025): 506–508, 2005.

M. Rigby, A. L. Ganesan, and R. G. Prinn. Deriving emissions time series from sparse atmospheric mole fractions. *Journal of Geophysical Research*, 116(D8):1–5, 2011a.

M. Rigby, A. J. Manning, and R. G. Prinn. Inversion of long-lived trace gas emissions using combined Eulerian and Lagrangian chemical transport models. *Atmospheric Chemistry and Physics*, 11(18):9887–9898, 2011b.

M. Rigby, A. J. Manning, and R. G. Prinn. The value of high-frequency, high-precision methane isotopologue measurements for source and sink estimation. *Journal of Geophysical Research*, 117(D12):1–14, 2012.

M. Rigby, J. Mühle, B. R. Miller, R. G. Prinn, P. B. Krummel, L. P. Steele, P. J. Fraser, P. K. Salameh, C. M. Harth, R. F. Weiss, B. R. Greally, S. O'Doherty, P. G. Simmonds, M. K. Vollmer, S. Reimann, J. Kim, K.-R. Kim, H. J. Wang, J. G. J. Olivier, E. J. Dlugokencky, G. S. Dutton, B. D. Hall, and J. W. Elkins. History of atmospheric SF_6 from 1973 to 2008. *Atmospheric Chemistry and Physics*, 10(21): 10305–10320, 2010.

M. Rigby, R. G. Prinn, P. J. Fraser, P. G. Simmonds, R. L. Langenfelds, J. Huang, D. M. Cunnold, L. P. Steele, P. B. Krummel, R. F. Weiss, S. O'Doherty, P. K. Salameh, H. J. Wang, C. M. Harth, J. Mühle, and L. W. Porter. Renewed growth of atmospheric methane. *Geophysical Research Letters*, 35(22):1–6, 2008.

D.B. Ryall and R.H. Maryon. Validation of the UK Met. Office's name model against the ETEX dataset. *Atmospheric Environment*, 32(24):4265–4276, 1998.

T. J. Schuck, C. a. M. Brenninkmeijer, a. K. Baker, F. Slemr, P. F. J. V. Velthoven, and a. Zahn. Greenhouse gas relationships in the Indian summer monsoon plume measured by the CARIBIC passenger aircraft. *Atmospheric Chemistry and Physics Discussions*, 10(2):2031–2087, 2010.

D.T. Shindell, G. Faluvegi, N. Bell, and G.A. Schmidt. An emissions-based view of climate forcing by methane and tropospheric ozone. *Geophysical Research Letters*, 32(4), 2005.

R. Spahni, R. Wania, L. Neef, M. van Weele, I. Pison, P. Bousquet, C. Frankenberg, P. N. Foster, F. Joos, I. C. Prentice, and P. van Velthoven. Constraining global methane emissions and uptake by ecosystems. *Biogeosciences*, 8(6):1643–1665, 2011.

A. Stohl, P. Seibert, J. Arduini, S. Eckhardt, P. Fraser, B. R. Greally, C. Lunder, M. Maione, J. Mühle, S. O'Doherty, R. G. Prinn, S. Reimann, T. Saito, N. Schmidbauer, P. G. Simmonds, M. K. Vollmer, R. F. Weiss, and Y. Yokouchi. An analytical inversion method for determining regional and global emissions of greenhouse gases: Sensitivity studies and application to halocarbons. *Atmospheric Chemistry and Physics*, 9(5):1597–1620, 2009.

A. Tarantola. *Inverse Problem Theory and Methods for Model Parameter Estimation*. Society for Industrial and Applied Mathematics, Philadelphia, Pennsylvania, 2005.

R. L. Thompson, C. Gerbig, and C. Rödenbeck. A Bayesian inversion estimate of N_2O emissions for western and central Europe and the assessment of aggregation errors. *Atmospheric Chemistry and Physics*, 11(7):3443–3458, 2011.

B. Tuzson, S. Henne, D. Brunner, M. Steinbacher, J. Mohn, B. Buchmann, and L. Emmenegger. Continuous isotopic composition measurements of tropospheric CO_2 at Jungfraujoch (3580 m a.s.l.), Switzerland: real-time observation of regional pollution events. *Atmospheric Chemistry and Physics*, 11(4):1685–1696, 2011.

C.D. Whiteman. *Mountain Meteorology*. Oxford University Press, New York, New York, 2000.

S.C. Wofsy. HIAPER Pole-to-Pole Observations (HIPPO): fine-grained, global-scale measurements of climatically important atmospheric gases and aerosols. *Philosophical transactions. Series A, Mathematical, physical, and engineering sciences*, 369 (1943):2073–86, 2011.

X. Xiong, S. Houweling, J. Wei, E. Maddy, F. Sun, and C. Barnet. Methane plume over south Asia during the monsoon season: satellite observation and model simulation. *Atmospheric Chemistry and Physics*, 9(3):783–794, 2009.

X. Yan, H. Akiyama, K. Yagi, and H. Akimoto. Global estimations of the inventory and mitigation potential of methane emissions from rice cultivation conducted using the 2006 Intergovernmental Panel on Climate Change Guidelines. *Global Biogeochemical Cycles*, 23(2):1–15, 2009.

C. Zhao, A.E. Andrews, L. Bianco, J. Eluszkiewicz, A. Hirsch, C. MacDonald, T. Nehrkorn, and M.L. Fischer. Atmospheric inverse estimates of methane emissions from Central California. *Journal of Geophysical Research*, 114(D16), 2009.